Roma Tre

DOTTORATO DI RICERCA IN

INGEGNERIA MECCANICA E INDUSTRIALE

XXXVIII CICLO

DESIGN, DEVELOPMENT AND VALIDATION OF MEASUREMENT METHODS AND SYSTEMS FOR THE FUNCTIONAL AND PERFORMANCE CHARACTERISATION OF RAPID PROTOTYPING SYSTEMS FOR BIOMEDICAL APPLICATIONS

Dottorando

Marta Cecchitelli

Tutor

Prof. Ing. Andrea Scorza

Prof. Ing. Salvatore Andrea Sciuto

Dott. Ing. Jan Galo

Coordinatore del Collegio di Dottorato

Prof.ssa Ing. Ornella Chiavola

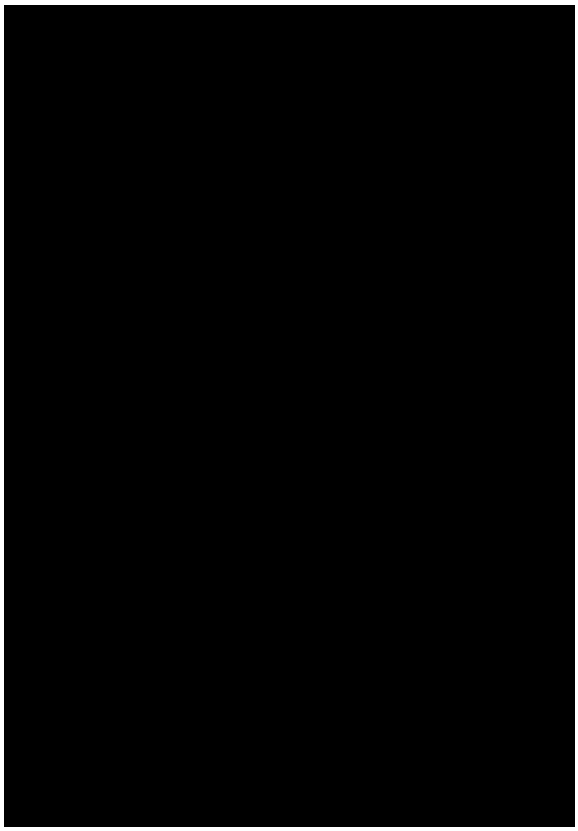

A tutti i maestri inconsapevoli che ho incontrato

Table of contents

Ringraziamenti

Tengo in modo particolare a ringraziare tutto il gruppo di lavoro che ha reso possibile ogni attività di questa tesi di Dottorato.

Desidero esprimere la mia gratitudine al supervisore Prof. Ing. Andrea Scorza per avermi seguito in ogni fase del progetto di ricerca nel corso di questo triennio, per la continua disponibilità e il supporto scientifico. Il suo accompagnamento, iniziato già durante il percorso di tesi magistrale, ha rappresentato per me un riferimento solido e costante, contribuendo in modo significativo alla mia crescita scientifica e professionale. Auspico sinceramente che il rapporto di stima reciproca costruito in questi anni possa proseguire in futuro, al di là delle diverse circostanze.

Un sentito ringraziamento va al co-tutor Prof. Ing. Salvatore Andrea Sciuto di cui ho avuto modo di apprezzare nel tempo le qualità umane e professionali nel suo ruolo di responsabilità, osservandone i modi di fare, la naturale ironia e prontezza di spirito, l'approccio al lavoro e la capacità di coniugare rigore e rispetto delle persone. Spesso, da una posizione discreta e indiretta, questo esempio ha rappresentato per me un importante riferimento di crescita.

Desidero riconoscere e ringraziare il co-tutor Dott. Ing. Jan Galo per il suo sostegno, espresso sempre attraverso parole di incoraggiamento e di apprezzamento, anche nei momenti più complessi, contribuendo a valorizzare il lavoro svolto e a rafforzare la fiducia nel percorso intrapreso. La sua capacità di riconoscere e sostenere l'impegno profuso ha avuto un impatto significativo sia sullo sviluppo di questa ricerca sia sul mio percorso di crescita personale.

Un sincero ringraziamento è rivolto ai professionisti Dott. Aurelio Secinaro e Ing. Luca Borro del laboratorio 3D dell'Ospedale Pediatrico Bambino Gesù per aver reso possibile lo svolgimento delle attività sperimentali in un contesto reale e multidisciplinare, contribuendo in modo determinante al valore applicativo di questa tesi.

Ringrazio il Prof. Ing. Massimiliano Barletta e i suoi collaboratori, in particolare l'Ing. Annalisa Genovesi, per avermi offerto la possibilità di svolgere le attività sperimentali nei laboratori di tecnologia meccanica mettendo a disposizione le macchine di prova e fornendo un prezioso supporto tecnico e scientifico.

Ringrazio inoltre tutti i colleghi e amici incontrati durante questo percorso, la Dott.ssa Ing. Giorgia Fiori, il Dott. Ing. Gabriele Bocchetta e l'Ing. Federico Filippi per il confronto quotidiano, il supporto morale e i momenti di condivisione che hanno reso questi anni impegnativi, non solo profondamente formativi, ma anche ricchi di momenti di leggerezza e sincera ilarità.

In ultimo, è per me doveroso ringraziare i miei genitori, che non mi hanno mai fatta sentire fuori tempo massimo e mi hanno sempre garantito la piena libertà di scelta in ogni circostanza.

La possibilità di scegliere, anche quando le decisioni non sono immediatamente condivise o si rivelano complesse, è uno dei doni più preziosi che io abbia ricevuto come figlia. Per questo, e per il sostegno silenzioso ma costante, anche dal punto di vista materiale, che non è mai venuto meno, mi sento profondamente fortunata e li ringrazio di cuore.

Ringrazio mia cugina, per la quale non ci sono molte parole da dire ma, come dice lei è "la mia seconda pelle", e in questo, racchiude tutto ciò che conta.

Chapter 1

Introduction

1.1 Background and Motivation

Over the past decade, three-dimensional (3D) printing has evolved from an experimental prototyping tool to an enabling technology for personalized healthcare. Its ability to translate patient-specific imaging data into tangible models, surgical guides and custom devices has reshaped preoperative planning, surgical simulation and medical education. Hospitals worldwide are now adopting additive manufacturing (AM), integrating digital fabrication directly into radiology, surgery and clinical engineering departments. This shift moves away from centralized industrial production toward decentralized manufacturing capable of producing customized anatomical models within hours.

Anatomical replicas obtained from Computed Tomography (CT) or Magnetic Resonance Imaging (MRI) data enhance understanding of complex morphologies and allow surgeons to prepare challenging procedures, anticipate complications and communicate more effectively with colleagues and families. This impact is particularly evident in paediatric, cranio-maxillofacial and cardiovascular surgery, where patient-specific anatomy can be often very small and highly variable and where improved preoperative insight could directly influence clinical outcomes. Tangible models also support multidisciplinary planning and provide an invaluable teaching tool for trainees, promoting a deeper understanding of anatomical variability.

At the technological level, the maturation of additive manufacturing has expanded the range of materials that can be used in clinical settings. Techniques such as fused filament fabrication, vat photopolymerization, powder bed fusion and material jetting enable the production of rigid bone-like structures, flexible airway models, replicas with graded stiffness and other structures that mimic organs. Ongoing research, together with the introduction of new elastomeric photopolymers, flexible filaments and multi-material jetting, has opened new possibilities for creating biomechanically realistic models. At the same time, continuous improvements in segmentation software, mesh editing and slicing tools are making the digital-to-physical workflow more reliable and easier to manage. These advancements are contributing to the growing adoption of additive manufacturing in point-of-care (PoC) environments.

However, alongside these opportunities, there are several persistent challenges that hinder the safe and reproducible implementation of 3D printing in PoC environments. Differences in imaging protocols, operator experience, segmentation strategies, digital modelling practices, print parameters, material batches and post-processing methods can combine to produce inconsistent anatomical fidelity or different mechanical behaviour of printed parts. Even when models appear visually accurate, subtle deviations in geometry or stiffness can compromise their suitability for surgical planning or simulation.

This confusion stems from the lack of harmonized standards and regulatory guidelines specifically tailored to PoC additive manufacturing. As highlighted in recent literature, the main obstacle to the large-scale deployment of 3D printing in hospitals lies in the operational and verification workflow: they would be designers, manufacturers and validators of medical devices, but without a unified regulatory framework defining how to conduct design control, documentation, process validation or acceptance thresholds. As a result, verification practices differ greatly from one institution to another. Dimensional accuracy can be assessed using calliper, structured light scanning, diagnostic CT or industrial CT, depending on local resources; mechanical performance can be measured using tensile, dynamic, compression or flexural tests, often without shared reference geometries. This heterogeneity compromises comparability between hospitals and introduces uncertainty into the manufacturing and validation process.

It is within this constantly evolving technological, clinical and regulatory context that this doctoral research is situated. Importantly, the work described in this dissertation was conducted directly within a hospital-based 3D printing laboratory during the development of a dedicated PoC additive manufacturing site. This unique context provided not only access to real patient data and clinical use cases but also direct involvement in the organizational, technical and quality-related processes required to implement an AM production workflow inside a non-industrial environment. The research activities were therefore developed in parallel with the practical challenges of designing, validating and stabilizing a PoC laboratory: during selecting equipment, defining segmentation and modelling procedures, experimenting with printing parameters, assessing dimensional and mechanical variability, and identifying sources of error that could significantly affect the reliability of the models.

This dual perspective, combining experimental research with active participation in a PoC production unit, influenced the entire thesis. On the one hand, it enabled rigorous, measurement-based studies aimed at the dimensional assessment of printed anatomical models as well as the

verification of the mechanical behaviour of those that mimic soft tissues. On the other hand, it offered a direct insight into how variability emerges in daily PoC operations, how different clinical departments interact with engineering workflows, and why quality control must be approached as a structured, traceable, and risk-informed manufacturing process.

Together, these considerations define the motivation behind this work: to contribute to the development of a preliminary quality control protocol that is experimentally tested and clinically feasible meaning compatible with the resources, instrumentation, time constraints and infrastructural limitations typical of a hospital environment rather than an industrial manufacturing facility, addressing the limitations that currently affect PoC additive manufacturing. This contribution is reinforced by the systematic collection of printing data, the analysis of real production experiences and the study of measurement methods, control strategies and preliminary acceptance thresholds, all developed in the practical context of a PoC laboratory alongside the academic approach of a mechanical and thermal measurement laboratory.

1.2 Quality Control in Biomedical Additive Manufacturing

Quality control (QC) is traditionally defined in international standards as "the part of quality management focused on fulfilling quality requirements," according to the terminology established in ISO 9000:2015. In the healthcare sector QC is a requirement for the adoption of any technology, where the accuracy, reproducibility and performance of materials have a direct impact on clinical decision-making. In biomedical additive manufacturing, QC should include a wide range of verification activities to ensure that printed anatomical models and devices are faithful to the anatomical region they are intended to reproduce or that they meet the requirements depending on their applications. From the literature, quality control in biomedical 3D printing can be thought of as a multi-layer process encompassing dimensional verification, mechanical characterization, reproducibility studies, material inspection, post-processing assessment and, when applicable, sterilization validation.

Despite the clear need for structured verification methods, the literature shows significant fragmentation in the approaches adopted for QC. Some studies rely on linear measurements, while others use surface deviation maps, volumetric analysis, CT-based metrology, landmark-based comparisons or visual inspection. Equally heterogeneous are the metrics used to evaluate mechanical properties: tensile tests, bending tests, compression, creep and dynamic mechanical analysis are all adopted inconsistently, with specimen geometries that often differ from one study

to another and lack standardization. Moreover, the quantification of uncertainty is rarely included, making it difficult to compare results across different laboratories or clinical units.

Unlike industrial AM facilities, hospital 3D printing labs operate with heterogeneous imaging inputs, variable operational expertise and resource constraints that limit the feasibility of traditional industrial metrology approaches. Imaging protocols differ between scanners and departments; segmentation workflows may depend on operator decisions and post-processing procedures are often adapted locally without reference to standardized methods. As a result, the quality of printed models is influenced by several interrelated factors, making quality control both critical and complex.

This lack of coordination is compounded by the absence of standards specifically dedicated to biomedical AM in PoC settings. Although international standards for additive manufacturing provide general definitions and industry guidelines, and the European regulatory framework, together with the United States medical device regulatory system, governs the approval and supervision of medical devices, there is no complete integration of these documents with the experimental needs of hospitals that produce anatomical models.

As part of the multi-stage quality control process, this thesis addresses the stages dedicated to dimensional and mechanical evaluation, proposing methodological contributions for assessing the geometric fidelity and mechanical behaviour of printed models, with the aim of supporting the definition of measurable acceptance criteria suitable for point-of-care 3D printing environments.

1.3 Research Objectives

The overall objective of this thesis is to propose quality control methodologies for biomedical 3D printing in hospitals. This objective is pursued through a combination of experimental investigations and metrological evaluations.

To this aim, the first specific objective is to analyze the current state of biomedical additive manufacturing and its regulatory context, highlighting the gaps and challenges that hinder standardized adoption in PoC contexts. This analysis serves as the conceptual basis for the thesis and identifies the need for structured and universally recognized quality control protocols.

The second specific objective concerns dimensional assessment: developing and validating measurements methods to quantify geometric fidelity using diagnostic CT, industrial CT and

image-analysis-based strategies. This includes the evaluation of volume, thickness, diameters and cross-sectional geometry, together with uncertainty estimation.

The third specific objective is to study the mechanical behaviour of both standardized and anatomically shaped samples designed to ensure repeatability and reproducibility in both the dimensional and morphological evaluation. Particular attention is paid to the tensile and viscoelastic properties of soft materials.

The final specific objective is to synthesize these findings into a comprehensive quality control framework that can support future PoC 3D printing laboratories in standardizing their workflows and ensuring reproducibility of printed medical models, with a particular focus on developing appropriate measurement procedures, selecting and validating metrological methods and integrating uncertainty estimation as a fundamental component of the verification process.

1.4 Dissertation Contributions

This thesis presents a series of contributions that combine experimental work conducted within a hospital 3D printing laboratory, a structured analysis of measurement and verification methods, and the formulation of a preliminary quality control framework for point-of-care additive manufacturing. The work integrates dimensional and mechanical evaluation approaches through image-based measurement methods and control strategies, preliminary acceptance thresholds and uncertainty considerations, developed both in the practical context of a PoC laboratory and through the analytical and statistical perspective typical of mechanical and thermal measurement environments. Each chapter contributes a specific element to this overall objective, from consolidating the scientific and regulatory background to developing validated measurement procedures and evaluating printed structures designed to replicate anatomical and soft tissue characteristics.

1.4.1 Chapter 2 Contributions

Chapter 2 provides a comprehensive overview of the current landscape of biomedical additive manufacturing, outlining the global state of the art, the most widely adopted technologies in clinical and research settings and the regulatory framework governing their use. The chapter is primarily based on the narrative review "*Measurements for quality control in biomedical 3D printing*", submitted on IEEE Sensors Reviews in 2025, developed by the author as first author. Through this work, the chapter consolidates existing knowledge on additive manufacturing processes, printable materials,

ISO/ASTM standards and medical device regulations relevant to point-of-care workflows. This chapter highlights the absence of quality control procedures dedicated to hospital manufacturing and identifies methodological gaps that currently limit the reproducibility and comparability of printed medical models.

Alongside this foundational review, the chapter presents an example of biomedical application of 3D printing from the author's work, "*First development of a LMHF vibration system for cell incubators*", published in proceeding of the IEEE International Workshop on Metrology for Industry 4.0 & IoT in 2024, to illustrate how additive manufacturing is already being used in clinical and research settings. In particular, the development of a high-frequency, low-amplitude vibration platform using 3D-printed components for the manufacture of customized structural elements is presented as an example of the versatility of additive manufacturing in the production of customized parts adapted to specific experimental constraints in hospital and laboratory settings. Similarly, the integration of measurement techniques in a clinical morphometric study on craniosynostosis "*Preliminary quantitative assessment of surgical outcomes in Craniosynostosis correction procedures: A 3D-Morphometric comparison*", published in Journal of Cranio-Maxillofacial Surgery in 2025, and in a study on hemifacial microsomia "*Evaluation of mandibular morphology in untreated growing patients with Hemifacial Microsomia: a 3D computed tomography study*", accepted for publication by Journal of Cranio-Maxillofacial Surgery in 2025, in which the author of this thesis contributed as a co-author, demonstrates how image-based reconstructions and volumetric assessments support surgical evaluation and underscore the importance of measurement methods in medical applications.

Together, these contributions define Chapter 2 as the theoretical and contextual basis of the dissertation, linking the scientific and regulatory landscape with examples of additive manufacturing and 3D measurement applied in hospital workflows. This framework supports the development of the measurement methods, experimental investigations and quality control strategies presented in the subsequent chapters.

1.4.2 Chapter 3 Contributions

Chapter 3 presents the 3D printing experimental activities carried out during the doctoral research, integrating the materials and methods presented in several published works. These activities were conducted in a hospital setting, mainly in the PoC 3D printing laboratory, and provide the practical basis for the dimensional and mechanical evaluations developed in the following chapters. The chapter introduces the complete digital to physical workflow used during

the research, from image acquisition and segmentation to printing, post-processing and preparation of the anatomical and mechanical samples to be tested.

The first contribution concerns the definition and analysis of the PoC 3D printing workflow, including segmentation procedures, virtual model generation, selection of printing technologies and materials, and post-processing operations. This section highlights how choices made in the early stages of image processing and modelling propagate through the manufacture process and affect the printed models. The workflow described here builds on the methodological approaches developed across author's published studies on model optimization and fabrication strategies. From a temporal perspective, the development of the workflow began with fused deposition modeling, the most accessible, widespread and cost-effective technology available in PoC environments.

The workflow described here builds on methodological approaches adopted in the author's published works involving fused deposition modelling (FDM) of anatomical structures. These includes "*Dimensional Assessment in Bioarchaeology Applications: a Preliminary Study on Quality Controls in 3D printing of Human Skulls*", published in proceeding of IMEKO TC-4 International Conference on Metrology for Archaeology and Cultural Heritage in 2023, and its extended journal version "*Quality Control of 3D Printing in Bioarchaeology: a Case Study on Dimensional Assessment of Cranial Models*" published in Acta IMEKO Journal in 2024. Further methodological insights were addressed in the biomedical study "*Quality Control for 3D Printing in Biomedical Applications: Dimensional Assessment of Skull Models*", published in proceedings of IEEE International Workshop on Metrology for Industry 4.0 & IoT in 2024 and in the study "*Volumetric Assessment for Quality Control in 3D Printed Bone Models: A Preliminary Investigation*" published in proceedings of the same conference in 2025 in which the fabrication of multiple printed clavicle models were described. Although developed in different application domains, these works collectively contributed to refining segmentation strategies, mesh optimization steps and FDM printing parameters adopted in the workflow.

Starting from this baseline, the chapter describes how it was possible to progressively refine segmentation strategies, which were later adapted and extended to more advanced additive manufacturing technologies used in the subsequent experimental activities. The chapter then documents the development of paediatric airway models, describing the reconstruction of tracheal geometries from diagnostic imaging, the design of simplified and anatomically faithful shapes, and the choice of materials used and printing stereolithography technology. These activities draw on the work "*Mechanical Properties of Soft Materials in 3D Printing: A Preliminary Quality Assessment*",

published in proceeding of IEEE International Workshop on Metrology for Industry 4.0 & IoT in 2025, and on its extended journal version "*Mechanical Testing of 3D-Printed Paediatric Trachea-Shaped Specimens: A Suitability Study*", published on Applied Sciences Journal in 2025 which discusses the manufacturing strategies and geometry modelling principles adopted: dog-bone, cylindrical and anatomically shaped specimens were designed and fabricated for mechanical characterized. The integration of the printed airway models into simulation tools also highlights their clinical relevance and the typical constraints encountered in PoC environments. In addition, PolyJet printed elastomeric specimens supplied by external collaborators were included to support comparative analyses across different printing technologies, as described in "*Mechanical Properties of Soft Materials in 3D Printing: A Preliminary Quality Assessment*", published in proceedings of IEEE International Workshop on Metrology for Industry 4.0 & IoT in 2025.

Overall, the chapter investigates how imaging, segmentation, printing parameters and material behaviour influence the reliability of biomedical 3D models. These preparation steps establish the experimental foundation for the dimensional assessment presented in Chapter 4 and mechanical assessments presented in Chapter 5.

1.4.3 Chapter 4 Contributions

Chapter 4 develops and validates the dimensional assessment methodologies used to evaluate the geometric fidelity of 3D-printed anatomical models. The chapter follows a progressive structure, moving from two-dimensional dimensional (2D) assessments to three-dimensional (3D) volumetric evaluations.

The first group of contributions concerns the 2D dimensional assessment of fused deposition modelling (FDM) printed skull models, investigated through three complementary studies.

The initial investigation, presented in "*Dimensional Assessment in Bioarchaeology Applications: a Preliminary Study on Quality Controls in 3D printing of Human Skulls*", published in proceeding of IMEKO TC-4 International Conference on Metrology for Archaeology and Cultural Heritage in 2023, proposes a preliminary method based on CT image analysis to compare a gold-standard cranial model with eight printed replicas. Although referred to bioarchaeological applications, the methodology, derived from a clinical CT-based workflow, directly parallels biomedical dimensional verification. The analysis focused on the transverse plane, quantifying section area, maximum longitudinal diameter and local thickness extracted from the slice of maximum diameter.

This approach was subsequently expanded and refined in the journal article "*Quality control of 3D printing in bioarchaeology: a case study on dimensional assessment of cranial models*" published in Acta IMEKO Journal in 2024. In this extended version, the segmentation procedure, threshold selection, mesh optimization and uncertainty evaluation were systematically analyzed. Despite its archaeological context, the study mirrors, both conceptually and technically, the image-based dimensional controls required for biomedical additive manufacturing, demonstrating how FDM variability and CT-based measurement uncertainties interact in complex anatomical geometries.

A further investigation, "*Quality Control for 3D Printing in Biomedical Applications: Dimensional Assessment of Skull Models*", published in proceedings of IEEE International Workshop on Metrology for Industry 4.0 & IoT in 2024, translated the method into a biomedical setting. This study examined the influence of operator-dependent positioning during CT acquisition and extended the dimensional assessment to the coronal plane, again quantifying area, diameter and thickness discrepancies. The repeated positioning of the reference model enabled an explicit estimation of intra-operator variability, providing additional insight into measurement uncertainty under realistic hospital workflows.

The chapter then advances to 3D volumetric assessment, through the study "*Volumetric Assessment for Quality Control in 3D Printed Bone Models: A Preliminary Investigation*" published in IEEE International Workshop on Metrology for Industry 4.0 & IoT in 2025. Multiple clavicle models were printed using FDM technology and the volumes of the models derived from diagnostic CT and industrial CT were compared, using both voxel-based masks and tetrahedral STL decomposition. This work establishes a reference variability range for repeated FDM prints of bone-like geometries and illustrates how different CT modalities influence volumetric accuracy and uncertainty estimation. The findings represent a key step toward defining preliminary acceptance thresholds for volumetric QC in PoC environments.

Together, these four studies establish a coherent 2D and 3D dimensional evaluation framework, demonstrating how imaging protocols, segmentation strategies, printing parameters and CT-based measurement procedures jointly affect the reproducibility of FDM printed anatomical models.

1.4.4 Chapter 5 Contributions

Chapter 5 addresses the mechanical assessment of soft and flexible materials used to reproduce organs and tissue-mimicking anatomical structures. The first investigation, "*Mechanical Properties of Soft Materials in 3D Printing: A Preliminary Quality Assessment*" published in proceedings of IEEE

International Workshop on Metrology for Industry 4.0 & IoT in 2025, proposed a practical tensile-based protocol to estimate elastic modulus directly from anatomically shaped stereolithography printed specimens, offering an accessible QC method for soft models used in surgical simulation.

This work was substantially expanded in the journal article "*Mechanical Testing of 3D-Printed Paediatric Trachea-Shaped Specimens: A Suitability Study*" published on Applied Sciences Journal in 2025, which introduced a multi-modal mechanical characterization including static tensile tests, dynamic mechanical analysis and long-duration creep tests. The study compared anatomical, cylindrical and dog-bone specimens, showing the influence of geometry on measured properties and the importance of using anatomically faithful samples for clinically relevant mechanical evaluation.

A complementary study, "*Mechanical Properties of Soft Materials in 3D Printing: A Preliminary Quality Assessment*" published in proceeding of IEEE International Workshop on Metrology for Industry 4.0 & IoT in 2025, investigated the mechanical behaviour of PolyJet-printed elastomers and quantified the influence of build orientation on tensile strength, modulus and elongation at break. This work highlights how anisotropy and process-specific variability must be considered when defining QC strategies for soft materials.

These contributions collectively define the mechanical assessment proposed, providing evidence for the variability, anisotropy and geometry-dependence of soft 3D-printed materials.

1.4.5 Chapter 6 Contributions

Chapter 6 summarizes the theoretical and experimental results developed throughout the dissertation into an integrated quality control (QC) framework tailored to point-of-care (PoC) 3D printing environments. Drawing on the dimensional and mechanical findings presented in Chapters 4 and 5, the chapter consolidates the main sources of variability observed along the digital to physical workflow and identifies the critical parameters that influence the reliability of anatomical models. A key contribution of this chapter is the proposal of preliminary acceptance thresholds of 2% for both dimensional and mechanical performance, derived from experimental data obtained on fused deposition modelling (FDM), stereolithography (SLA) and PolyJet printed specimens. Furthermore, the chapter proposes a structured QC workflow that incorporates measurement procedures, metrological methods and uncertainty estimation. Collectively, these elements provide a framework and database that can guide future PoC units in manufacturing practices and verification phases.

1.4.6 Chapter 7 Contributions

Chapter 7 presents the overall conclusions of the dissertation and situates the results within the broader context of biomedical additive manufacturing. The chapter summarizes the scientific contributions achieved in terms of workflow analysis, dimensional and mechanical assessment, and the development of a preliminary quality control framework for hospital-based 3D printing. It also highlights the contribution of this work to uncertainty estimation and proposes the adoption of a single, comparable metric to support the harmonization of results across different biomedical additive manufacturing units. Building on these elements, the chapter outlines strategies to improve reproducibility, traceability and standardization within PoC environments.

Finally, Chapter 7 identifies future research directions, emphasizing methodologies and gaps that must be addressed to develop unified QC protocols, extend assessment methods to additional technologies and materials, and support the regulatory integration and inter-institutional harmonization.

1.5 Summary of Contributions

In summary, this thesis contributes to progress in the field of biomedical additive manufacturing through a combination of experimental contributions and measurement methods developed in the context of hospital-based point-of-care (PoC) 3D printing laboratory development. The work integrates direct operational experience gained during the implementation of a PoC production site with dimensional and mechanical evaluation studies and the development of a preliminary quality control framework developed in a clinical context.

Chapter 2 consolidates the international scientific and regulatory landscape of biomedical additive manufacturing and proposes a unified PoC 3D printing workflow derived from the analysis of existing practices reported in the literature. The following chapters explicitly follow this workflow with the intent to contribute to any gaps: Chapter 3 presents the experimental production activities carried out during the doctoral work, describing from segmentation and modelling to manufacturing of anatomical models and mechanical specimens using different 3D printing technologies. Chapters 4 and Chapters 5 investigate the dimensional and mechanical assessment methods applied to these printed parts, providing quantitative evidence on geometric fidelity, material behaviour and the associated sources of uncertainty. Chapter 6 combines these findings into a preliminary, measurement-based QC framework for PoC manufacturing, while Chapter 7 contextualizes the results, outlines their broader implications and defines future research directions.

The research presented in this thesis is supported by a series of peer-reviewed publications that reflect the progression of the experimental activities and methodological developments undertaken during the doctoral work. These include studies on dimensional analysis of fused deposition modelling printed skull and bone models, mechanical characterization of stereolithography and PolyJet soft materials, and applications of additive manufacturing in clinical and experimental environments. Together, these publications form the scientific foundation of the dissertation and demonstrate the coherence and continuity of the research pathway, as well as its sharing with the international scientific community.

1.5.1 Journal Article

- Title: Measurements for Quality Control in Biomedical 3D Printing: Standards, Gaps and Missing Protocols

  Authors: Marta Cecchitelli, Giorgia Fiori, Jan Galo, Salvatore Andrea Sciuto, Andrea Scorza.

  Journal: submitted to IEEE Sensors Review, 2025.
- Title: Quality control of 3D printing in bioarchaeology: a case study on dimensional assessment of cranial models

  Authors: Marta Cecchitelli, Giorgia Fiori, Gabriele Bocchetta, Federico Filippi, Fabio Leccese, Jan Galo, Salvatore Andrea Sciuto, Andrea Scorza.

  Journal: *Acta IMEKO, 2023.*
- Title: Preliminary quantitative assessment of surgical outcomes in Craniosynostosis correction procedures: A 3D-Morphometric comparison

  Authors: Urbano Urbani, Luca Borro, Alessia Giorgi, Sergio Silvestri, Marta Cecchitelli, Olivia Pagliarosi, Jan Galo, Luca Armisi, Mario Zama, Aurelio Secinaro.

  Journal: Journal of Cranio-Maxillofacial Surgery, 2025.
- Title: Evaluation of mandibular morphology in untreated growing patients with Hemifacial Microsomia: a 3D computed tomography study

  Authors: Roberto Uomo, Wanda Maldonato, Alessandra Putrino, Luca Borro, Marta Cecchitelli, Lucilla Ravà, Aurelio Secinaro, Angela Galeotti.

  Journal: Journal of Cranio-Maxillofacial Surgery, 2025.
- Title: Mechanical Testing of 3D-Printed Paediatric Trachea-Shaped Specimens: A Suitability Study

Authors: Marta Cecchitelli, Giorgia Fiori, Annalisa Genovesi, Massimiliano Barletta, Luca Borro, Jan Galo, Aurelio Secinaro, Salvatore Andrea Sciuto, Andrea Scorza.

Journal: Applied Sciences, 2025.

1.5.2 Conference Paper

- Title: Dimensional assessment in bioarchaeology applications: a preliminary study on quality controls in 3D printing of human skulls

  Authors: Marta Cecchitelli, Giorgia Fiori, Gabriele Bocchetta, Federico Filippi, Fabio Leccese, Jan Galo, Salvatore Andrea Sciuto, Andrea Scorza.

  Proceedings: IMEKO TC-4 International Conference on Metrology for Archaeology and Cultural Heritage, MetroArchaeo, 2023.
- Title: First development of a LMHF vibration system for cell incubators

  Authors: Marta Cecchitelli, Federico Filippi, Giorgia Fiori, Jan Galo, Andrea Del Fattore, Aurelio Secinaro, Salvatore Andrea Sciuto, Andrea Scorza.

  Proceedings: IEEE International Workshop on Metrology for Industry 4.0 & IoT, MetroInd4.0&IoT, 2024.
- Title: Quality control for 3D Printing in biomedical applications: a case study on dimensional assessment of skull models

  Authors: Marta Cecchitelli, Giorgia Fiori, Jan Galo, Salvatore Andrea Sciuto, Andrea Scorza.

  Proceedings: IEEE International Workshop on Metrology for Industry 4.0 & IoT, MetroInd4.0&IoT, 2024.
- Title: Mechanical Properties of Soft Materials in 3D Printing: A Preliminary Quality Assessment

  Authors: Marta Cecchitelli, Giorgia Fiori, Annalisa Genovesi, Massimiliano Barletta, Jan Galo, Salvatore Andrea Sciuto, Andrea Scorza.

  Proceedings: IEEE International Workshop on Metrology for Industry 4.0 & IoT, MetroInd4.0&IoT, 2025.
- Title: Volumetric Assessment for Quality Control in 3D Printed Bone Models: A Preliminary Investigation

  Authors: Marta Cecchitelli, Giorgia Fiori, Alessandro Luchetti, Jan Galo, Salvatore Andrea Sciuto, Andrea Scorza.

Proceedings: IEEE International Workshop on Metrology for Industry 4.0 & IoT, MetroInd4.0&IoT, 2025.

- Title: Mechanical Properties of Paediatric Trachea-shaped Specimens: a Preliminary Quality Assessment

  Authors: Marta Cecchitelli, Giorgia Fiori, Luca Borro, Annalisa Genovesi, Massimiliano Barletta, Jan Galo, Salvatore Andrea Sciuto, Andrea Scorza.

  Proceedings: IEEE International Workshop on Biomedical Applications, Technologies and Sensors, BATS, 2025.

Chapter 2

State of the Art and Regulatory Background

2.1 Overview of Biomedical 3D Printing Technologies

Additive manufacturing (AM), often referred to as 3D printing, is defined in the ISO/ASTM 52900 standard [1] as a process of joining materials to make parts from three-dimensional model data, usually layer upon layer, as opposed to subtractive and formative manufacturing methods.

In practice, this means that a digital model created from Computer Aided Design (CAD) software or medical imaging data is converted into a stack of layers and the machine builds the physical object by adding material only where it is needed. This layer-by-layer approach makes it possible to fabricate complex geometries that would be difficult or impossible to obtain with conventional machining or molding. Over the past decade, three-dimensional (3D) printing has moved from experimental prototyping to routine clinical support, enabling patient-specific anatomical models, surgical guides and personalized prostheses fabricated within point-of-care (PoC) hospital environments [2].

Initially, in biomedical field additive manufacturing was mainly used for prototypes and educational models; more recently, it has been increasingly adopted for patient-specific anatomical models, surgical guides and medical devices. Several clinical studies and reviews describe how hospitals have started to integrate 3D printing at the point of care, using in-house facilities to support diagnosis, pre-operative planning and treatment. For example, a feasibility study on orthopedic trauma showed that patient-specific plates for fixation of proximal tibia fractures can be designed and printed directly within the hospital, with production times compatible with the surgical schedule and with good fitting on the patient's anatomy [3]. Narrative reviews in oral and cranio-maxillofacial surgery report similar experiences, where virtual surgical planning and point-of-care 3D printing have been used to prepare cutting guides, reconstruction plates and anatomical models, helping surgeons to plan complex cases and to communicate with patients and trainees [4]. A systematic review focused on 3D printed medical devices used directly to treat patients confirms that clinical use has increased sharply in recent years, with a wide range of applications across specialties and with different combinations of imaging modalities, design workflows and printing technologies [5].

All over the world, this decentralization offers several clinical advantages and reported benefits include more efficient pre-operative planning, reduced operating time and improved communication with patients and multidisciplinary teams [6], [7].

The main AM technologies (Figure 2.1) that are currently used in point-of-care hospital environments include Fused Deposition Modelling (FDM), Stereolithography (SLA), Selective Laser Sintering (SLS) and Material Jetting (MJ) [8]. In most of the reported experiences, medical images such as Computed Tomography (CT) or Magnetic Resonance Imaging (MRI) scans are segmented to obtain a 3D representation of the patient's anatomy, which is then refined in dedicated software and prepared for printing [9]. The final application can be an anatomical model for visualization and simulation, a cutting or drilling guide used during surgery, or in some cases a device used directly in the patient's body. Beyond anatomical models, 3D printing is also increasingly used to fabricate customized components for experimental devices within hospital and laboratory settings. An example is the development of a low-magnitude and high-frequency (LMHF) vibration system for cell incubators, in which several structural elements were produced using FDM technology to obtain a customizable platform for incubator mechanical stimulation cells [10]. In this project, I contributed directly to the design and fabrication of the tailored 3D-printed components. The AM can support the rapid prototyping of functional parts adapted to specific biomedical constraints. This application shows how 3D printing extends beyond patient-specific anatomical reproduction to enable the development of research-oriented devices within clinical and laboratory workflows. In addition to manufacturing anatomical models and patient-specific devices, 3D technologies play a central role in quantitative clinical analysis. This is reflected in two recent studies that involved the author in the development and interpretation of image-based measurements: a 3D morphometric evaluation of surgical outcomes in craniosynostosis, where CT reconstructions were used to quantify cranial symmetry and postoperative changes[11], and a study on hemifacial microsomia, where mandibular volumes and surface deviations were assessed to characterize skeletal asymmetry [12]. These works contribute to investigating the link between accurate segmentation, reliable 3D reconstruction and reproducible measurement methods with their potential role in supporting clinical decision-making and the validation of patient-specific models, reinforcing the importance of quantitative approaches in biomedical 3D printing workflows.

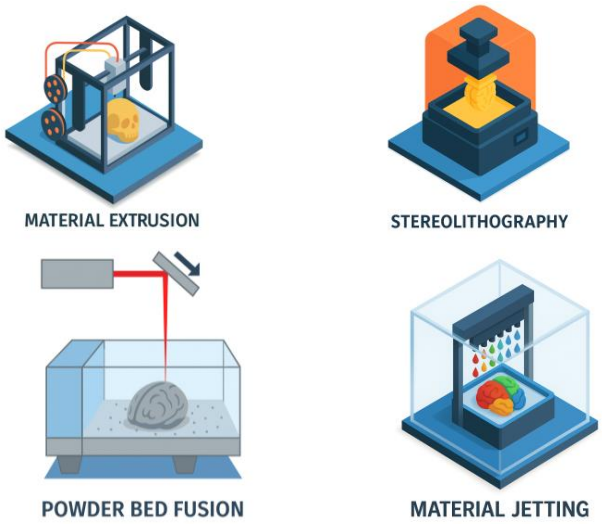

Figure 2.1. Overview of the main AM technologies used in biomedical 3D printing. From left to right: Material Extrusion, Vat Photopolymerization (Stereolithography), Powder Bed Fusion, and Material Jetting. Each process relies on distinct physical principles and materials, enabling different levels of resolution, surface quality and suitability for clinical applications.

These studies also show that the choice of 3D printing technology is strongly linked to the clinical task. Rigid bone models for trauma or craniofacial reconstruction are often produced with material extrusion or vat photopolymerization; dental and craniofacial guides and models frequently rely on high-resolution photopolymerization systems; strong functional parts or complex porous structures may employ powder-based methods; and organs or soft-tissue phantoms may benefit from multi-material and elastomeric printing. Table 2.1 summarizes the main AM technologies currently used in PoC environments, highlighting their operating principles, accuracy, limitations, and clinical implications. In fact, each technology has its own strengths and weaknesses in terms of accuracy, surface finish, material compatibility, mechanical performance, post-processing and sterilization. These factors determine not only the visual appearance of anatomical models, but also their suitability for different clinical uses and the type of quality control that can be realistically implemented in a hospital setting.

Table 2.1. Overview of Additive Manufacturing Technologies for Point-of-Care Use

Technology	**Material and Principle**	**Typical Accuracy**	**Key Limitations and Risks**	**PoC Implications**
Material extrusion	Thermoplastic filament extrusion	Moderate accuracy	Layer lines, anisotropy, warping, support removal issues	Good for non-critical anatomical models and guides
Vat photopolymerization	Light-curable resin, layer-by-layer curing	High surface fidelity, fine detail	Material shrinkage, residual monomer, post-curing drift	Suitable for high-precision models, requires careful QA
Powder bed fusion	Laser sintering of powder	Good accuracy, internal complexity, no supports needed	Powder handling, cost, thermal uniformity, surface roughness	Ideal for complex geometry and robust parts
Material Jetting	Droplet deposition + UV curing	Multi-material, gradient stiffness, excellent surface	High cost, nozzle maintenance, material robustness limits	Useful for multi-material realistic models, prototyping

The following subchapters provide an overview of the technologies most relevant to this thesis with specific attention to their use in biomedical applications. No single technique is suitable for all clinical needs. For this reason, understanding the strengths and limitations of each process is important to the implications for quality control in point-of-care 3D printing.

2.1.1 Fused Deposition Modelling

FDM is the most widely adopted technology in hospital-based 3D printing units. It works by melting a thermoplastic filament and depositing it layer by layer through a heated nozzle. Its popularity is linked to its low cost, ease of use and the availability of many materials. These characteristics make FDM suitable for general anatomical models, bone structures and educational tools. Even though FDM is practical, it has limitations that must be considered when it is used for clinical applications. The printed parts are anisotropic because the adhesion between layers is

weaker than the strength within each layer. This affects both dimensional accuracy and mechanical behavior. The surface quality depends on the layer height and can show visible ridges, especially in curved or sloped regions. Common artefacts include warping at the base of the model, stringing in thin features and variations caused by changes in temperature or humidity during printing [13].

2.1.2 Vat photopolymerization

Vat photopolymerization techniques, such as SLA and Digital Light Processing (DLP), offer significantly higher accuracy. These systems cure liquid resin using a laser or a projected light pattern. They are commonly used when detailed anatomical reproduction is needed, especially for dental structures, vascular geometries or small anatomical regions [14]. Their main advantage is the ability to produce smooth surfaces and thin-wall features.

Photopolymer resins, however, are sensitive to the conditions of post-processing. After printing, each part must be washed to remove uncured resin and then exposed to UV light for post-curing. These steps can cause dimensional changes if the exposure times, cleaning solutions or curing conditions vary. Shrinkage during curing is a known issue and can affect the final geometry. Some resins may also contain residual monomers that influence mechanical behavior or biocompatibility. Sterilization remains a critical issue for photopolymer resins. Many of them deform or deteriorate when exposed to heat or chemical sterilization, making their use in sterile environments more complex. This requires careful verification of dimensions and mechanical properties [15].

2.1.3 Powder Bed Fusion

Powder bed fusion, particularly SLS, is an AM method capable of producing strong and dimensionally stable parts. It works by selectively fusing layers of polymer powder with a laser. One key advantage is that unused powder supports the part during fabrication, allowing the creation of complex geometries, including hollow structures and internal channels, without the need for additional support material. This is useful for hollow or intricate models. Printed parts are usually strong and dimensionally stable [16]. Despite these advantages, Powder Bed Fusion is less common in PoC laboratories because it requires a controlled environment, specialized ventilation and strict powder-handling procedures. SLS systems are expensive and require a rigorous infrastructure: powder handling, filtration, coating stability and thermal management are all non-trivial operations and represent a real operational burden [17].

2.1.4 MultiJet Printing

MJ printing, often known through commercial systems such as PolyJet, produces parts by jetting small droplets of photopolymer that are immediately cured by UV light. This process allows very smooth surfaces, high accuracy and, importantly, the ability to combine multiple materials in the same object. As a result, gradients of stiffness and realistic anatomical characteristics can be reproduced, which is particularly useful for organ models and multi-tissue structures [18]. The main advantage of MJ printing is its capacity to generate anatomically realistic phantoms with fine detail and material variations. In the biomedical domain, it is especially useful for fabricating patient-specific anatomical models, surgical guides, and training phantoms mimicking mechanical gradients combining rigid and soft materials under a unified workflow [19]. MJ has been used recently in biomedical applications such as an innovative dental stackable [20], a patient-specific simulator for endoscopic sinus surgery [21] and multi-color bone models [22]. Its high-dimensional accuracy and capacity for localized material tuning make it attractive for preoperative planning and device prototyping in medicine. However, limitations include the limited mechanical strength of photopolymers, potential cytotoxicity of residual photoinitiators and cost of materials and postprocessing [23].

2.2 International Regulatory Landscape

The international regulatory landscape relevant to 3D printing in point-of-care (PoC) environments, as listed in Table 2.2, is broad and heterogeneous. Existing frameworks were developed mainly for industrial or centralized manufacturing, but many of their principles can be applied to PoC units, where hospitals act simultaneously as designers, manufacturers and users of patient-specific medical devices. For this reason, it is essential to understand how current regulations, standards and technical documents contribute to defining safety, performance and quality requirements.

Table 2.2. International Regulatory Landscape

Year	Jurisdiction/Authority	Title	Ref.
2015	South Korea, Ministry of Food and Drug Safety (MFDS)	Guidance on Patient-matched Medical Devices manufactured using 3D printers	[24]
2015	Japan, Welcome to Ministry of Health, Labour and Welfare (MHLW)	Publication of Guidance for the Evaluation of Emerging Technology Medical Devices/Regenerative Medical Products	[25]
2017	Europe, European Parliament	Regulation (EU) 2017/745	[26]

	and of the Council		
2017	USA, Food and Drug Administration (FDA)	Technical Considerations for Additive Manufactured Medical Devices	[27]
2018	ISO	ISO 10993-1: 2018 - Biological evaluation of medical devices Part 1: Evaluation and testing within a risk management process	[28]
2018	ISO	ISO 19227: 2018 - Implants for surgery — Cleanliness of orthopedic implants — General requirements	[29]
2018	DICOM, National Electrical Manufacturers Association (NEMA)	Supplement 205: DICOM Encapsulation of STL Models for 3D Manufacturing	[30]
2019	Health Canada	Guidance Document - Supporting Evidence for Implantable Medical Devices Manufactured by 3D Printing	[31]
2019	China, National Medical Products Administration (NMPA)	Issued Guidelines for Technical Review of the Registration of Custom-Made and Material Additive-Based Medical Devices of Passive Implantable Bones, Joints and Oral Hard Tissues	[32]
2020	ASTM	ASTM F3335-20 - Standard Guide for Assessing the Removal of Additive Manufacturing Residues in Medical Devices Fabricated by Powder Bed Fusion	[33]
2020	ISO	ISO 14155: 2020 - Clinical investigation of medical devices for human subjects — Good clinical practice	[34]
2020	DICOM, National Electrical Manufacturers Association (NEMA)	Supplement 208: DICOM Encapsulation of OBJ Models for 3D Manufacturing and Virtual Reality	[35]
2021	Singapore (HSA)	Regulatory Guideline for 3D-Printed Medical Devices	[36]
2015, confirmed in 2021	IEC	IEC 62366-1:2015 - Medical devices - Part 1: Application of usability engineering to medical devices	[37]
2021	ISO	ISO 13485: 2021 - Medical devices — Quality management systems — Requirements for regulatory purposes	[38]
2021	ISO/ASTM	ISO/ASTM TS 52930:2021 - Additive manufacturing — Qualification principles — Installation, operation and performance (IQ/OQ/PQ) of PBF-LB equipment	[39]
2021	ISO/ASTM	ISO/ASTM 52900:2021 - Additive manufacturing — General principles — Fundamentals and vocabulary	[1]
2021	Europe, Medical Device Coordination Group Document (MDCG)	MDCG 2021-3 - Questions and Answers on Custom-Made Devices	[40]
2022	Italy, Government	Legislative Decree 137/2022	[41]
2023	International Medical Device Regulators Forum (IMDRF)	IMDRF/PMD WG/N74 – Personalized Medical Devices – Production Verification and Validation	[42]
2023	ISO/ASTM	ISO/ASTM 52920:2023 – Additive manufacturing — Qualification principles — Requirements for industrial additive manufacturing processes and production sites	[43]
2024	ASTM	ASTM F3187-16 Standard Guide for Directed Energy	[44]

		Deposition of Metals	
2014, confirmed in 2024	ISO	ISO 11135: 2014 Sterilization of health-care products — Ethylene oxide — Requirements for the development, validation and routine control of a sterilization process for medical devices	[45]
2024	ISO	ISO 14630:2024 - Non-active surgical implants — General requirements	[46]
2024	ISO/ASTM	ISO/ASTM 52904: 2024 - Additive manufacturing of metals — Process characteristics and performance — Metal powder bed fusion process to meet critical applications	[47]
2024	ISO/ASTM	ISO/ASTM 52909:2024 - Additive manufacturing of metals — Finished part properties — Orientation and location dependence of mechanical properties for metal parts	[48]
2024	ISO/ASTM	ISO/ASTM 52927: 2024 – Additive manufacturing — General principles — Main characteristics and corresponding test methods	[49]
2024	ISO/ASTM	ISO/ASTM 52928:2024 – Additive manufacturing of metals— Feedstock materials — Powder life cycle management	[50]
2024	USA, Food and Drug Administration (FDA)	Quality Management System Regulation: Final Rule Amending the Quality System Regulation	[51]
2019, confirmed in 2025	ISO	ISO 14971:2019 - Medical devices — Application of risk management to medical devices	[52]
2025	ISO	ISO 11137-1:2025 - Sterilization of health care products — Radiation - Part 1: Requirements for the development, validation and routine control of a sterilization process for medical devices	[53]
2025	ISO	ISO 5092:2025 - Additive manufacturing for medical — General principles — Additive manufacturing of non-active implants	[54]
2025	Australia, Therapeutic Goods Administration (TGA)	Medical devices reforms: personalized medical devices	[55]
Under publication	ISO/ASTM	ISO/ASTM 52929 - Additive manufacturing of metals — Powder bed fusion — Presentation of material properties in material data sheets	[56]
Work in progress	ASTM	WK 55610 - New Test Methods for the Characterization of Powder Flow Properties for Additive Manufacturing Applications	[57]
Work in progress	ASTM	WK 58219 - Feedstock Materials-Creating Feedstock Specifications for Metal Powder Bed Fusion	[58]
Work in progress	ASTM	WK 62190 - Feedstock Materials Technical specifications on Metal powder	[59]
Work in progress	ASTM	WK 62867 - Guide for Design for Material Extrusion Processes	[60]
Work in progress	ASTM	WK 64190 - Additive Manufacturing Design – Decision Guide	[61]
Work in progress	ASTM	WK 65420 - Standard Guidlines Laser Powder Bed Fusion (L-PBF) for Metal	[62]

2.2.1 International Standards and Quality Requirements

Regulation of medical devices relies on two global pillars: the implementation of a Quality Management System (QMS) and the systematic application of risk management. ISO 13485 [38] establishes the structure of a QMS for medical devices, while ISO 14971 [52] describes the process for identifying, evaluating and controlling risks throughout the entire lifecycle of a device. These standards are the foundation for compliant manufacturing processes in all jurisdictions. The recent update of the Quality Management System Regulation issued by the United States Food and Drug Administration (FDA) [51], which aligns its expectations with ISO 13485 [63], reflects a strong international trend toward harmonization.

Several countries and authorities have progressively introduced documents dedicated to additive manufacturing or patient-matched devices. South Korea was among the first to publish a dedicated guideline on 3D-printed patient-matched devices [24], followed shortly by Japan with a document addressing the evaluation of emerging medical technologies [25]. In Europe, the Medical Device Regulation (EU) 2017/745 [26] establishes safety and performance requirements that apply equally to conventional and additively manufactured devices. The FDA's Technical Considerations for Additive Manufactured Medical Devices [27] provides similar expectations in the United States and remains one of the most influential documents in the field.

Other regulatory bodies have followed with national guidance adapted to their healthcare systems. Singapore's Health Sciences Authority (HSA) issued a regulatory guideline on 3D-printed medical devices [36], while Australia's Therapeutic Goods Administration (TGA) published updates on personalized medical devices and later initiated a wider reform project specifically focused on PoC manufacturing [64]. Japan's Ministry of Health, Labor and Welfare (MHLW) [65], South Korea's MFDS [24] and Health Canada [31] have also developed documents addressing additively manufactured or custom-made devices, including those produced through powder bed fusion or intended for orthopedic and dental applications, as reflected in the Chinese National Medical Products Administration guideline for additive-based implants [32].

Alongside regulatory guidance, a substantial number of standards contribute to defining good practices for additive manufacturing. ISO 10993-1 [28] remains essential for the biological evaluation of medical devices, while ISO 19227 [29] specifies cleanliness requirements for orthopedic implants. Standards developed by DICOM, such as Supplement 205 for Standard Triangulation Language (STL) models [30] and Supplement 208 for OBJ models [35], address the need for consistent encapsulation of 3D model data generated from medical imaging.

2.2.2 ISO and ASTM Standards for Additive Manufacturing

More recently, several ISO/ASTM technical standards have been introduced to support the qualification and validation of additive manufacturing processes. ISO/ASTM 52920 [43] defines requirements for industrial AM production sites, and ISO/ASTM TS 52930 [39] describes installation, operation and performance qualification steps (IQ/OQ/PQ) for laser-based powder bed fusion systems. ISO/ASTM 52904 [47] focuses on process performance for critical metal applications, while ISO/ASTM 52909 [48] deals with the dependence of mechanical properties on part orientation and build location. ISO/ASTM 52927 [49] and ISO/ASTM 52928 [50] address part characterization and feedstock lifecycle management, and ISO/ASTM 52900 [1] defines general principles and terminology.

Beyond additive manufacturing itself, other standards influence related aspects of clinical use. ISO 14155 [34] governs good clinical practice for medical device investigations, while IEC 62366-1 [37] sets requirements for usability engineering. Standards for sterilization, such as ISO 11135 [45] for ethylene oxide and ISO 11137-1 [53] for radiation sterilization, remain essential reference documents, even though many materials used in 3D printing do not fully align with conventional sterilization profiles. Additional medical device requirements, such as those in ISO 14630 [46] for non-active surgical implants, provide baseline expectations that PoC manufactured devices may be expected to meet.

Some initiatives explicitly target personalized or patient customized devices. The medical device coordination group in Europe published MDCG 2021-3 [40] to clarify the conditions under which custom-made devices can be placed on the market. At the international level, the International Medical Device Regulators Forum (IMDRF) released guideline N74 [42] to define principles for production verification and validation of personalized medical devices, including those produced near the point of care. This document represents an important step toward clearer expectations for decentralized manufacturing.

Finally, several standards and technical documents remain under development. These include ISO/ASTM 52929 on powder bed fusion material data sheets [56] and various ASTM work items focused on feedstock characterization, powder specifications, design guidelines for material extrusion and laser powder bed fusion processes [57], [58], [59], [60], [61], [62]. Their development demonstrates the growing interest in structured quality control for additive manufacturing.

Although many building blocks already exist, a dedicated regulatory framework for PoC manufacturing is still lacking. Healthcare institutions face uncertainty about which standards are mandatory, how to adapt QMS principles to small-scale units and how to demonstrate conformity for devices produced on demand. As a result, PoC laboratories currently apply heterogeneous approaches to documentation, validation, verification and release. A harmonized and universally recognized regulatory pathway would therefore be essential to ensure consistent safety and performance across clinical settings.

2.3 Proposals from the Literature: Quality Control Methods Adopted

Given the gaps in standardization and verification identified in the previous subchapters, several studies have proposed several approaches to support Quality Control (QC) within Point-of-Care (PoC) 3D printing environments. These contributions aim to ensure that each stage of the workflow, from imaging to post-processing, maintains sufficient consistency and accuracy to allow the safe use of 3D-printed medical models and devices in clinical practice. The literature consistently highlights that QC cannot be limited to post-printing inspection but must instead be distributed throughout the entire production chain [66], [67], [68].

Based on the experiences reported in these studies, the main phases of PoC manufacturing can be described as a sequence of steps, each associated with specific sources of error and verification tasks. This structure is often represented through workflow-based models that outline how Quality Assurance (QA) actions should be integrated across imaging, segmentation, modelling, printing and post-processing. The analysis of existing publications shows that these frameworks are not intended as universally accepted protocols but as conceptual tools that consolidate the most recurrent verification strategies described in the literature. These frameworks summarize recurring practices from multiple international studies describing both the general structure of QA in medical 3D printing and the specific verification steps adopted in PoC contexts [69], [70].

Several authors have contributed specific proposals for QC at different stages of the workflow. Schulze et al. presented one of the most comprehensive frameworks, identifying distinct sources of error from image acquisition to post-processing and associating each phase with targeted verification methods. Their work emphasizes that both digital and physical steps introduce errors that must be accounted for within hospital-based manufacturing units [66]. Building on this perspective, Wilkat et al. developed an in-house workflow for producing patient-specific aortic models. They introduced critical verification steps related to sterilization, deformation analysis and

microstructural integrity assessment following post-processing, highlighting the need to evaluate how cleaning and curing influence anatomical fidelity and mechanical behavior [71].

Further contributions explore the integration of extended QA structures. Martinez-Marquez et al. proposed an 18-step system of "quality gates" distributed across the design and fabrication stages of patient-specific implants. These gates include structured checkpoints, process validation steps and real-time monitoring actions intended to prevent error propagation throughout the workflow. Their work demonstrates the importance of formalizing intermediate controls rather than relying solely on final inspection [72]. Complementing these approaches, Wang et al. expanded the validation phase by introducing quantitative and qualitative performance tests, including haptic assessment of tactile realism, drilling resistance and usability of printed models during surgical simulation. Their work underscores the importance of incorporating end-user perception and functional feedback as essential elements of final QC [73].

Altogether, these contributions outline a multilayered pathway for QC in PoC 3D printing. They collectively describe how imaging, segmentation, digital modelling, fabrication, post-processing, sterilization and clinical validation contribute to the accuracy and reliability of the final printed device. While these frameworks differ in single steps, they converge on the need to integrate both preventive and corrective QC actions. They also recognize that principles of verification, traceability, consistency and error mitigation, are common across PoC manufacturing workflows. When the various steps discussed in the literature are unified and interpreted together, they can be summarized into a consistent QC workflow that reflects the shared structure of the main proposals. This interpretation is here represented in the flow diagram shown in Figure 2.2, which aggregates the recurring steps and verification points into a single proposed quality control protocol for 3D printing PoC.

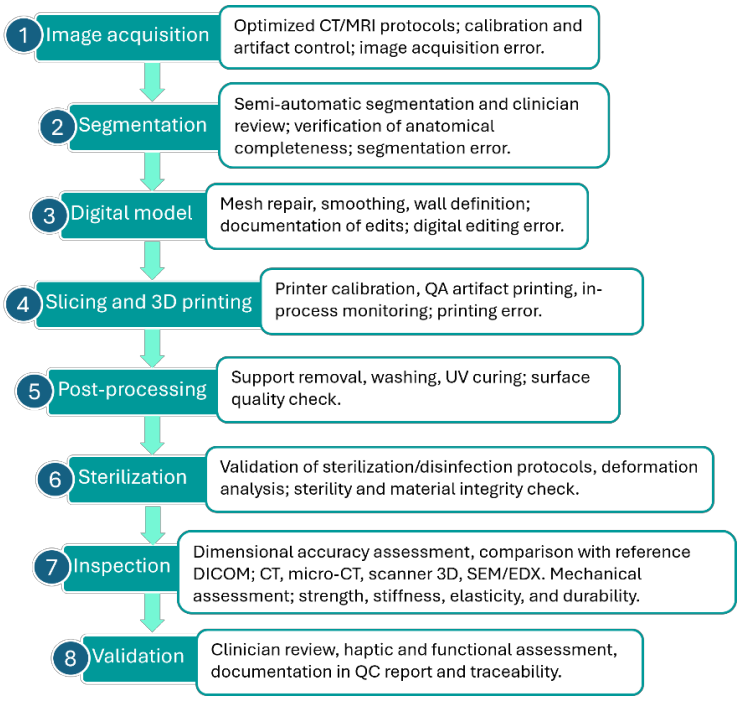

Figure 2.2. The original flowchart illustrates a complete workflow for 3D printing quality control PoC, integrating and unifying key contributions and process steps reported in the literature, including error classification and verification from imaging to post-processing [66], sterilization validation and microstructural integrity checks [71], integrated quality gates and process validation [72], and the inclusion of haptic and functional assessment as part of the final validation stage of patient-specific models [73].

Although the individual quality control steps represented in the flowchart in Figure 2.2 have been discussed separately in the existing literature, their integration into a single, structured and coherent workflow represents an original contribution of the present work. By organizing these steps into a clear sequence with defined verification points, the diagram offers a practical reference that is currently missing from the literature. For this reason, it should be regarded not only as a summary of existing approaches, but as a conceptual contribution that enhances clarity, comparability and applicability of QC strategies in PoC environments. The proposals of the present work also highlight persistent variability in methods, metrics and acceptance threshold an examination of the systemic issues that continue to limit standardization in clinical additive manufacturing. These emerging gaps are discussed below, providing a critical overview of the main technical, procedural and organizational barriers that still affect PoC 3D printing and motivate the experimental work developed in this thesis.

2.4 Emerging Issues and Gaps

Despite major advances in defining quality control (QC) workflows for point-of-care (PoC) 3D printing, several systemic and cross-cutting challenges remain unresolved. When each stage of the workflow is examined individually, persistent gaps can be identified across imaging, segmentation, modelling, printing, post-processing, sterilization and regulatory compliance. These limitations continue to restrict the standardization, reproducibility and safe implementation of PoC manufacturing.

At the image acquisition stage, variability in Computed Tomography (CT) and Magnetic Resonance Imaging (MRI) protocols, including slice thickness, spatial resolution and artefacts, directly affects the fidelity of the final anatomical model [74]. Inadequate imaging parameters have been shown to increase segmentation and modelling error propagation, particularly in cases where texture noise or motion artefacts compromise anatomical definition [75].

In the segmentation phase, large method and operator-dependent variability persists. While semi-automatic segmentation tools may reduce processing time, their performance is strongly dependent on image quality and anatomical complexity, leading to inconsistent results between users and even within the same workflow [76]. Errors introduced in segmentation propagate through every subsequent step and are difficult to isolate once the model reaches the printing stage.

Additional gaps are evident during slicing and 3D printing. Issues such as incomplete printer calibration, inconsistent parameter settings, material batch variability and the near absence of in-process monitoring are still reported in many PoC environments [77]. These factors introduce uncontrolled variability that affects dimensional accuracy, internal structures and overall model reliability.

In post-processing support removal, washing, UV curing and surface finishing quantitative methods to assess deformation, residual stress or microstructural heterogeneities are still lacking [78]. Since many PoC units rely on manual or semi-manual procedures, post-processing remains one of the stages with the highest potential for geometric drift or mechanical alteration, yet it remains poorly characterized in the literature.

Beyond technical aspects, regulatory and organizational constraints represent major obstacles to the implementation of harmonized PoC workflows. As soon as technologies, materials and workflow-specific issues are identified, the absence of a clear regulatory framework becomes the main barrier to uniformity. Reviewing the state of mechanical testing in biomedical additive

manufacturing, Neussl et al. identified the lack of harmonized test standards and called for the development of consistent QC protocols to ensure inter-laboratory reproducibility [79].

This regulatory gap is particularly evident in personalized and patient-matched device production. Current international frameworks are poorly aligned with the individualized nature of PoC manufacturing, where each device is produced for a single patient under dynamic conditions. Traditional regulations were designed for mass-manufactured devices validated as finished products, whereas PoC 3D printing requires the regulation of an entire production workflow. In Europe, the Medical Device Regulation (MDR 2017/745) [26] addresses in-house manufacturing through the Health Institute Exemption [80], shifting regulatory responsibility directly to the hospital. This obliges healthcare institutions to implement quality management, comply with safety and performance requirements and justify the absence of a suitable commercial alternative. Hospitals therefore become de facto medical device manufacturers, often without the organizational structure, expertise in risk management or documentation systems required for regulatory compliance. The operational burden and associated costs significantly limit implementation.

Human and economic factors add further complexity. The lack of standardized training and certification pathways results in a shortage of qualified professionals capable of managing clinical, engineering and quality aspects of PoC production. Economic constraints, including the high initial investment, infrastructure requirements and absence of reimbursement mechanisms, reduce adoption to a small number of well-resourced centers [81].

A critical and often underestimated gap concerns sterilization. Sterilization is mandatory for any device intended for use in sterile environments, yet existing standards were developed for conventional manufacturing and do not account for the material variability, surface porosity or microstructure typical of additively manufactured polymers. No harmonized guidance currently defines validated sterilization techniques for AM materials or standardized methods to assess the impact of sterilization on dimensional accuracy and mechanical integrity. This limitation poses a major barrier to clinical use, especially for surgical guides and intraoperative models.

In summary, the literature shows that no universal framework exists for reporting, verification and sterilization in point-of-care manufacturing. The absence of harmonized regulatory guidance, validated protocols and shared quality control criteria remains one of the main barriers to the safe and reproducible adoption of clinical 3D printing. These gaps also clarify why this thesis concentrates specifically on dimensional and mechanical assessment. Among all stages of the

workflow, these two phases represent the most quantifiable and reproducible components of quality control, and they provide measurable indicators that can be used to evaluate variability, compare technologies and support decision-making. Focusing on dimensional fidelity and mechanical behavior addresses a fundamental limitation highlighted in the literature: the absence of a unified and consistent set of quantitative parameters that could support PoC laboratories in evaluating the accuracy and performance of their printed models and devices. Proposing shared measurement procedures and preliminary acceptance thresholds can reduce variability and provide a basis for quality decisions in clinical settings. In this thesis Chapter 3 describes the workflow adopted to manufacture anatomical models and mechanical samples. Chapter 4 develops a quantitative dimensional assessment, analyzing the variability introduced by segmentation, printing and post-processing. Chapter 5 extends the investigation to mechanical behavior, examining stiffness, elasticity and time-dependent responses with the aim of proposing preliminary acceptance threshold that can contribute to future QC frameworks for 3D PoC printing.

References

[1] *Additive manufacturing — General principles — Fundamentals and vocabulary*, ISO/ASTM 52900:2021, Nov. 2021.

[2] R. Kumar, H. Mehdi, S. S. Bhati, M. Arunkumar, S. Mishra, and M. K. Lohumi, "A comprehensive review of advancements in additive manufacturing for 3D printed medical components using diverse materials," *Discov. Mater.*, vol. 5, no. 1, p. 152, Aug. 2025, doi: 10.1007/s43939-025-00349-w.

[3] A. Q. A. Teo, D. Q. K. Ng, P. Lee, and G. K. O'Neill, "Point-of-Care 3D Printing: A Feasibility Study of Using 3D Printing for Orthopaedic Trauma," *Injury*, vol. 52, no. 11, pp. 3286–3292, Nov. 2021, doi: 10.1016/j.injury.2021.02.041.

[4] D. Ostaş *et al.*, "Point-of-Care Virtual Surgical Planning and 3D Printing in Oral and Cranio-Maxillofacial Surgery: A Narrative Review," *J. Clin. Med.*, vol. 11, no. 22, p. 6625, Nov. 2022, doi: 10.3390/jcm11226625.

[5] T. Kermavnar, A. Shannon, K. J. O'Sullivan, C. McCarthy, C. P. Dunne, and L. W. O'Sullivan, "Three-Dimensional Printing of Medical Devices Used Directly to Treat Patients: A Systematic Review," *3D Print. Addit. Manuf.*, vol. 8, no. 6, pp. 366–408, Dec. 2021, doi: 10.1089/3dp.2020.0324.

[6] T. Kermavnar, A. Shannon, K. J. O'Sullivan, C. McCarthy, C. P. Dunne, and L. W. O'Sullivan, "Three-Dimensional Printing of Medical Devices Used Directly to Treat Patients: A Systematic Review," *3D Print. Addit. Manuf.*, vol. 8, no. 6, pp. 366–408, Dec. 2021, doi: 10.1089/3dp.2020.0324.

[7] A. Valls-Esteve *et al.*, "Point-of-care additive manufacturing: state of the art and adoption in Spanish hospitals during pre to post COVID-19 era," *3D Print. Med.*, vol. 10, no. 1, p. 43, Dec. 2024, doi: 10.1186/s41205-024-00244-9.

[8] F. Ali, S. N. Kalva, and M. Koc, "Advancements in 3D printing techniques for biomedical applications: a comprehensive review of materials consideration, post processing, applications, and challenges," *Discov. Mater.*, vol. 4, no. 1, p. 53, Oct. 2024, doi: 10.1007/s43939-024-00115-4.

[9] S. Hatamikia *et al.*, "Realistic 3D printed CT imaging tumor phantoms for validation of image processing algorithms," *Phys. Med.*, vol. 105, p. 102512, Jan. 2023, doi: 10.1016/j.ejmp.2022.102512.

[10] M. Cecchitelli *et al.*, "First development of a LMHF vibration system for cell incubators," in *2024 IEEE International Workshop on Metrology for Industry 4.0 & IoT (MetroInd4.0 & IoT)*, Firenze, Italy: IEEE, May 2024, pp. 17–21. doi: 10.1109/MetroInd4.0IoT61288.2024.10584246.

[11] U. Urbani *et al.*, "Preliminary quantitative assessment of surgical outcomes in Craniosynostosis correction procedures: A 3D-Morphometric comparison," *J. Cranio-Maxillofac. Surg.*, vol. 53, no. 8, pp. 1029–1036, Aug. 2025, doi: 10.1016/j.jcms.2025.03.012.

[12] R. Uomo *et al.*, "Evaluation of mandibular morphology in untreated growing patients with hemifacial Microsomia: a 3D computed tomography study," *J. Cranio-Maxillofac. Surg.*, p. 104416, Dec. 2025, doi: 10.1016/j.jcms.2025.11.019.

[13] M. S. Kumar, M. U. Farooq, N. S. Ross, C.-H. Yang, V. Kavimani, and A. A. Adediran, "Achieving effective interlayer bonding of PLA parts during the material extrusion process with enhanced mechanical properties," *Sci. Rep.*, vol. 13, no. 1, p. 6800, Apr. 2023, doi: 10.1038/s41598-023-33510-7.

[14] I.-A. Timofticiuc *et al.*, "Biomaterials Adapted to Vat Photopolymerization in 3D Printing: Characteristics and Medical Applications," *J. Funct. Biomater.*, vol. 15, no. 1, p. 7, Dec. 2023, doi: 10.3390/jfb15010007.

[15] M. Topa-Skwarczyńska and J. Ortyl, "Photopolymerization shrinkage: strategies for reduction, measurement methods and future insights," *Polym. Chem.*, vol. 14, no. 18, pp. 2145–2158, 2023, doi: 10.1039/D3PY00261F.

[16] R. J. N. Joshua *et al.*, "Powder Bed Fusion 3D Printing in Precision Manufacturing for Biomedical Applications: A Comprehensive Review," *Materials*, vol. 17, no. 3, p. 769, Feb. 2024, doi: 10.3390/ma17030769.

[17] Y. Song, Y. Ghafari, A. Asefnejad, and D. Toghraie, "An overview of selective laser sintering 3D printing technology for biomedical and sports device applications: Processes, materials, and applications," *Opt. Laser Technol.*, vol. 171, p. 110459, Apr. 2024, doi: 10.1016/j.optlastec.2023.110459.

[18] M. Curto, J. Dowsett, A. P. Kao, G. Tozzi, and A. H. Barber, "Multi-material 3D printed composites inspired by nacre: a hard/soft mechanical interplay," *Sci. Rep.*, vol. 15, no. 1, p. 6728, Feb. 2025, doi: 10.1038/s41598-025-91080-2.

[19] S. Chokshi *et al.*, "Medical 3D Printing Using Material Jetting: Technology Overview, Medical Applications, and Challenges," *Bioengineering*, vol. 12, no. 3, p. 249, Feb. 2025, doi: 10.3390/bioengineering12030249.

[20] X. Guan, C. Liu, T. F. Sheng, Y. H. Beh, and I. M. Tew, "Innovative Stackable Multijet-Printed Templates for Precise Veneer Preparation: A Dental Technique," *Appl. Sci.*, vol. 15, no. 9, p. 4975, Apr. 2025, doi: 10.3390/app15094975.

[21] G. Molinari *et al.*, "Assessment of a novel patient-specific 3D printed multi-material simulator for endoscopic sinus surgery," *Front. Bioeng. Biotechnol.*, vol. 10, p. 974021, Nov. 2022, doi: 10.3389/fbioe.2022.974021.

[22] O. G. Ruiz and Y. Dhaher, "Multi-color and Multi-Material 3D Printing of Knee Joint models," *3D Print. Med.*, vol. 7, no. 1, p. 12, Dec. 2021, doi: 10.1186/s41205-021-00100-0.

[23] O. Gülcan, K. Günaydın, and A. Tamer, "The State of the Art of Material Jetting—A Critical Review," *Polymers*, vol. 13, no. 16, p. 2829, Aug. 2021, doi: 10.3390/polym13162829.

[24] "Ministry of Food and Drug Safety>Our Works>Medical Devices>Regulations> View Details | Ministry of Food and Drug Safety." Accessed: Nov. 03, 2025. [Online]. Available: https://www.mfds.go.kr/eng/brd/m_40/view.do?seq=72619&srchFr=&srchTo=&srchWord=&srchTp=&itm_seq_1=0&itm_seq_2=0&multi_itm_seq=0&company_cd=&company_nm=/1000&page=1

[25] *Publication of Guidance for the Evaluation of Emerging Technology Medical Devices/Regenerative Medical Products*, PFSB/ELD/OMDE/CMS (Yakushokukisan) Notification 0925 No.1, Sept. 2015.

[26] "Regulation - 2017/745 - EN - Medical Device Regulation - EUR-Lex." Accessed: Oct. 29, 2025. [Online]. Available: https://eur-lex.europa.eu/eli/reg/2017/745/oj/eng

[27] *Technical Considerations for Additive Manufactured Medical Devices*, Dec. 2017.

[28] *Biological evaluation of medical devices - Part 1: Evaluation and testing within a risk management process*, ISO 10993-1:2018, Aug. 2018.

[29] *Implants for surgery — Cleanliness of orthopedic implants — General requirements*, ISO 19227:2018, Mar. 2018.

[30] *Digital Imaging and Communications in Medicine (DICOM) Supplement 205: DICOM Encapsulation of STL Models for 3D Manufacturing*, Apr. 2018.

[31] *Guidance Document - Supporting Evidence for Implantable Medical Devices Manufactured by 3D Printing*, Apr. 2019.

[32] *Guidelines for Technical Review of the Registration of CustomMade and Material Additive-Based Medical Devices of Passive Implantable Bones, Joints and Oral Hard Tissues.*, Oct. 2019.

[33] *Standard Guide for Assessing the Removal of Additive Manufacturing Residues in Medical Devices Fabricated by Powder Bed Fusion*, ASTM F3335-20, Mar. 2020.

[34] *Clinical investigation of medical devices for human subjects — Good clinical practice*, ISO 14155: 2020, July 2020.

[35] *Digital Imaging and Communications in Medicine (DICOM) Supplement 208: DICOM Encapsulation of OBJ Models for 3D Manufacturing and Virtual Reality*, Jan. 2020.

[36] Health Sciences Authority, *Regulatory Guideline for 3D printed Medical Devices*, July 2021.

[37] *Medical devices - Part 1: Application of usability engineering to medical devices*, IEC 62366-1:2015, Feb. 2015.

[38] *Medical devices — Quality management systems — Requirements for regulatory purposes*, ISO 13485:2021, Nov. 2021.

[39] *Additive manufacturing — Qualification principles — Installation, operation and performance (IQ/OQ/PQ) of PBF-LB equipment*, ISO/ASTM TS 52930:2021, Nov. 2021.

[40] *Questions and Answers on Custom-Made Devices*, MDCG 2021-3, Mar. 2021.

[41] *Disposizioni per l'adeguamento della normativa nazionale alle disposizioni del regolamento (UE) 2017/745 del Parlamento europeo e del Consiglio, del 5 aprile 2017, relativo ai dispositivi medici, che modifica la direttiva 2001/83/CE, il regolamento (CE) n. 178/2002 e il regolamento (CE) n. 1223/2009 e che abroga le direttive 90/385/CEE e 93/42/CEE del Consiglio, nonche' per l'adeguamento alle disposizioni del regolamento (UE) 2020/561 del Parlamento europeo e del Consiglio, del 23 aprile 2020, che modifica il regolamento (UE) 2017/745 relativo ai dispositivi medici, per quanto riguarda le date di applicazione di alcune delle sue disposizioni ai sensi dell'articolo 15 della legge 22 aprile 2021, n. 53.*, Legislative Decree 137/2022, Semptember 2022.

[42] *Personalized Medical Devices – Production Verification and Validation*, IMDRF/PMD WG/N74, Apr. 2023.

[43] *Additive manufacturing — Qualification principles — Requirements for industrial additive manufacturing processes and production sites*, ISO/ASTM 52920:2023, June 2023.

[44] *Standard Guide for Directed Energy Deposition of Metals*, ASTM F3187-16, Feb. 2024.

[45] *Sterilization of health-care products — Ethylene oxide — Requirements for the development, validation and routine control of a sterilization process for medical devices*, ISO 11135:2014, July 2014.

[46] *Non-active surgical implants — General requirements*, ISO 14630:2024, Sept. 2024.

[47] *Additive manufacturing of metals — Process characteristics and performance — Metal powder bed fusion process to meet critical applications*, ISO/ASTM 52904:2024, Nov. 2024.

[48] *Additive manufacturing of metals — Finished part properties — Orientation and location dependence of mechanical properties for metal parts*, ISO/ASTM 52909:2024, Feb. 2024.

[49] *Additive manufacturing — General principles — Main characteristics and corresponding test methods*, ISO/ASTM 52927:2024, Mar. 2024.

[50] *Additive manufacturing of metals— Feedstock materials — Powder life cycle management*, ISO/ASTM 52928:2024, May 2024.

[51] C. for D. and R. Health, "Quality Management System Regulation: Final Rule Amending the Quality System Regulation – Frequently Asked Questions," *FDA*, Aug. 2025, Accessed: Oct. 29, 2025. [Online]. Available: https://www.fda.gov/medical-devices/quality-system-qs-regulationmedical-device-current-good-manufacturing-practices-cgmp/quality-management-system-regulation-final-rule-amending-quality-system-regulation-frequently-asked

[52] *Medical devices — Application of risk management to medical devices*, ISO 14971:2019, Dec. 2019.

[53] *Sterilization of health care products — Radiation Part 1: Requirements for the development, validation and routine control of a sterilization process for medical devices*, ISO 11137-1:2025, Apr. 2025.

[54] *Additive manufacturing for medical — General principles — Additive manufacturing of non-active implants*, ISO 5092:2025, Sept. 2025.

[55] T. G. Administration (TGA), "Medical devices reforms: personalised medical devices | Therapeutic Goods Administration (TGA)." Accessed: Nov. 03, 2025. [Online]. Available: https://www.tga.gov.au/products/regulations-all-products/tga-reforms/medical-devices-reforms/medical-devices-reforms-personalised-medical-devices

[56] *Additive manufacturing for medical — General principles — Additive manufacturing of non-active implants*, ISO/ASTM 52929:2025, 2025.

[57] *New Test Methods for the Characterization of Powder Flow Properties for Additive Manufacturing Applications*, ASTM WK55610.

[58] *Feedstock Materials-Creating Feedstock Specifications for Metal Powder Bed Fusion*, WK 58219.

[59] *Feedstock Materials Technical specifications on Metal powder*, WK 62190.

[60] *Guide for Design for Material Extrusion Processes*, WK 62867.

[61] *Additive Manufacturing Design – Decision Guide*, WK 64190.

[62] *Standard Guidlines Laser Powder Bed Fusion (L-PBF) for Metal.*

[63] *Medical devices — Quality management systems — Requirements for regulatory purposes*, ISO 13485: 2016, Mar. 2016.

[64] T. G. Administration (TGA), "Therapeutic Goods Administration (TGA) | Australian Government Department of Health." Accessed: Nov. 03, 2025. [Online]. Available: https://www.tga.gov.au/therapeutic-goods-administration-tga

[65] "Welcome to Ministry of Health, Labour and Welfare." Accessed: Nov. 03, 2025. [Online]. Available: https://www.mhlw.go.jp/english/

[66] M. Schulze *et al.*, "Quality assurance of 3D-printed patient specific anatomical models: a systematic review," *3D Print. Med.*, vol. 10, no. 1, p. 9, Mar. 2024, doi: 10.1186/s41205-024-00210-5.

[67] V. A. Sears and J. M. Morris, "Establishing a Point-of-Care Virtual Planning and 3D Printing Program," *Semin. Plast. Surg.*, vol. 36, no. 03, pp. 133–148, Aug. 2022, doi: 10.1055/s-0042-1754351.

[68] D. J. Thomas and D. Singh, "3D printing for developing patient specific cosmetic prosthetics at the point of care," *Int. J. Surg.*, vol. 80, pp. 241–242, Aug. 2020, doi: 10.1016/j.ijsu.2020.04.023.

[69] B. G. Beitler *et al.*, "Interpretation of regulatory factors for 3D printing at hospitals and medical centers, or at the point of care," *3D Print. Med.*, vol. 8, no. 1, p. 7, Dec. 2022, doi: 10.1186/s41205-022-00134-y.

[70] Z. Jin, C. He, J. Fu, Q. Han, and Y. He, "Balancing the customization and standardization: exploration and layout surrounding the regulation of the growing field of 3D-printed medical

devices in China," *Bio-Des. Manuf.*, vol. 5, no. 3, pp. 580–606, July 2022, doi: 10.1007/s42242-022-00187-2.

[71] M. Wilkat *et al.*, "Accuracy and Sterilizability of In-House Printed Patient-Specific Aortic Model for Surgeon-Modified Stent Grafts—A Workflow Description for Emergency Aortic Endovascular Procedures," *J. Clin. Med.*, vol. 13, no. 5, p. 1309, Feb. 2024, doi: 10.3390/jcm13051309.

[72] D. Martinez-Marquez, M. Jokymaityte, A. Mirnajafizadeh, C. P. Carty, D. Lloyd, and R. A. Stewart, "Development of 18 Quality Control Gates for Additive Manufacturing of Error Free Patient-Specific Implants," *Materials*, vol. 12, no. 19, p. 3110, Sept. 2019, doi: 10.3390/ma12193110.

[73] X. Wang, S. Shujaat, E. Shaheen, and R. Jacobs, "Quality and haptic feedback of three-dimensionally printed models for simulating dental implant surgery," *J. Prosthet. Dent.*, vol. 131, no. 4, pp. 660–667, Apr. 2024, doi: 10.1016/j.prosdent.2022.02.027.

[74] A. Streckenbach *et al.*, "Current State and Outlook in Medical 3D Printing and the Role of Radiology," *RöFo - Fortschritte Auf Dem Geb. Röntgenstrahlen Bildgeb. Verfahr.*, vol. 197, no. 07, pp. 770–780, July 2025, doi: 10.1055/a-2436-7185.

[75] T. Saini, P. S. Shiakolas, and C. McMurrough, "Evaluation of Image Segmentation Methods for In Situ Quality Assessment in Additive Manufacturing," *Metrology*, vol. 4, no. 4, pp. 598–618, Nov. 2024, doi: 10.3390/metrology4040037.

[76] M. Fogarasi, J. C. Coburn, and B. Ripley, "Algorithms used in medical image segmentation for 3D printing and how to understand and quantify their performance," *3D Print. Med.*, vol. 8, no. 1, p. 18, Dec. 2022, doi: 10.1186/s41205-022-00145-9.

[77] W. L. Ng, J. An, and C. K. Chua, "Process, Material, and Regulatory Considerations for 3D Printed Medical Devices and Tissue Constructs," *Engineering*, vol. 36, pp. 146–166, May 2024, doi: 10.1016/j.eng.2024.01.028.

[78] A. Kantaros, T. Ganetsos, F. Petrescu, L. Ungureanu, and I. Munteanu, "Post-Production Finishing Processes Utilized in 3D Printing Technologies," *Processes*, vol. 12, no. 3, p. 595, Mar. 2024, doi: 10.3390/pr12030595.

[79] T. Neussl *et al.*, "Quality approaches and standards of 3D printing in orthopedic and traumatological settings: a systematic review," *Explor. Musculoskelet. Dis.*, vol. 3, p. 100794, June 2025, doi: 10.37349/emd.2025.100794.

[80] European Parliament and Council of the European Union, *Regulation (EU) 2017/745 on medical devices and amending Directive 2001/83/EC, Regulation (EC) No 178/2002 and Regulation (EC) No 1223/2009, Article 5(5), Official Journal of the European Union, vol. L 117, pp. 1–175, May 5, 2017*.

[81] C. Serrano, S. Fontenay, H. van den Brink, J. Pineau, P. Prognon, and N. Martelli, "Evaluation of 3D printing costs in surgery: a systematic review," *Int. J. Technol. Assess. Health Care*, vol. 36, no. 4, pp. 349–355, 2020, doi: 10.1017/S0266462320000331.

Chapter 3

3D Printing Experimental Activities

3.1 3D Printing Workflow in Hospital Environments

The experimental activities carried out during this doctoral program took place mainly within a Point-of-Care (PoC) 3D printing laboratory, currently under development, at a pediatric hospital, with the intention of adopting additive manufacturing (AM) to support diagnostic imaging, surgical planning and training. This environment provided access to medical imaging systems, segmentation workstations and multiple 3D printers, enabling a complete implementation of the digital-to-physical workflow described in current biomedical literature on 3D printing for surgical planning and patient-specific treatments [1], [2].

In this context, the workflow followed in this chapter is based on that reported in the literature and summarized in Chapter 2, starting with the acquisition of computed tomography (CT) and continuing with segmentation, mesh optimization, 3D printing and post-processing (Figure 3.1).

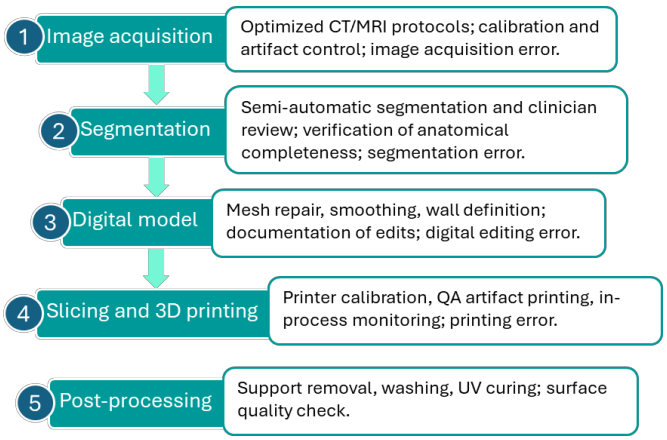

Figure 3.1. Extract of the PoC 3D-printing workflow adopted in this chapter, illustrating the five sequential steps from medical image acquisition to post-processing of the printed model. Each step highlights the key operations and associated sources of error that may affect the dimensional and mechanical fidelity of the final model.

A significant part of the workflow refinement originated from early studies performed on cranial models fabricated with fused deposition modelling (FDM). These studies confirmed the need for

quality control procedures and highlighted the absence of standardized protocols for PoC 3D printing in healthcare [3], [4], [5].

The skull-based experiments revealed how segmentation thresholds, mesh smoothing, layer height selection and support strategies influence dimensional fidelity, especially for thin or highly curved structures. This experience influenced the strategies adopted later for all other models, including bone replicas and soft-tissue structures.

As the research progressed, the workflow was extended to more complex anatomical regions requiring high geometric accuracy and controlled mechanical behavior. In particular, the reconstruction and fabrication of pediatric trachea models relied on Stereolithography (SLA) technology and flexible photopolymers, an approach aligned with the increasing use of soft 3D-printed anatomical replicas reported in the literature for surgical simulation and preoperative training [6], [7], [8]. These applications demonstrate how soft polymers and elastomers, although promising for tissue-mimicking models, require dedicated mechanical characterization due to the nonlinear behavior of the materials and the absence of standards for specimen preparation and testing [9], [10].

Collaboration with external partners has also enabled the inclusion of elastomeric samples printed with PolyJet technology. These samples were designed in-house and used to compare different printing technologies and understand how the orientation of the material jet deposition affects mechanical response.

The hospital environment in which these activities were conducted imposed typical constraints of real clinical workflows. Computed Tomography (CT) scans often follow pediatric low-dose protocols, which introduced noise and lower contrast, that have been shown to affect segmentation accuracy and automatic threshold-based 3D model extraction [11], [12]. Similarly, when evaluating the proposed workflow under realistic operating conditions, particular attention was also paid to reproducing the production pressures typical of hospital 3D printing units. For this reason, the experimental activities included tests performed on models printed under deliberately high productivity conditions, using fast printing profiles but relying on a properly maintained and calibrated machine. This approach is aimed at reflecting the intensive workloads that a clinical PoC laboratory may routinely experience.

Overall, the 3D printing workflow implemented in this dissertation is the result of iterative refinement across different anatomical models and materials, each contributing to the investigation of source of errors depending on segmentation, manufacturing variability, and post-processing

effects. This workflow forms the practical basis on which the dimensional assessment (Chapter 4) and the mechanical assessment (Chapter 5) were developed.

3.2 Segmentation and Digital Model

Segmentation and digital modelling constitute the first operational block of the PoC 3D printing workflow implemented in this thesis. They represent the first stage, in which imaging data is transformed into printable geometries, and is the first source of error that will propagate in dimensional or mechanical evaluations.

The segmentation phase in hospital, especially in pediatrics, where CT acquisition protocols have stringent constraints, directly influences the geometric fidelity of the resulting anatomical model, as it is highly dependent on both the quality of the images acquired and the operator performing it manually. The workflow begins with image acquisition where CT datasets, step 1 of the flowchart in Figure 3.1, were exclusively employed as the imaging source throughout all the applications considered in this work.

Following acquisition, the process moved to segmentation, step 2 of the flowchart in Figure 3.1, a critical step in which the anatomical region of interest is isolated from the volumetric imaging data to generate the 3D representation suitable for digital modelling and, ultimately, 3D printing. Segmentation involves identifying voxel clusters that correspond to specific anatomical structures based on intensity thresholds and local geometric features. In this context, masks represent the binary volumetric regions generated during segmentation; they define which voxels belong to the structure of interest and serve as the basis for the subsequent 3D surface reconstruction. The accuracy of these masks directly affects the fidelity of the final STL model.

Across the studies included in this dissertation, segmentation was carried out using Materialise Mimics (versions 25.0 and 26.0), the certified medical imaging software available in the PoC laboratory. All segmentations were performed through semi-automatic thresholding combined with mask refinement and every generated mask was subsequently reviewed and clinically validated by an experienced radiologist to ensure anatomical accuracy and consistency with the original CT data.

Once segmentation masks were validated, they were converted into the digital model through mesh extraction and optimization, step 3 of the flowchart in Figure 3.1, the mesh being the polygonal surface representation of the segmented anatomy composed of interconnected triangles that define the geometry of the object, before proceeding with further processing. Across all applications, exported STL files were cleaned using Autodesk Meshmixer, a mesh-editing software widely used for basic surface correction and defect removal, and then optimized in Materialise 3-

matic (version 17.0), an advanced engineering tool for mesh refinement, geometric editing, and preparation of medical models for 3D printing, through mesh repair, smoothing, hole closure and wall-definition procedures. The degree of smoothing and correction was intentionally kept to a minimum to avoid hiding the actual anatomical variability or introducing artificial regularities.

The following subsections describe how this workflow was applied to the different anatomical and test models produced during the doctoral work, namely the cranial, clavicle and airway models, together with the dog-bone, cylindrical and anatomically shaped specimens, highlighting the specific segmentation strategies, modelling choices and objectives associated with each case study.

3.2.1 Cranial Model

The cranial model represents the starting point for the experimental activities conducted in this doctoral research and constitutes the first structured attempt at dimensional investigation conducted on 3D-printed anatomical models in a PoC setting. Its development preceded all subsequent case studies in the thesis and was used to investigate how segmentation, digital modelling, slicing and fused deposition modelling (FDM) parameters influence the geometric fidelity of a printed Polylactic Acid (PLA) object with respect to its original anatomy.

The cranial model was selected for several reasons: its widespread use in cranio-maxillofacial surgery and biomedical education, its morphological complexity with thin walls, cavities and curved surfaces, and its sensitivity to segmentation and printing choices [13]. These features made it suitable for investigating the sources of variability inherent in the digital preparation and fabrication workflow. A first study was presented as a preliminary quality control approach, in which a reference cranial model was digitally reconstructed and 3D printed. The dimensional evaluation was conducted between the reference model and its replicas using image-based comparison methods.

The cranial model served as a reference was 3D printed from the CT data (Siemens Somatom Force® dual source tomograph [14]) of an anonymous diagnostic examination performed on an 8-year-old patient under a pediatric low-dose protocol. As noted in the biomedical study, such acquisition settings minimize radiation exposure but reduce contrast making the dataset unsuitable as a direct dimensional reference comparison. For this reason, the patient diagnostic scan served exclusively as the basis for deriving the digital "reference skull model", later used to generate all subsequent replicas (Figure 3.2). In addition, the decision not to use this data as a reference also lies in the fact that patient images may be affected by interference due to both the presence of soft tissue and the different X-ray response of bone to the print material.

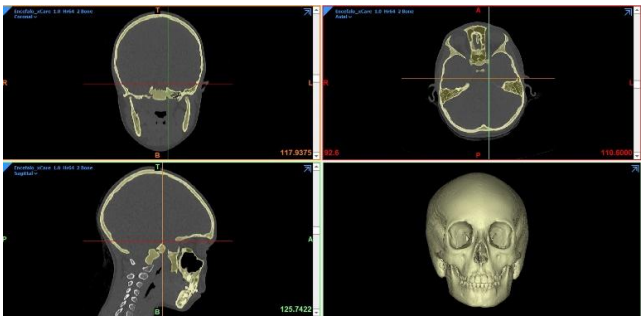

Figure 3.2. 3D reconstruction of the "reference skull model" from axial, coronal and sagittal views from the anonymous patient CT examination.

The DICOM dataset was imported into a specialized medical 3D image segmentation software, i.e., Mimics Materialise 25.0 (Leuven, Belgium) [15]. The digital segmentation was accomplished using a semi-automated technique. To ensure that the 3DP model was suitable for the reference purpose, the 3D reconstruction of the skull from CT images was exported to Autodesk Meshmixer [16] and subjected to manual smoothing to remove surface blemishes and irregularities. To reduce material use and printing time while preserving anatomical details, the skull model was scaled down to 75% of its original size. To obtain the digital model, the segmented object was exported to Medical 3-matic 17.0 [17] and converted to an optimized STL file (Figure 3.3), minimizing artifacts like stitching, holes and overlaps, suitable for the print file (.3mf).

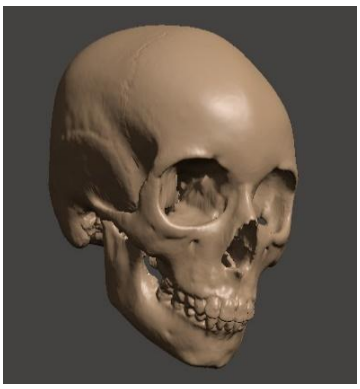

Figure 3.3. The digital "reference skull model".

In the skull's replica workflow, the reference skull model was subjected to CT scan acquisition with the aim to maximize the image resolution. The CT protocol adopted for this acquisition is reported in Table 3.1. The segmentation was repeated eight times starting from the same reference skull model CT dataset, allowing the generation of eight STL files used to fabricate independent replicas.

This procedure enabled the investigation of variability introduced specifically by segmentation decisions.

Table 3.1. Main reference skull model CT scanning protocol settings.

CT parameter	Setting
Total number of slices	263
Slice thickness	0.5 mm
Slice increment	0.5 mm
Pixel size	0.35 × 0.35 mm^2
Field of view	180 mm
Voltage peak	90 kV
Single collimation width	0.59 mm
Step factor	0.55

A custom Hounsfield Unit threshold (-802 to 739 HU) was systematically applied to match the PLA radiodensity of the scanned reference skull model, ensuring consistency in skull segmentation. The HU values are universally employed in CT scanning to quantify the radiodensity of anatomical structures [18]. These values are linearly correlated with the grayscale of CT images, providing a direct and quantifiable measure of tissue density [19]. Segmented objects were automatically wrapped and smoothed several times with identical settings to maintain uniformity. Again, all eight segmented models were imported into Medical 3-matic 17.0 [17] to optimize the mesh and save the STL files for printing.

3.2.2 Clavicle Model

After reconstructing the cranial model, which served as the starting point for investigating the segmentation and digital modelling workflow, the second case study focused on the reconstruction of a clavicle 3D model with a different experimental strategy. In this phase of the work, the objective was no longer to quantify deviations with respect to a single anatomical reference model, but rather to evaluate the intra-replica dimensional variability that arises when multiple identical prints are fabricated from the same digital model.

Unlike the cranial model, where segmentation was intentionally repeated multiple times to explore also operator-dependent variability, the clavicle model was designed to examine the variability that may depend on the manufacturing stage or on the measurement method used for the

dimensional comparison, independently of segmentation differences. For this reason, segmentation was performed only once on the CT dataset of an anonymous 15-year-old paediatric patient, and the resulting digital model was used to generate all subsequent replicas. Clavicle model was chosen to simulate the use of patient-specific bone replicas in surgical training for orthopaedic procedures. The compact size and linear shape of this model made it possible to optimize material use and reduce printing time.

The DICOM dataset was imported into a dedicated medical 3D imaging software, i.e., Mimics Materialise 26.0 (Leuven, Belgium) [15]. The digital segmentation was performed using a semi-automatic procedure and the segmented object was then exported to Medical 3-matic 17.0 (Leuven, Belgium) [17], where it was converted into a STL file. The mesh was optimized to minimize artifacts (i.e., stitching errors, holes, overlaps, etc.) and ensure compatibility with the print file (.3mf).

3.2.3 Airways Model

The realization of pediatric airway 3D models represents the third and most advanced phase of the segmentation and digital modelling activities carried out during this doctoral work. Unlike the cranial and clavicle models, which served primarily to investigate dimensional assessment and workflow source of errors, the tracheal case study was motivated by the need to design, fabricate, and mechanically validate anatomical replicas suitable for surgical simulation.

This activity was conducted in close collaboration with the Otorhinolaryngology Complex Operative Unit (U.O.C), as part of a structured training program on difficult airway management and the challenges associated with orotracheal intubation in pediatric patients. The clinical team expressed the need for 3D-printed laryngeal and tracheal structures capable of realistically reproducing both the anatomical geometry and the functional behavior of the upper airway, including a chamber emulating lung expansion and collapse. These models were intended to support both hands-on simulation sessions and theoretical instruction.

In this context, a primary challenge in replicating complex anatomical structures for clinical use is to represent not only the geometry but also the mechanical behavior of the real biological tissue. Among the human organs, the trachea is especially challenging to reproduce due to the combination of stiff cartilage and soft connective tissue. High-fidelity reproduction is important in a simulation environment: recent studies have highlighted the clinical relevance of 3D-printed airway models for training in tracheotomy, intubation and airway resection procedures [20], [21].

The main objective of this stage of the research was therefore of two type: (a) to reconstruct the tracheal geometry from CT datasets and generate a digital anatomical model suitable for integration into a pediatric airway simulator, described in this subchapter; (b) to design a set of complementary specimen geometries, anatomical, cylindrical and standard dog-bone shapes, that would allow the mechanical characterization of the soft photopolymers used in this application, described in the following Subchapter 3.2.4.

To meet these requirements, a real pediatric trachea was reconstructed from a CT diagnostic dataset. The DICOM images were imported into Materialise Mimics (version 26.0) and processed following the segmentation workflow previously described (Figure 3.4).

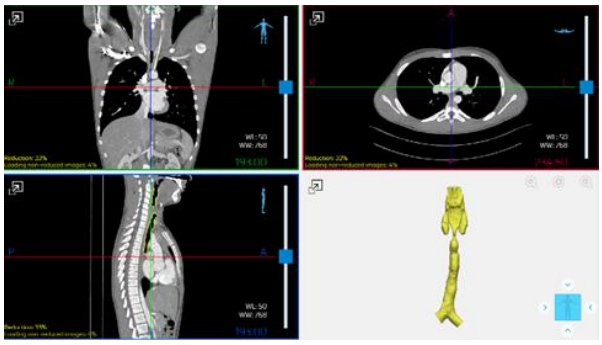

Figure 3.4. Example of a segmentation of the tracheal anatomy from high-resolution CT scans of a pediatric patient using Materialise Mimics (version 26.0).

The lower contrast associated with soft tissues required iterative refinement of the segmentation masks to maintain lumen continuity, ensure anatomically wall thickness and avoid artefacts. All masks generated throughout the iterative phases were revised and validated by the clinical team. Once validated, the segmentation mask was converted into a 3D digital model and imported into Materialise 3-matic (version 17.0) for mesh inspection, smoothing and hole closure. The goal of this digital modelling phase was to produce an airflow-tight, structurally coherent model that reproduced the tracheal geometry while ensuring compatibility with the mechanical constraints imposed by the training simulator.

To address the operational needs of the training program, the U.O.C. requested the reconstruction of multiple tracheal geometries derived from different CT examinations. This allowed the creation of different anatomically plausible airway models capturing natural inter-patient variability in pediatric tracheal morphology (Figure 3.5).

Figure 3.5. Different anatomical airway models with design adaptations to the integration on the simulator.

Before finalizing the geometry to be adopted for the training course, multiple dimensional trials were conducted. Several test versions of the trachea were fabricated with small variations in length, external diameter, connector to manikin geometry and wall thickness. These iterative tests allowed clinicians to evaluate insertion stability, compatibility with intubation and ventilation devices, and the overall ergonomics of the model during simulated procedures. Feedback from the clinical team informed the progressive refinement of the model until a final version meeting both anatomical and functional requirements was achieved.

The airway reconstruction activities performed in the PoC context provided not only the anatomical basis for the simulation environment, but also refined and perfected controlled digital framework from which it was then possible to start exploring the mechanical behavior of the printed models. Since there are no standardized geometries for testing anatomically derived soft structures, dedicated test specimen designs were developed and described in the following subchapter.

3.2.4 Anatomical, Cylindrical and Dog-Bone Specimens

The reconstruction of the pediatric airway models and their integration into the simulation environment, described in Subchapter 3.2.3, highlighted the need for a controlled and reproducible approach to investigate the mechanical behavior of the material used. There are no standardized shapes for testing anatomically derived soft structures such as the pediatric trachea; therefore, it was necessary to define dedicated geometries for the specimens.

In detail, three geometries were obtained as follows:

- Anatomical Specimens: these models replicate the true geometry of the pediatric trachea based on the CT-derived 3D reconstruction. To enable mechanical testing, external cylindrical connectors were added at both ends of the model to ensure stable clamping within the Dynamic Mechanical Analysis (DMA) system used for testing (Figure 3.5a). These connectors have a nominal internal diameter of 18 mm, external diameter of 20 mm and a height of 20 mm. The connection to the tracheal structure was obtained via a loft operation and an external hollowing of 2 mm thickness was applied to obtain a uniformly thin-walled structure. To achieve a symmetrical configuration and avoid asymmetric loading during dynamic testing, the distance between each cylindrical connector and the trachea was carefully designed. A symmetry axis was defined using the mesh geometry to align both connectors, thereby minimizing the risk of undesired resonances during dynamic loading. The final dimensions of the STL file used for the sample are reported in Table 3.2, with the corresponding dimension labels in Figure 3.5a. The entire design and geometric modelling process was performed using Materialise 3-matic (version 17.0) software.

- Cylindrical Specimens: a second set of specimens was designed using an idealized cylindrical geometry based on the average cross-section of the original tracheal segment, a simplified but dimensionally equivalent geometry, introduced to isolate material from geometric effects and facilitate comparison, following the approach adopted in [22] (Figure 3.5b). Seven cross-sections were extracted along the central axis of the trachea, spaced 11 mm apart, and the corresponding diameters were measured. The average radius was computed as 6.7 ± 0.1 mm, and the cylinder height was adjusted to 7.0 ± 0.1 mm to match the vertical dimension of the anatomical model (Table 3.2). The resulting cylindrical model was then hollowed externally with a 2 mm wall thickness, in a uniform thin-walled cylindrical shell.

- Standard Specimens (ISO 527-1A): the third group of samples was designed according to the ISO standard (Figure 3.5c) with a nominal length of 170 mm, width of 10 mm and thickness of 4 mm, which is commonly used for tensile testing of plastic materials. The CAD models of the samples were created using Fusion 360 [23]. This configuration enabled a standardized assessment of the material's mechanical properties, allowing for reliable benchmarking and comparison with existing literature and reference values.

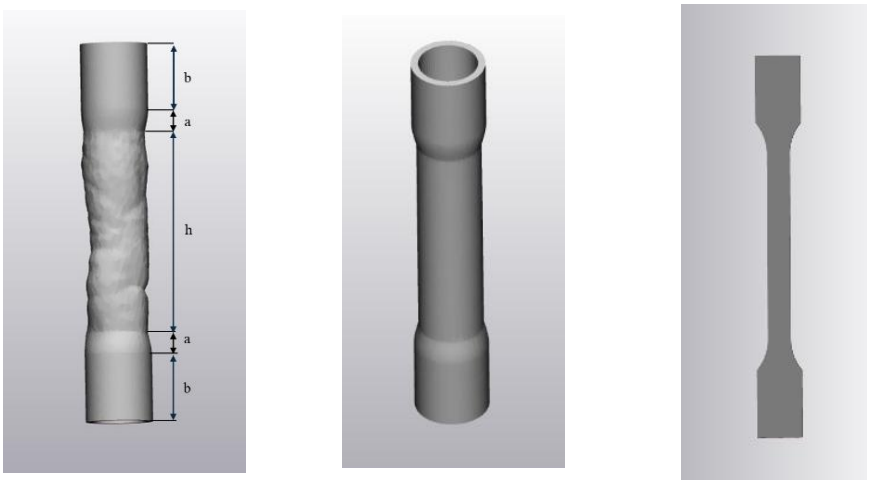

(a) (b) (c)

Figure 3.5. Specimen geometries: (a) anatomical with the labels indicating the dimensions reported in Table 3.2; (b) cylindrical and (c) dog-bone-shape of ISO 527-1A.

Table 3.2. Specimens' dimensions (expressed with a 95 % confidence level).

h (mm)	**a (mm)**	**b (mm)**	**Mean external radius (mm)**	**Mean internal radius (mm)**
60.6 ± 0.1	6.0 ± 0.1	20.0 ± 0.1	8.7 ± 0.1	6.7 ± 0.1

3.3 Printing Technologies, Materials Selection and Post-Processing Workflow

The transition from the digital model to the physical object represents a crucial phase of the PoC 3D printing workflow. In this subchapter, only the steps of slicing and 3D printing (Step 4) and post-processing (Step 5) of the workflow introduced in Chapter 2 are addressed in detail (Figure 3.6), as they constitute the operations directly involved in converting the digitally prepared anatomical structures and specimen geometries into tangible 3D models for dimensional and mechanical assessment. These two stages, illustrated in the diagram below, represent the set of technological choices and practical actions that most influence the manufacturability, reproducibility, surface and mechanical characteristics of the printed objects.

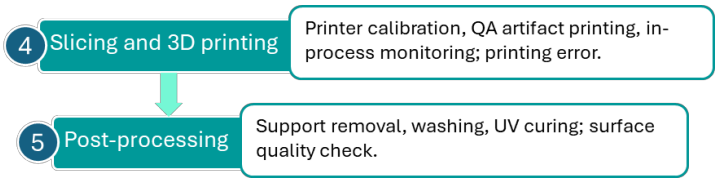

Figure 3.6. Extract of the PoC 3D printing workflow illustrating the stages addressed in this section. Step 4 (Slicing and 3D printing) includes model orientation, slicing parameter definition and machine calibration, while Step 5 (Post-processing) consists of support removal, cleaning procedures and curing operations. These phases represent the transition from the digital model to the physical object and directly influence the dimensional, mechanical and surface quality of the printed models.

Within the PoC laboratory, different additive manufacturing technologies were adopted depending on model type and intended use. Fused Deposition Modelling (FDM) [24] was employed for bone structures such as cranial and clavicle models, where rigidity, geometric stability and imaging compatibility represented the primary requirements. In contrast, Stereolithography (SLA) [25] was used for soft-tissue models such as the pediatric trachea and for all the geometries developed for mechanical testing, due to the need for thin walls, smooth surfaces and the ability to process flexible photopolymers that mimic the mechanical behavior of anatomical parts.

In addition to these in-house processes, the workflow also included models fabricated using PolyJet technology by an external manufacturer [26]. These PolyJet specimens were produced for the study of soft elastomeric materials and allowed the comparison between different technologies and printing orientations on tensile behavior. Their integration within experimental activities provides a broader perspective on how different AM processes contribute to the variability and performance of biomedical models.

Although printing parameters and printer specific settings varied across technologies, the logical structure of the slicing and printing step remained consistent. The digital model obtained from segmentation and mesh optimization was first imported into the relevant slicing software: UltiMaker Cura for FDM processes, PreForm for SLA systems and proprietary software for PolyJet fabrication. In all applications, particular importance was given to the print model orientation, support generation and layer definition as these factors influence dimensional accuracy, surface finish, and, in the case of soft materials, mechanical response under load. The slicing phase translated the digital geometry into machine-interpretable instructions.

The subsequent post-processing stage also varied according to the technology adopted but followed a consistent logic within the PoC workflow. FDM prints required the removal of support structures, dissolvable or manually detachable. SLA models underwent washing in isopropyl alcohol, support removal and UV post-curing, steps necessary to stabilize the photopolymer and ensure consistent mechanical properties. PolyJet models, processed by the external manufacturer, were delivered after standard cleaning of support gels and preliminary dimensional verification. Across all technologies, post-processing was intentionally kept as controlled and reproducible as possible, trying to reduce to minimize operator-induced artifacts.

This section provides the technological context and methodological considerations underlying the production of the anatomical models and specimen geometries described in Subchapter 3.2. The printing strategies adopted for each model type (cranial, clavicle, airway and dedicated test specimens) are discussed in the subsections that follow, linking technology and material selection, slicing choices and post-processing requirements to the specific objectives of each experimental activity.

3.3.1 3D Printing Cranial Models

The cranial models were printed using Fused Deposition Modelling (FDM) on the UltiMaker S5 Pro Bundle [27], the system available in the PoC laboratory (Figure 3.7). The skull represented the first case study where printing and slicing parameters were systematically defined to ensure reproducibility, as the aim of this study was to investigate the variability that is introduced into the models starting from the first steps of the workflow while maintaining printing conditions in the nine printed skulls.

Figure 3.7. Cranial model 3D printing with UltiMaker S5 Pro Bundle.

The STL files, derived from the segmentation workflows described in Subchapter 3.2.1, were imported into UltiMaker Cura 5.2.2 [28], where a single set of slicing parameters was established generating the G-code for printing. The reference skull model, referred to as Skull0 (Figure 3.8), was printed using the same printing parameters as the eight replicas, except for a slightly lower layer thickness to ensure optimal surface quality (Table 3.3). All 3D models were printed in polylactic acid (PLA, extruder 1 in Table 3.3), a material widely used with FDM technology [29], which exhibits excellent CT compatibility, mimicking the response of the bone to X-rays without luminescence artifacts. Furthermore, PLA is biocompatible, making it an ideal material for implantable medical devices. It is the most commonly used biodegradable polymer in clinical applications, suitable for both temporary and long-term implantable devices [30], [31], [32]. To facilitate the printing process, a water-soluble support structure made of polyvinyl alcohol (PVA, extruder 2 in Table 3.3) [33] was automatically generated for all 3D models. The printed models were placed in water for more than 48 hours to allow the PVA to dissolve. This material is particularly suitable for complex geometries like the skull, ensuring easy removal and minimal interference between contact surfaces, a critical factor for accurate dimensional measurements. The support structure was designed to maintain a 45° overhang angle, minimizing the material use and ensuring structural integrity for a total printing time of 2 days, 11 hours and 42 minutes and a post-processing of about 3 days.

Table 3.3. Main printing parameters of 3D cranial models.

Parameter	Extruder 1	Extruder 2
Material	PLA	PVA
Print temperature	205 °C	220 °C
Print speed	40 mm·s-1	35 mm·s-1
Layer height: eight replicas	0.2 mm	0.2 mm
Layer height: Skull0	0.1 mm	0.1 mm
Infill density	10 %	-

Figure 3.8. Skull0 in front and its eight replicas behind.

3.3.2 3D Printing Clavicle Models

The printing of clavicle models followed a different experimental focus from the cranial study. As described in Section 3.2.2, the objective was to investigate intra-batch manufacturing variability, that is, the variability arising exclusively from the printing process when segmentation and digital modelling are fixed.

For this study, six bone replicas were 3D printed and, to ensure strict control over the printing workflow, the same optimized STL file and the same G-code were used for all six clavicle prints. The use of a single G-code file to print all 3D replicas ensured identical orientation and position on the print bed, slicing parameters and support distribution, thereby eliminating operator-dependent variability. The G-code of the .3mf file, generated using UltiMaker Cura 5.2.2 [28], was read by the same UltiMaker S5 Pro Bundle Printer used for printing cranial mode [27]. Due to its

extensive use in FDM technology and excellent compatibility with CT imaging, PLA was also used as the printing material of the clavicle models.

The printing parameters, listed in Table 3.4, were selected based on the *Fast* profile in Ultimaker Cura to replicate the intensive and rapid use of 3D printing in a daily practical context. For the same reason, PLA was chosen for printing supports.

Table 3.4. Main printing parameters of 3D clavicle models.

Parameters	**Extruder**
Material	PLA
Layer height	0.2 mm
Print temperature	205 °C
Print speed	70.0 mm s^{-1}
Infill density	15 %

Figure 3.9 shows one of the six 3D printed models on the print bed with its supports. The relatively simple geometry of the clavicle made it quite easy to remove the rigid supports manually. As in the cranial study, no post-processing of the surface was performed to prevent any interference with the quality of the replicas in terms of surface roughness and layer resolution of the FDM printer.

Figure 3.9. An example of 3D clavicle model made of PLA on the print bed with its supports. The models exhibit the characteristic surface texture and layer pattern typical of extrusion-based manufactured.

Once all bone replicas were printed (Figure 3.10a), they were colored red to facilitate acquisitions using the 3D scanner (Figure 3.10b), a solution often adopted for reverse engineering applications [34]. This additional step was introduced to ensure optimal reflectivity and contrast for future dimensional investigations, facilitating accurate point-cloud acquisition and surface reconstruction by the structured-light 3D scanner.

(a) (b)

Figure 3.10. Six clavicle replicas (a) immediately after FDM printing, in their native white PLA, (b) displayed after applying a uniform red coating. The coloring process does not alter the geometry of the models but increases their reflectivity and visual uniformity.

3.3.3 3D Printing Airways Model

The fabrication of pediatric airway models required an AM technology capable of reproducing thin-walled structures, smooth internal surfaces and compliant mechanical behavior suitable for clinical simulation. For these reasons, the models were produced using Stereolithography (SLA) on the Formlabs Form 3BL system [35], which is widely adopted for the fabrication of anatomical models due to its high geometric accuracy and the availability of soft photopolymers.

The selection of the printing material was the result of an iterative process combining clinical feedback and mechanical performance requirements. Two SLA compatible elastomeric resins were initially considered: Elastic 50A Resin and Flexible 80A Resin, both characterized by Shore hardness values within the range typically associated with soft biological tissues. Their elastomeric behavior made them suitable candidates for simulating tracheal deformability and for enabling realistic interaction with surgical instruments.

To assess their suitability for clinical simulation, preliminary tracheal prototypes were printed using both materials and evaluated by a group of specialists from the Otorhinolaryngology U.O.C during

simulated pediatric airway procedures. The qualitative evaluation focused on the tactile response, manual deformability and the realism of contact with laryngoscopes and intubation tools. Based on this comparative assessment, clinicians unanimously identified Flexible 80A Resin as the most appropriate material.

The digital models developed in the previous stages (Subchapter 3.2.3) were imported into PreForm, where printing orientation and support placement were optimized to minimize internal supports within the airway lumen. After slicing, the models were printed using a 0.1 mm layer thickness.

Once printing was completed, the post-processing recommended by the resin supplier was performed, including washing in isopropyl alcohol in two steps of 10 minutes, support manually removal and final UV curing for 10 minutes at 60 °C. The consistency of these steps ensured uniform material behavior across the different anatomical variants printed for the training program.

The final airway model printed was integrated into a pediatric airway manikin (Figure 3.11).

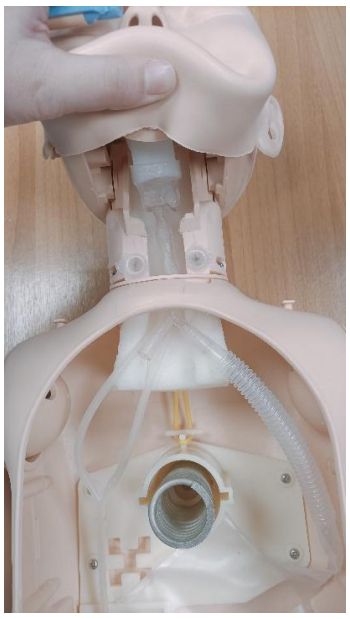

Figure 3.11. Integration of the 3D-printed tracheal model into a pediatric airway simulator.

3.3.4 3D Printing Anatomical, Cylindrical and Dog-Bone Specimens

The fabrication of the anatomical, cylindrical and dog-bone specimens followed the same stereolithography (SLA) workflow adopted for the airway models. The specimens were manufactured on a Formlabs Form 3BL printer using Flexible 80A Resin, the elastomeric material

selected following clinical evaluation, as discussed in Subchapter 3.3.3. This material was chosen for its ability to reproduce more realistically the global mechanical behavior of the pediatric trachea. In fact, among the two photopolymers evaluated, Flexible 80A Resin provided the most representative behavior of the three structural components of the tracheal wall: cartilaginous rings, connective tissue and mucosal layers, making it the most suitable choice for subsequent mechanical investigations.

Since no dedicated standard exists for defining the geometry of test specimens in this context, the three specimen geometries were designed to enable a systematic exploration of how geometry influences the mechanical response of SLA printed elastomers. Anatomical specimens (Figure 3.12) replicated the real tracheal morphology reconstructed from CT datasets (Subchapter 3.2.4), whereas cylindrical specimens (Figure 3.13) were derived from the average cross-sectional geometry of the trachea to create an idealized and more homogeneous thin-walled structure. Finally, the ISO 527-1A dog-bone shape (Figure 3.14) was included to provide standardized geometry for comparison.

All models were oriented horizontally relative to the build platform to ensure uniform mechanical performance and to optimize structural homogeneity and minimize anisotropy due to layer orientation. Anatomical and cylindrical specimens were printed with a layer thickness of 0.1 mm, resulting in 267 layers and an average print time of approximately 8 hours per batch. For the ISO 527-1A specimens, the same resin, layer thickness, and print orientation were used, but only 40 layers were required, with an estimated print time of approximately 1 hour and 30 minutes. The supports, identical for all anatomical, cylindrical, and dog-bone shape specimens belonging respectively to the same print batch, were carefully removed manually by the same operator, following the standard procedures recommended for this material and technology. This ensured consistency in the post-processing phase and minimized variability due to support handling.

After printing, samples were subjected to a post-processing protocol recommended by the manufacturer of the printer and the material, including: washing in 98% isopropyl alcohol for 10 minutes, post-curing in the Form Cure unit at 60 °C for 10 minutes..

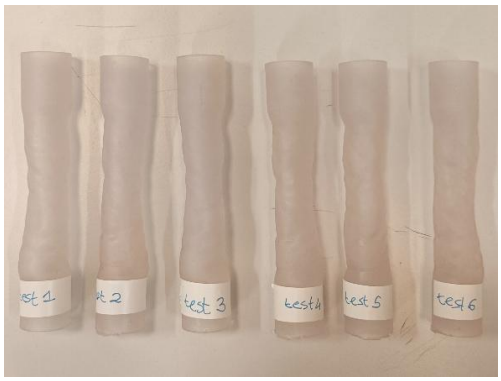

Figure 3.12. Anatomical specimen 3D printed using SLA, derived from the CT-based reconstruction of the pediatric trachea.

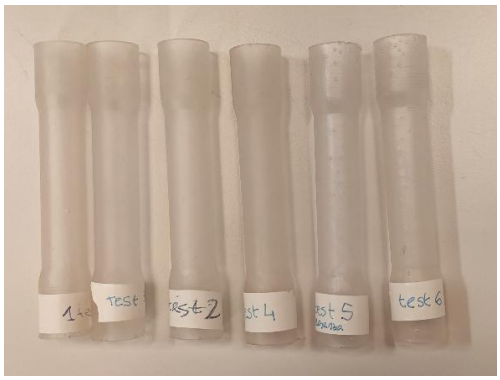

Figure 3.13. Cylindrical specimen 3D printed using SLA, obtained from the average cross-sectional dimensions of the trachea.

Figure 3.14. ISO 527-1A dog-bone specimen 3D printed using SLA, included as a standardized reference geometry for comparative mechanical assessment.

In addition to the SLA printed specimens, ISO 527-1A dog-bone specimens fabricated using PolyJet technology were also included in the experimental activities. These were produced

externally using the Stratasys J750 Digital Anatomy system [36] and printed in Agilus30™, a rubber-like photopolymer with a Shore A hardness of 30. This material is widely adopted in biomedical 3D printing for its elastic properties and its ability to reproduce soft anatomical structures. The PolyJet specimens were fabricated specifically to investigate the effect of printing orientation on the tensile behavior of soft photopolymers, as this is a key factor influencing material anisotropy in AM processes. For this purpose, specimens were printed in two orientations, vertical and horizontal (Figure 3.15). The nominal layer thickness was 0.037 millimeters, in accordance with the printing conditions recommended by the material manufacturer. A complete overview of the two printed batches, each consisting of eight specimens for a total of sixteen samples, is shown in Figure 3.16.

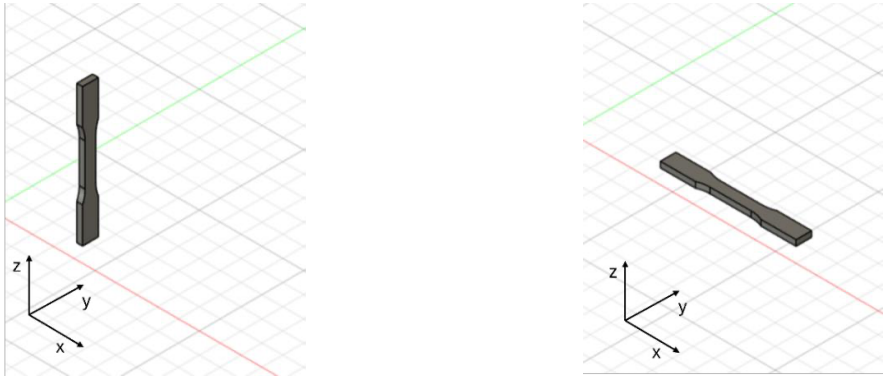

(a) (b)

Figure 3.15. A representation of the specimens placed on the printing bed in (a) vertical orientation, and (b) horizontal orientation.

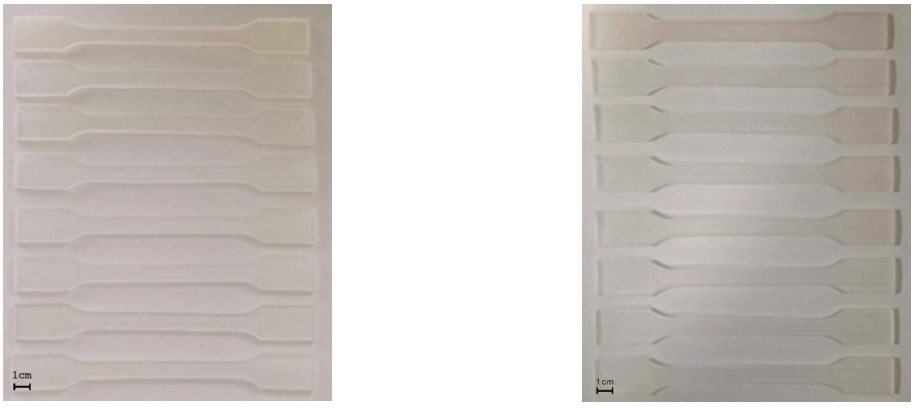

(a) (b)

Figure 3.16. Overview of the PolyJet printed dog-bone specimens: (a) first batch printed in vertical orientation and (b) second batch printed in horizontal orientation, for a total of sixteen specimens.

By combining SLA and PolyJet specimens within the same methodological framework, this doctoral work enabled a broader comparative assessment across both anatomical and standardized geometries, as well as most common AM technologies most commonly employed in biomedical applications. Particular attention is paid to metrological aspects, including measurements repeatability, reproducibility and uncertainty estimation, which are intrinsically linked to the workflow adopted. These considerations are explicitly addressed in Chapter 4 through the dimensional evaluation of printed models and further explored in Chapter 5 to study the mechanical response of 3D-printed soft materials under controlled and comparable test conditions.

References

[1] A. Tejo-Otero, I. Buj-Corral, and F. Fenollosa-Artés, "3D Printing in Medicine for Preoperative Surgical Planning: A Review," *Ann. Biomed. Eng.*, vol. 48, no. 2, pp. 536–555, Feb. 2020, doi: 10.1007/s10439-019-02411-0.

[2] Z. Sun, Y. H. Wong, and C. H. Yeong, "Patient-Specific 3D-Printed Low-Cost Models in Medical Education and Clinical Practice," *Micromachines*, vol. 14, no. 2, p. 464, Feb. 2023, doi: 10.3390/mi14020464.

[3] A. Ganapathy *et al.*, "Guide for starting or optimizing a 3D printing clinical service," *Methods*, vol. 206, pp. 41–52, Oct. 2022, doi: 10.1016/j.ymeth.2022.08.003.

[4] V. A. Sears and J. M. Morris, "Establishing a Point-of-Care Virtual Planning and 3D Printing Program," *Semin. Plast. Surg.*, vol. 36, no. 03, pp. 133–148, Aug. 2022, doi: 10.1055/s-0042-1754351.

[5] K. W. Shim, "Medical Applications of 3D Printing and Standardization Issues," *Brain Tumor Res. Treat.*, vol. 11, no. 3, p. 159, 2023, doi: 10.14791/btrt.2023.0001.

[6] M. M. Duran, G. Moro, Y. Zhang, and A. Islam, "3D printing of silicone and polyurethane elastomers for medical device application: A review," *Adv. Ind. Manuf. Eng.*, vol. 7, p. 100125, Nov. 2023, doi: 10.1016/j.aime.2023.100125.

[7] Y. Zhu *et al.*, "3D-Printed Polymeric Biomaterials for Health Applications," *Adv. Healthc. Mater.*, vol. 14, no. 1, p. 2402571, 2025.

[8] J. F. Henriques, L. Gonçalves, A. M. Amaro, and A. P. Piedade, "3D printed polymers that mimic the mechanical properties of atherosclerotic blood vessels for training models: the advantageous degradation induced by UV radiation and hydrolysis," *3D Print. Med.*, vol. 11, no. 1, p. 34, July 2025, doi: 10.1186/s41205-025-00288-5.

[9] S.-J. Estermann, D. H. Pahr, and A. Reisinger, "Quantifying tactile properties of liver tissue, silicone elastomers, and a 3D printed polymer for manufacturing realistic organ models," *J. Mech. Behav. Biomed. Mater.*, vol. 104, p. 103630, Apr. 2020, doi: 10.1016/j.jmbbm.2020.103630.

[10] N. V. Ngoc *et al.*, "A review of the mechanical of SLA 3D printing materials: Printing Orientations and Photopolymerization Technology," presented at the International Conference on

Advanced Mechanical Engineering, Automation and Sustainable Development, Springer, 2021, pp. 660–664.

[11] K. M. S. A. Mahrooqi, C. K. C. Ng, and Z. Sun, "Pediatric Computed Tomography Dose Optimization Strategies: A Literature Review," *J. Med. Imaging Radiat. Sci.*, vol. 46, no. 2, pp. 241–249, 2015, doi: https://doi.org/10.1016/j.jmir.2015.03.003.

[12] C. Hopfner *et al.*, "Design and 3D printing of variant pediatric heart models for training based on a single patient scan," *3D Print. Med.*, vol. 7, no. 1, p. 25, Aug. 2021, doi: 10.1186/s41205-021-00116-6.

[13] S. Ghai, Y. Sharma, N. Jain, M. Satpathy, and A. K. Pillai, "Use of 3-D printing technologies in craniomaxillofacial surgery: a review," *Oral Maxillofac. Surg.*, vol. 22, no. 3, pp. 249–259, Sept. 2018, doi: 10.1007/s10006-018-0704-z.

[14] "Dual Source CT." Accessed: Dec. 04, 2025. [Online]. Available: https://www.siemens-healthineers.com/it/computed-tomography/technologies-and-innovations/dual-source-ct

[15] "Materialise Mimics | Healthcare Software Platform." [Online]. Available: https://www.materialise.com/en/healthcare/mimics

[16] "Meshmixer | Fusion | Autodesk App Store." Accessed: Dec. 04, 2025. [Online]. Available: https://apps.autodesk.com/FUSION/en/Detail/Index?id=4108920185261935100&appLang=en&os=Win64

[17] "Materialise 3-matic Medical | Medical Device Design Software." Accessed: Aug. 13, 2025. [Online]. Available: https://www.materialise.com/en/healthcare/mimics/3-matic-medical

[18] N. Kamaruddin, Z. A. Rajion, A. Yusof, and M. E. Aziz, "Relationship between Hounsfield unit in CT scan and gray scale in CBCT," presented at the TRANSLATIONAL CRANIOFACIAL CONFERENCE 2016 (TCC 2016): Proceedings of the 1st Translational Craniofacial Conference 2016, Pinang, Malaysia, 2016, p. 020005. doi: 10.1063/1.4968860.

[19] T. Razi, P. Emamverdizadeh, N. Nilavar, and S. Razi, "Comparison of the Hounsfield Unit in CT scan with the Gray Level in cone-beam CT," *J. Dent. Res. Dent. Clin. Dent. Prospects*, vol. 13, no. 3, pp. 177–182, Dec. 2019, doi: 10.15171/joddd.2019.028.

[20] N. Shimojima *et al.*, "Simulated slide tracheoplasty for congenital tracheal stenosis using three-dimensional printed models," *Pediatr. Surg. Int.*, vol. 38, no. 12, pp. 1895–1902, 2022.

[21] A. Ramella *et al.*, "Validation and Verification of High-Fidelity Simulations of Thoracic Stent-Graft Implantation," *Ann. Biomed. Eng.*, vol. 50, no. 12, pp. 1941–1953, Dec. 2022, doi: 10.1007/s10439-022-03014-y.

[22] Q. Chai, S. Huang, F. Wan, F. Wu, and L. Feng, "A new experimental method to measure and calculate the tensile strength of concrete," *Front. Mater.*, vol. 10, p. 1216747, July 2023, doi: 10.3389/fmats.2023.1216747.

[23] "Autodesk Fusion | 3D CAD, CAM, CAE, & PCB Cloud-Based Software | Autodesk." Accessed: Apr. 09, 2025. [Online]. Available: https://www.autodesk.com/it/products/fusion-360/overview

[24] R. H. Risad, Md. H. Ahmed, A. Basher, S. Rashid, Md. M. A. Shishir, and K. R. Hossain, "FDM printing process and its Biomedical Application," *Chem. Res. Technol.*, vol. 1, no. 3, July 2024, doi: 10.22034/chemrestec.2024.467346.1021.

[25] P. Lakkala, S. R. Munnangi, S. Bandari, and M. Repka, "Additive manufacturing technologies with emphasis on stereolithography 3D printing in pharmaceutical and medical applications: A review," *Int. J. Pharm. X*, vol. 5, p. 100159, Dec. 2023, doi: 10.1016/j.ijpx.2023.100159.

[26] N. Muthuram, P. Sriram Madhav, D. Keerthi Vasan, M. E. Mohan, and G. Prajeeth, "A review of recent literatures in poly jet printing process," *Mater. Today Proc.*, vol. 68, pp. 1906–1920, 2022, doi: 10.1016/j.matpr.2022.08.090.

[27] "UltiMaker S5," UltiMaker. Accessed: Dec. 05, 2025. [Online]. Available: https://ultimaker.com/3d-printers/s-series/ultimaker-s5/

[28] "UltiMaker Cura," UltiMaker. Accessed: Dec. 05, 2025. [Online]. Available: https://ultimaker.com/software/ultimaker-cura/

[29] E. H. Tümer and H. Y. Erbil, "Extrusion-Based 3D Printing Applications of PLA Composites: A Review," *Coatings*, vol. 11, no. 4, p. 390, Mar. 2021, doi: 10.3390/coatings11040390.

[30] M. Hussain, S. M. Khan, M. Shafiq, and N. Abbas, "A review on PLA-based biodegradable materials for biomedical applications," *Giant*, vol. 18, p. 100261, June 2024, doi: 10.1016/j.giant.2024.100261.

[31] S. Pérez-Davila *et al.*, "3D-Printed PLA Medical Devices: Physicochemical Changes and Biological Response after Sterilisation Treatments," *Polymers*, vol. 14, no. 19, p. 4117, Oct. 2022, doi: 10.3390/polym14194117.

[32] A. J. R. Barcena, P. Ravi, S. Kundu, and K. Tappa, "Emerging Biomedical and Clinical Applications of 3D-Printed Poly(Lactic Acid)-Based Devices and Delivery Systems," *Bioengineering*, vol. 11, no. 7, p. 705, July 2024, doi: 10.3390/bioengineering11070705.

[33] N. Y. Z. Ng, R. H. Abdul Haq, O. M. F. Marwah, F. H. Ho, and S. Adzila, "Optimization of polyvinyl alcohol (PVA) support parameters for fused deposition modelling (FDM) by using design of experiments (DOE)," *Mater. Today Proc.*, vol. 57, pp. 1226–1234, 2022, doi: 10.1016/j.matpr.2021.11.046.

[34] R. H. Helle and H. G. Lemu, "A case study on use of 3D scanning for reverse engineering and quality control," *Mater. Today Proc.*, vol. 45, pp. 5255–5262, 2021, doi: 10.1016/j.matpr.2021.01.828.

[35] "Form 3BL: una stampante 3D di grande formato sviluppata per il settore sanitario.," Formlabs. Accessed: Dec. 05, 2025. [Online]. Available: https://formlabs.com/it/3d-printers/form-3bl/

[36] "J750 Digital Anatomy 3D Printer | Stratasys Support Center," Stratasys. Accessed: Dec. 05, 2025. [Online]. Available: https://support.stratasys.com/en/Printers/PolyJet-Legacy/J750-Digital-Anatomy

Chapter 4

Dimensional Assessment

4.1 Role of Dimensional Assessment in the PoC workflow

The dimensional assessment of 3D-printed anatomical models represents a key verification step within Point-of-Care (PoC) additive manufacturing (AM) workflows. As described in the workflow introduced in Chapter 2, each phase including image acquisition, segmentation, digital modelling, fabrication, post-processing and eventually sterilization may introduce potential sources of error that accumulate along the production chain. The *Inspection* step represents the final verification stage in which printed models are evaluated to ensure that they meet the geometric and functional fidelity defined during the digital preparation step.

As illustrated in Step 7 of the workflow (Figure 4.1), this stage includes both dimensional accuracy assessment, performed through CT, micro-CT, 3D scanning or other metrological techniques, and mechanical assessment, which evaluates strength, stiffness, elasticity and durability.

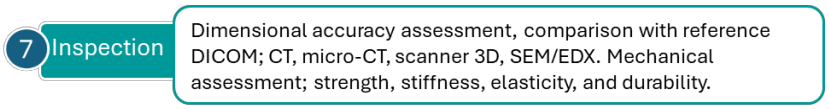

Figure 4.1. Step 7 of the PoC 3D-printing workflow: inspection. This phase includes the dimensional accuracy assessment of the printed model through comparison with reference geometry as well as the mechanical assessment of the material response. Together, these operations provide quantitative verification of the geometric and functional fidelity of the final object before clinical use or further evaluation within the PoC environment.

The dimensional congruence of 3D printing models to the patient's actual anatomy is critical for safe and effective clinical decision-making [1], [2]. This is a highly relevant issue, and research is actively investigating this field [3], [4]. Hence, the need for a specific QC protocol including dimensional assessment [5]. In [6], thirty-five 3D printed models were subjected to high-resolution CT scans to estimate their accuracy. The wall thickness and surface congruency were compared with the original STL file using dedicated 3D engineering software. In [7], the clinical reliability of point-of-care 3D printed cranial implants was evaluated by analyzing their geometric,

morphological, and biomechanical properties. The inspection step is the only stage in which objective and measurable indicators of print quality are evaluated and where dimensional and mechanical properties are quantitatively assessed against the digital reference model.

Despite its centrale role, current practices in PoC 3D printing remain highly fragmented. The literature reports significant variability in verification strategies, measurement instrumentation, dimensional metrics and acceptance threshold. A consolidated or internationally adopted protocol for PoC quality control is not yet available and the methodologies implemented in hospitals or research laboratories often depend on local expertise, available equipment and clinical needs. This variability is exacerbated by the lack of regulatory standards specifically tailored to in-house 3D printing, resulting in heterogeneous quality control procedures and limited reproducibility between institutions.

To address this gap, several research groups have proposed different dimensional assessment QC frameworks, reflecting in the heterogeneous approaches. These contributions collectively highlight the need for multilayered inspection strategies, explicit error classification and the integration of both preventive and corrective actions.

The next Subchapter 4.2 introduces the dimensional inspection methods most frequently employed in PoC biomedical 3D printing, synthesizing the approaches described across recent studies and grouping them into two main categories: (a) direct linear metrology, (b) surface and volumetric evaluation. These methods constitute the conceptual basis for the quantitative dimensional assessments developed and applied in this doctoral program.

4.2 Dimensional Assessment Methods Form Literature

Dimensional assessment in PoC 3D printing relies on a variety of measurement strategies that differ in methods, resolution and operating principles. The literature reports a broad spectrum of dimensional assessment approaches, reflecting the diversity of measurement instruments, measurement chains and image-analysis techniques used in PoC environments. Methods range from caliper measurements and manual measuring tools to optical scanning or Computed Tomography (CT) images comparisons, voxel analyses and CAD overlays between the 3D model before and after printing [8]. This methodological heterogeneity reflects both the rapid technological expansion of biomedical AM and the absence of standardized protocols for in-house manufacturing.

Several gaps limit comparability across sites. First, metric heterogeneity is evident: accuracy is reported using a variety of measures, including landmark deviations, mean or percentile surface errors and root mean square error (RMSE) [1]. Many studies do not define clinically justified acceptance bands, making it difficult to translate geometric deviations into release decisions with clear clinical implications. Second, the estimation of error sources is often incomplete: segmentation uncertainty, digital editing contributions, manufacturing deviations and post-processing effects are frequently aggregated into a single dimensional error without disentangling their partial contributions [9], limiting the ability to target corrective actions. Third, sampling plans and acceptance criteria are highly variable, with model-specific, technology dependent or institution specific choices regarding sample size, sampling frequency and tolerance thresholds. Finally, uncertainty reporting remains inconsistent: uncertainty bands vary significantly between laboratories, often depending on operator expertise or local measurement practices, making comparisons between studies and measurement reproducibility difficult and reducing the interpretability of reported measurements.

Despite this variability, most approaches described in the literature can be grouped into two main methodological categories: (a) direct linear metrology and (b) surface and volumetric evaluation. These categories represent the basis of dimensional assessment workflows adopted in PoC laboratories and inform the methodological framework applied in this doctoral work.

The following sections provide an overview of these two families of methods, describing their instruments, operating principles and typical use cases as reported in PoC 3D-printing studies.

4.2.1 Direct Linear Metrology

In PoC laboratories, the simplest and most accessible method for verifying dimensional accuracy is direct metrology, which consists of comparing linear distances between predefined anatomical landmarks on the printed part and their corresponding digital values from the reference STL or DICOM dataset. This technique typically relies on digital calipers, vernier calipers or micrometers, chosen for their ease of use and high repeatability under controlled conditions. According to recent studies, digital calipers with nominal accuracies of ± 0.01 mm or ± 0.02 mm and micrometers with resolutions down to 0.001 mm were consistently employed. A summary of the measurement instruments, nominal resolutions and acceptance thresholds reported in recent PoC studies is presented in Table 4.1.

Regarding the instrumentation, for example, Ravi et al. alternated between micrometers and calipers depending on the geometry [10], while Fayed documented a micrometer with 0.001 mm precision and a vernier caliper accurate to 0.01 mm, representative of instruments available and suitable for PoC verification [11]. Arnold et al. measured printed dental models using a certified digital caliper with a manufacturer-specified accuracy of ± 0.02 mm, performing five repeated measurements for each dimension under controlled laboratory conditions [12].

Similarly, Mohamed et al. used a digital caliper with ± 0.01 mm accuracy to assess the length, width, and thickness of printed denture specimens, taking three readings per point to minimize operator variability [13]. Regarding accuracy results, Ravi et al. measured multi-pathological anatomical models and found maximum dimensional errors below 1 mm and mean deviations under 0.26 mm, concluding that a 1 mm global tolerance can serve as a clinically acceptable cutoff for most applications [10].

Further confirmation of these limits was provided by Lee et al., who constructed personalized 3D printed femoral pseudoaneurysm models for endovascular training and assessed linear dimensions against DICOM data using a digital caliper (0.01 mm resolution). They reported mean deviations of 0.21 ± 0.13 mm and a maximum absolute error below 0.5 mm, supporting the 1 mm tolerance as a safe acceptance criterion for vascular simulation [14]. For higher-precision requirements, such as dental master or surgical planning models, Arnold et al. suggested that the gypsum references may achieve < ± 50 μm [12].

Finally, Wendo et al. conducted a study on the evaluation of dimensional accuracy for FDM-printed anatomical models of the hand, quantifying parameters such as Mean Absolute Difference (MAD) and Mean Dimensional Error (MDE), which were also within the commonly accepted thresholds of ≤ 1 mm or ≤ 2 % for patient-specific clinical models [15].

Table 4.1. Summary of direct linear metrology approaches reported in recent PoC studies.

Study and year	Measurement Instrument	Nominal Resolution	QC Acceptance Threshold	Ref.
Ravi et al., 2022	Micrometer and caliper	0.001 mm	≤ 1 mm; ≤ 3%	[10]
Fayed 2024	Micrometer and vernier caliper	0.001mm; 0.01 mm	± 1 mm	[11]
Arnold et al., 2024	Digital caliper	0.02 mm	± 0.05 mm	[12]
Mohamed et al., 2025	Digital caliper	0.01 mm	± 0.5 mm	[13]
Lee et al., 2024	Digital caliper	0.01 mm	≤ 1 mm	[14]
Wendo et al., 2025	Digital caliper	0.02 mm	≤ 1 mm; ≤ 2 %	[15]

Although widely adopted for its simplicity and accessibility, direct linear metrology in this context shows substantial variability in the choice of instruments, nominal resolutions and tolerance thresholds across studies. Consequently, the quantitative outcomes reported, ranging from sub-millimetric accuracy to percentage-based deviations, are difficult to compare, and the lack of dedicated standardized measurement protocols limits the reproducibility of landmark-based assessments in PoC environments. This heterogeneity underscores the need for harmonized procedures.

4.2.2 Surface and Volumetric Metrology

For a more comprehensive assessment of external and internal geometry, recent studies have increasingly adopted optical 3D scanning, CT, micro-CT, and Scanning Electron Microscopy-Energy Dispersive X-ray (SEM/EDX) to validate printed anatomical models and implantable structures. These methods rely on a 3D-to-3D comparison between the printed part and its source digital file: the printed model is rescanned, registered to the reference STL, and deviations are computed across the whole surface or volume. A summary of the surface- and volume-based metrology instruments, nominal resolutions and acceptance thresholds reported in recent studies is presented in Table 4.2.

The surface of the printed part is captured as a dense point cloud or mesh, which is then digitally aligned with the reference STL file by landmark-based or best-fit registration. The deviation between the two surfaces can be visualized as a color-coded map showing local accuracy variations

and is accompanied by quantitative metrics such as root-mean-square (RMS) error and the percentage of surface area within tolerance. Typically, green regions indicate minimal deviation, while red and blue denote positive and negative deviations, respectively. Structured-light and laser scanning remain the most widely adopted surface-based QC tools.

Similarly, Msallem et al. digitized reference and printed mandibular models using the same EinScan-SP structured-light scanner, with 0.05 mm single-shot accuracy and 0.17-0.20 mm point spacing, aligning meshes in Materialise 3-matic. RMS deviations across FDM, SLA, SLS and MJ models remained < 0.2 mm, with SLS achieving 110 ± 16 μm trueness [16]. Recent implementations couple micro-CT with SEM/EDX for correlated morphological and compositional validation. Gendviliene et al. combined micro-CT (Bruker Skyscan 1178, 80 μm pixels, 65 kV, 615 μA) and SEM (Hitachi TM-1000) to assess layer height, thread spacing, and morphology, using Geomagic Control X for superimposition and ± 0.025 mm best-fit alignment. This protocol exemplifies hybrid inspection applicable to medical models [17].

When full-volume fidelity is required, CT-based metrology enables simultaneous assessment of external and internal features. Lebowitz et al. reconstructed CT-scanned carpal bones printed from cadaveric data, finding a mean absolute error of 0.22 ± 0.07 mm between print and native geometry [18]. Hsu et al. also demonstrated ABS canine tibia FDM models with RMS deviation 0.30 mm, measured against original CT by voxel-wise overlay [19]. Complementarily, Tóth et al. compared four commercial scanners (Artec Eva, 3Shape D700, Steinbichler Comet L3D, Creaform EXAscan) on an FDM printed vertebra model, reporting nominal accuracies of 0.010-0.012 mm (3Shape), 0.025 mm sphere-spacing error (Steinbichler), and ± 0.055 mm in x,y,z axis resolution (EXAscan). The deviation of their anatomical model varies from 0.272 mm to 0.361 mm depending on the scanner used, which represents a difference of 1.088 - 1.440% [20]. Kaschwich et al. used CT with 0.33 mm isotropic resolution (Siemens Somatom Definition) to validate patient-specific aortic phantoms printed by PolyJet technology. Mean surface deviation stayed below 0.3 mm and the correlation between printed and CT-derived vessel diameters exceeded, proving the sensitivity of CT to lumen geometry inaccessible to optical scanning [21].

Across optical-scan studies, the EinScan-SP, 3Shape D700 and Steinbichler L3D emerge as reference instruments for PoC dimensional verification, typically offering nominal precision ≤ 50 μm, with practical RMS deviations below 0.2 mm over entire anatomical geometries. Overall, across literature, structured-light 3D scanners achieve ≤ 50 μm nominal accuracy, clinical CT/CBCT deliver sub-millimetric (0.3-0.5 mm) fidelity, and CT attains 0.33 pixel resolution.. Deviation analyses consistently report RMS or mean absolute differences < 0.3 mm and propose tolerance

bands of ± 0.25-0.5 mm for anatomical verification and ≤ 2% volumetric discrepancy as a practical QC threshold for PoC facilities.

Table 4.2. Summary of surface and volumetric metrology approaches reported in recent PoC studies.

Study and year	Measurement Instrument	Nominal Resolution	QC Acceptance Threshold	Ref.
Msallem et al., 2020	EinScan-SP (SHINING 3D)	0.05 mm	± 0.25 mm	[16]
Gendviliene et al., 2020	Bruker Skyscan 1178; Hitachi TM-1000 SEM	Pixel 0.8 mm	± 0.25 mm	[17]
Lebowitz et al., 2020	Siemens Somatom Emotion	Pixel 0.3 mm	± 0.5 mm	[18]
Hsu et al., 2020	Toshiba Aquilion One	Pixel 0.3 mm	± 0.5 mm	[19]
Tóth et al., 2021	Artec Eva; 3Shape D700; Steinbichler Comet L3D; Creaform EXAscan	10 - 55 μm	≤ 2 % (1)	[20]
Kaschwich et al., 2021	CT Siemens Somatom Definition	Pixel 0.33 mm	± 0.3 mm	[21]

Similarly, surface and volumetric metrology exhibit considerable methodological diversity, with studies relying on different acquisition systems, measuring instruments and methods, accuracy and acceptance threshold. From a metrological standpoint, the reported results reflect both the fragmentation of the sector and a limited attention to uncertainty and measurement consistency. While these techniques provide richer spatial information than linear measurements, the heterogeneity in scanner performance, voxel resolutions and deviation analyses complicates cross-study comparisons and the interpretation of reported dimensional fidelity. Once again, this fragmentation highlights the absence of unified guidelines for geometric validation and confirms the importance of developing standardized QC protocols for PoC 3D printing.

4.3 Proposed Dimensional Assessment

The dimensional assessment framework developed in this doctoral work was designed to address specific limitations identified in the literature and to propose a methodology suitable for evaluating geometric fidelity in PoC additive manufacturing. Building on the heterogeneous landscape of measurement approaches described in Subchapter 4.2, this work adopts a structured two-stage strategy combining slice-based 2D analysis and volumetric 3D evaluation.

The first specific goal was to investigate how image-based measurement variability, particularly segmentation choices, slice selection and operator-dependent procedures, influence the dimensional outcome of printed anatomical models. To address this, a CT slice-based linear measurement method was implemented, enabling the extraction of clinically relevant geometric indicators (e.g., diameters, thicknesses and cross-sectional areas) directly from diagnostic imaging. The comparison between a reference cranial model and multiple FDM printed replicas allowed the investigation of segmentation variability, modelling effects and manufacturing contributions, forming the basis for the two-dimensional studies presented in Subchapter 4.3.1.

A second specific goal was to evaluate the impact of operator-dependent positioning during CT acquisition of the model to be inspected, a variable frequently overlooked in adopting CT image analysis in PoC quality control. For this reason, part of the proposed methodology includes the repeated CT scanning of the same reference model by the same operator, allowing an estimation of intra-operator variability and its contribution to the overall dimensional uncertainty.

The third specific goal was to extend dimensional verification from isolated cross-sections to the entire 3D geometry of printed models. To this end, the methodology integrates a volumetric assessment based on the comparison of CT acquisitions of multiple FDM printed clavicle replicas, together with an evaluation of the two measurement systems employed: a diagnostic CT scanner commonly available in hospital settings and a high-resolution industrial metrological CT used as reference. By segmenting the printed models and comparing either voxel masks or tetrahedralized STL geometries, the approach enables the quantification of production repeatability and the assessment of volumetric consistency across prints manufactured under nominally identical conditions. This forms the basis of the three-dimensional analyses presented in Subchapter 4.3.2.

The proposed approach leverages instruments and procedures realistically accessible in hospital settings, such as diagnostic CT, while incorporating high-accuracy industrial measurements for reference validation. The dual 2D and 3D strategy enables the characterization of both local

deviations, affected by segmentation, slice choice and imaging protocol, and global volumetric discrepancies, affected by manufacturing repeatability and CT resolution. The following sections detail the implementation of these methodologies through the experimental cases studies developed in this doctoral work.

4.3.1 Two-Dimensional Assessment of Cranial Model

The first application of the proposed dimensional assessment framework focuses on the two-dimensional evaluation of a cranial anatomical model. The skull was selected as a benchmark geometry because it exhibits thin cortical regions, concave and convex surfaces, and internal cavities, all of which are sensitive to segmentation parameters, image-processing choices and printing parameters. Moreover, cranial models are widely used in surgical planning, training and research, making them a representative test case for PoC dimensional verification.

Within this case study, the dimensional assessment was structured as an incremental sequence of investigations, each adding a new layer of methodological refinement. A CT slice-based measurement protocol was first defined and applied to a set of FDM printed skull replicas. The aim was to establish a reproducible procedure for extracting diameters, thicknesses and cross-sectional areas in a transverse anatomical plane. This preliminary framework was then extended by translating the methodology to a second anatomical plane and to repeated CT acquisitions in order to investigate the effect of operator-dependent positioning.

The following subchapters describe the measurement procedures adopted for this two-dimensional assessment. Subchapter 4.3.1.1 introduces the CT slice-based measurement protocol common to all investigations. Subchapter 4.3.1.2 and Subchapter 4.3.1.3 present the transverse and coronal plane assessments, respectively, while Subchapter 4.3.1.4 focuses on image analysis, threshold selection and the associated uncertainty contributions.

4.3.1.1 CT Slice-Based Linear Measurements

The CT slice-based linear measurement protocol was designed to obtain a set of geometric quantities from diagnostic CT data and to apply the same measurements to both the reference cranial model and its FDM printed replicas.
The segmentation and FDM fabrication of the reference skull model and its eight replicas have been previously described in Subchapter 3.2.1 and Subchapter 3.3.1, where the same segmentation workflow, mesh optimization and printing parameters were used to obtain each replica comparable

with the skull reference. A first scan of the reference skull model allowed 3D reconstruction and printing of the eight replicas. A second scan of all nine skull models allowed dimensional assessment based on image analysis. This approach involved capturing high-resolution images of both the reference model and replicas, ensuring that the details and features were captured. The nine 3D cranial models, i.e., the reference skull model and its replicas, were subjected to the same CT scanning protocol to allow direct comparison of their dimensional measurements.

For the transverse-plane analysis, all skulls were scanned using a Siemens Somatom Force® dual-source CT scanner [22], following a pediatric head protocol optimized for high in-plane spatial resolution. The acquisition parameters are summarized in Table 4.3. For the coronal-plane analysis, skulls were scanned using a Siemens Somatom Force® single-source CT scanner [23], adopting a modified protocol that increased the number of acquired slices in order to improve the continuity of the reconstruction. This second protocol, reported in Table 4.4, provided a denser sampling and enabled a more detailed evaluation of how image orientation, skull positioning, and operator-dependent variability affect CT dimensional measurements.

Table 4.3. Main Settings of CT Scan Protocol used for transverse-plane analysis

CT parameter	**Setting**
Total number of slices	263
Slice thickness	0.5 mm
Slice increment	0.5 mm
Pixel size	0.35 × 0.35 mm^2
Field of view	180 mm
Voltage peak	90 kV
Single collimation width	0.59 mm
Step factor	0.55

Table 4.4. Main Settings of CT Scan Protocol used for coronal-plane analysis

CT parameter	**Setting**
Pixel size	0.34 × 0.34 mm^2
Field of view	175.00 mm
Number of slices	415
Slice increment	0.4 mm

Slice thickness	0.4 mm
Voltage peak	120 kV
Single collimation width	0.29 mm

A rigorous and objective method based on image analysis was applied to assess the dimensional congruence between the reference skull model and its replicas. This method involves automatic segmentation of CT scans to identify the slice with the largest outer diameter for each skull, enabling 2D analysis in both planes. The segmentation of CT images, based on a threshold value derived from the grayscale values of the data acquired, allows determining 3D masks for all skulls. The slice corresponding to the mask with the largest outer diameter is identified for replicas and skull reference and used for the dimensional comparison based on the following quantitative parameters: section area, maximum longitudinal diameter and cortical thicknesses identified at the latter. These measurements are compared for each replica and the reference skull model, resulting in the quantitative values and the percentage difference of the above quantities. Specifically, the section area is determined by counting the white pixels in the selected mask and then converting the pixel count to mm^2 based on pixel size.

4.3.1.2 Transverse Plane Dimensional Assessment

The transverse plane assessment represents the first implementation of the CT slice-based protocol on a set of FDM-printed cranial models. In medical anatomy, a transverse plane, also referred to as axial or horizontal plane, is an anatomical plane that is perpendicular to both the sagittal and coronal planes and divides the body or any of its parts horizontally into superior (upper) and inferior (lower) portions[24]. The main objective of this investigation was to quantify dimensional deviations between the reference skull and multiple printed replicas in a single plane to explore the contributions of segmentation and printing variability.

As described in Subchapter 4.3.1.1, all skulls were scanned using the same dual-source clinical CT protocol, ensuring that the DICOM datasets were directly comparable. To maintain consistency in positioning, all skulls were scanned following the pediatric head CT protocol. They were carefully placed in a dedicated stand (Figure 4.2) and centered within the gantry using a cruciform laser system (Figure 4.3). To ensure repeatability, a single experienced radiology technician was responsible for positioning all skulls.

Figure 4.2. Cranial model 3D printing placed in the dedicated stand for CT scan.

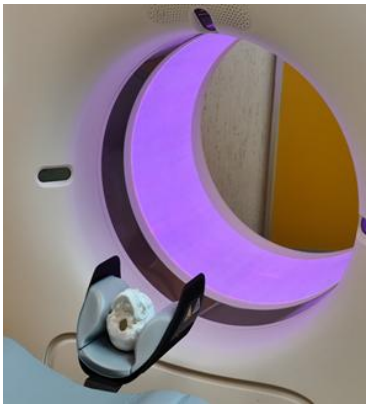

Figure 4.3. Cranial model 3D printing centered within the gantry using a cruciform laser system.

For each model, the transverse section corresponding to the maximum cranial diameter was identified following a slice selection strategy, with the aim that the measurement plane was anatomically homologous across all datasets. Once the reference plane was defined, the corresponding slice was extracted from each CT data. The transverse-plane analysis also served as a testbed for assessing how the FDM process reproduces curved and thin-walled bone structures when derived from clinical CT data. The combination of an anatomical plane and a fixed set of metrics allowed a structured comparison between the reference skull and its printed replicas, highlighting regions and quantities that are most sensitive to the combined effects of segmentation and fabrication (Figure 4.4).

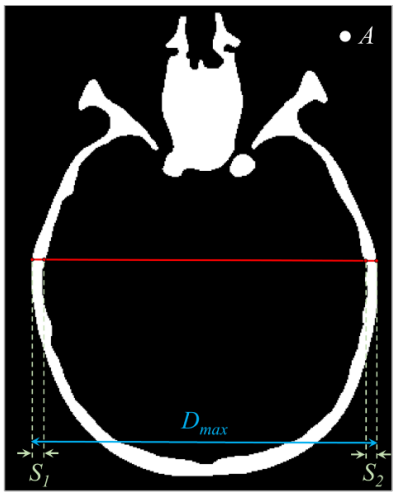

Figure 4.4. Mask of the CT slice in which the measured quantities being compared in transverse plane. A: area of skull section (white pixels); D_{max}: maximum longitudinal diameter; S_1 and S_2: skull thicknesses at D_{max}.

The quantification of the associated measurement uncertainty, including the contributions from CT pixel resolution, image analysis and slice selection, is described in Subchapter 4.3.1.4.

4.3.1.3 Coronal Plane Dimensional Assessment

To complement the transverse-plane analysis and to evaluate the robustness of the measurement protocol under modified imaging conditions, a second investigation was conducted on the coronal plane of the cranial model. The coronal plane, often referred to as frontal plane, is the vertical anatomical plane that divides the body into anterior and posterior portions [24]. All skulls were scanned following the same positioning procedure described previously but in different orientation: to perform the dimensional comparison under repeatability conditions, each skull model was meticulously placed on the motorized patient table using visual references for alignment and orientation, as shown in Figure 4.5.

Figure 4.5. Alignment and orientation of the models on the CT patient table

In addition, the cruciform laser system of the CT was used to center the model within the gantry ensuring that variations in model placement reflected only operator-dependent variability rather than uncontrolled motion or misalignment. To quantify the influence of this factor on the dimensional outcome, the reference skull was scanned six times, each following complete repositioning on the patient table. This procedure allowed the estimation of intra-operator variability independently of manufacturing differences, isolating the uncertainty component associated with the CT acquisition step. A single experienced radiology technician was responsible for positioning all skull models throughout the scanning. This allowed estimating the contribution of uncertainty due to the positioning procedure, regardless of the variability introduced by the printing process.

The coronal plane assessment followed the same core measurement principles adopted for the transverse analysis identifying the slice presenting the maximum outer diameter in the coronal direction automatically but for each CT dataset, an adaptive thresholding procedure was applied to generate the 3D mask of the model. The adaptive threshold is a grayscale value automatically adjusted for each acquisition based on the detected noise level. For each CT scan, noise is quantified as the highest gray level in slices where no part of the model was scanned. Once selected, the corresponding slice was used to extract the same set of geometric parameters used for the transverse plane (Figure 4.6).

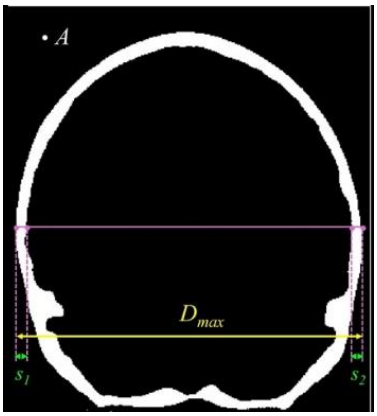

Figure 4.6. Example of a slice of the mask in which the maximum longitudinal diameter D_{max} is found in the coronal plane. A: area of skull section (white pixels); D_{max}: maximum longitudinal diameter; S_1 and S_2: skull thicknesses at D_{max}.

The uncertainty contributions specific to the coronal acquisition protocol and adaptive thresholding procedure are integrated into the general framework presented in Subchapter 4.3.1.4.

4.3.1.4 Image Analysis, Thresholding and Uncertainty Contributions

The two-dimensional assessment of the cranial model relies on an image-analysis workflow that converts CT greyscale data into binary masks, identifies the slice of maximum outer diameter and extracts geometric parameters such as section area, maximum longitudinal diameter and cortical thicknesses. On the selected slice, the area is obtained by counting the pixels belonging to the segmented mask and converting the pixel count into square millimeters using the nominal pixel size, while diameters and thicknesses are measured as distances between pairs of points on the mask boundary.

In order to ensure that these measurements can be interpreted within a quantitative quality control framework, a dedicated uncertainty analysis was carried out. The objective was to identify the main uncertainty contribution associated with CT image dimensional measurements and to provide estimating their combined effect on the derived quantities. In both transverse and coronal assessments, two primary contributions were considered: the uncertainty due to CT pixel resolution and the uncertainty associated with the image-analysis method, including segmentation threshold selection and slice identification.

The contribution related to pixel resolution was evaluated directly from the acquisition parameters, using the nominal pixel size associated with each CT protocol (Table 4.3 and Table 4.4). This component reflects the limit to the spatial resolution achievable with the imaging system. The

uncertainty contribution associated with the image-analysis method was estimated by Monte Carlo (MC) simulations with 10^4 iterations [22].

For the transverse-plane analysis, the greyscale threshold used for automatic segmentation of the 3D masks was modelled as a random variable with a rectangular distribution and bounds of ± 5% around the nominal threshold value. In addition, the identification of the slice with maximum diameter was allowed to vary within ±2 slices, also modelled by a rectangular distribution, to account for potential misalignment stemming from operator-dependent skull positioning errors during CT acquisition or small shifts in the slice selection process.

For the coronal-plane analysis, an adaptive thresholding procedure was introduced to automatically adjust the greyscale threshold for each acquisition based on the background noise level. In this case, the threshold was modelled with a rectangular distribution over ±10 greyscale levels, corresponding to the minimum number of grey levels usually distinguishable by the human eye in a noisy image [25], [26], [27], [28], [29]. The slice index at which the maximum diameter was detected was also perturbed within ±1 slice, again using a rectangular distribution, to quantify the effect of slice misidentification on the measured quantities. As in the transverse analysis, 10^4 MC iterations were performed and the resulting distributions of the dimensional quantities were used to estimate the uncertainty contribution associated with the image-analysis method.

For both anatomical planes, the combination of the contribution of the pixel resolution and the contribution of the image analysis was used to obtain a first estimate of the overall measurement of each geometric parameter using the uncertainty propagation law. Although the numerical values, expressed as standard deviation, of these uncertainty components are presented in Chapter 6, the methodology described above provides the conceptual framework adopted in CT-based dimensional measurements. It also clarifies the importance of imaging resolution, threshold selection, slice identification and operator dependence in determining the reliability of 2D CT-based dimensional assessment within PoC quality control workflows.

4.3.2 Three-Dimensional Assessment of Clavicle Model

Following the two-dimensional assessment conducted on the cranial model, the second part of the proposed dimensional assessment extends the analysis to the three-dimensional (3D) geometry of an anatomical structure. The study proposed moves on to 3D analysis of printed models: a preliminary volumetric assessment was carried out to investigate the repeatability of 3D printed bone models, fabricated by FDM (Fused Deposition Modeling) technology as stated in Subchapter

3.2.2 and Subchapter 3.3.2, with relevance to orthopedic applications. Six clavicle replicas were 3D printed using the same STL geometry and FDM printing parameters, including material, slicing strategy, infill density, build orientation and support generation. The use of a single G-code ensured that potential differences between replicas could be attributed primarily to the manufacturing process rather than to segmentation or mesh-optimization variability.

The goal of the 3D analysis was twofold. First, to quantify the volumetric variability among replicas produced under identical printing conditions, thereby assessing the repeatability of the FDM process in a clinical context by proposal a threshold percentage value indicative of the quality of the printing process. Second, to compare two CT-based measurement chains, using a diagnostic CT scan (CT-D), representative of equipment already available in hospital PoC settings, and an industrial CT scan (CT-I), designed for high-precision metrology and used as a reference system. By exploring the two advanced CT-based imaging techniques, commonly used in diagnostics and metrology, the intention was to proceed with QC protocols and improve understanding of methods that ensure the quality and safety of 3D printed models for clinical applications. By applying both techniques and comparing them, the study would provide insights into the effectiveness and performance in assessing the fidelity of 3D printed models: the aim is to identify a percentage discrepancy value between the models that could be representative of the quality of the printing process. For these reasons, the comparison is conducted between the printed replicas and not with the original model. The comparative analysis and estimation of uncertainty associated with each methods provide insight into the feasibility of using CT-D as a practical QC tool in PoC environments.

Subchapter 4.3.2.1 and Subchapter 4.3.2.2 describe the acquisition protocols, reconstruction procedures and volumetric calculation methods implemented for the diagnostic and industrial CT systems, respectively. The uncertainty contributions associated with each approach, including pixel resolution, slice thickness, adaptive thresholding and tetrahedral decomposition, follow the same methodological principles presented earlier for the two-dimensional cranial model, but extended to three-dimensional volume estimation.

4.3.2.1 Volumetric Assessment Techniques: Diagnostic CT

The first volumetric evaluation method relied on Diagnostic Computed Tomography (CT-D), performed using a Siemens Somatom Force® single-source system [23] configured to maximize image resolution. The acquisition parameters are reported in Table 4.5.

Table 4.5. Main settings of the CT-D scan protocol

CT Parameter	Setting
Pixel size	0.41 × 0.41 mm²
Total number of slices	911
Slice increment	0.4 mm
Slice thickness	0.4 mm
Voltage peak	120 kV
Single collimation width	0.30 mm

All six clavicle replicas were scanned in a single acquisition session to minimize inter-scan variability and to ensure consistent imaging conditions across the dataset (Figure 4.7). The DICOM dataset obtained for each scan was processed using a MATLAB workflow designed to automatically segment the clavicle volume using an adaptive thresholding method.

Figure 4.7. Setup for CT-D acquisition of the six 3D-printed clavicle replicas with Siemens Somatom Force.

The threshold was defined as the highest greyscale value detected in image regions containing only background noise. For each slice, a binary mask identifying the bone boundary was obtained, from which the enclosed area was calculated by pixel counting and conversion to mm² (Figure 4.8).

Figure 4.8. 2D mask of a CT-D slice obtained by automatic segmentation.

The 3D volume was computed by integrating the areas across slices, taking into account the slice thickness and employing interpolation to reconstruct the volume between consecutive masks. This image-analysis method is consistent with previous two-dimensional QC studies on skull models but extended to produce a volumetric measurement. The interpolation process involved averaging the pixel count difference between the areas of two consecutive mask slices to obtain the representation of the 3D structure. By repeating the abovementioned steps for the set of slices of a single bone model, the overall volume V_{CT} was estimated.

A comprehensive uncertainty analysis was performed, including pixel resolution, slice thickness and the uncertainty of the image analysis-based method. The latter contribution was estimated by means of a Monte Carlo simulation with 10^4 iterations for each bone model, where the adaptive threshold was varied within a ±5% uniform distribution, following the conventions used in prior QC imaging studies. Therefore, the overall measurement uncertainty of the volume $\sigma_{V,CT\text{-}D}$ was estimated by combining the above contributions through the uncertainty propagation law.

4.3.2.2 Volumetric Assessment Techniques: Industrial CT

The following proposed volumetric measurement method employed an Industrial Computed Tomography system (CT-I), the ZEISS METROTOM 1500 [30], which offers substantially higher spatial resolution and metrological accuracy than diagnostic CT. Each clavicle model was scanned individually, using a voxel size of 60 μm, enabling significantly finer geometric detail than the CT-D dataset (Figure 4.9).

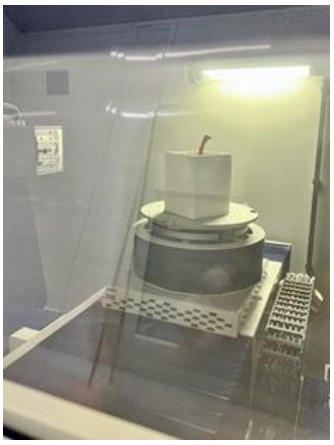

Figure 4.9. CT-I scan of a single model with ZEISS METROTOM 1500.

The CT-I reconstructions were processed using Zeiss Inspect software to generate a high-resolution STL mesh for each replica (Figure 4.10). The STL representation consists of a set of tetrahedra defined by vertex coordinates and faces. The volume of the object was calculated from the volume of STL.

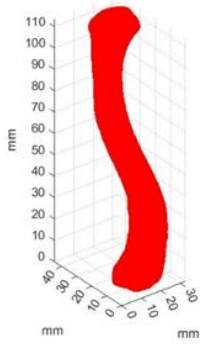

Figure 4.10. Example of STL file of a bone model generated from a CT-I scan.

Therefore, the volume V_{opt} was assessed as the sum of the volumes of the tetrahedra. The volume of the single tetrahedron V_{tet} was computed as follows [31]:

$$V_{tet} = \frac{1}{6} |\det \begin{pmatrix} v_1 \\ v_2 \\ v_3 \end{pmatrix}| \quad (1)$$

where v_1, v_2 and v_3 are the vectors identifying the tetrahedron in space with respect to the origin.

The uncertainty of the second processing method $\sigma_{V,CT\text{-}I}$ in evaluating the clavicle volume was estimated from the uncertainties of the volumes of the tetrahedra of which the STL file is composed, according to [32]. The uncertainty $\sigma_{V,tet}$ of the volume of a single tetrahedron was

estimated considering the uncertainty σ_{str} of 4 μm associated with the position of the single point in the cloud, identified by the module of the vectors v_1, v_2 and v_3, as follows:

$$\left(\frac{\sigma_{V,tet}}{V_{tet}}\right)^2 = \left(\frac{\sigma_{str}}{|v_1|}\right)^2 + \left(\frac{\sigma_{str}}{|v_2|}\right)^2 + \left(\frac{\sigma_{str}}{|v_3|}\right)^2 \quad (2)$$

In estimating the uncertainty of the total volume $\sigma_{V,CT\text{-}I}$, it must be taken into account that the uncertainty contributions $\sigma_{V,tet}$ of the individual volumes of the tetrahedra are dependent on each other. Therefore, the uncertainty $\sigma_{V,CT\text{-}I}$ was obtained summing these contributions.

Given its superior resolution CT-I was used as the reference measurement system against which CT-D estimates were compared. The analysis of discrepancies between the two method are presented in Chapter 6.

References

[1] P. Nguyen *et al.*, "Quality assurance in 3D-printing: A dimensional accuracy study of patient-specific 3D-printed vascular anatomical models," *Front. Med. Technol.*, vol. 5, p. 1097850, Feb. 2023, doi: 10.3389/fmedt.2023.1097850.

[2] N. Wake, B. Johnson, and S. Leng, "Quality assurance of 3D printed anatomic models," in *3D Printing for the Radiologist*, Elsevier, 2022, pp. 89–98.

[3] K. W. Shim, "Medical Applications of 3D Printing and Standardization Issues," *Brain Tumor Res. Treat.*, vol. 11, no. 3, p. 159, 2023, doi: 10.14791/btrt.2023.0001.

[4] O. K. Bowoto, S. A. Zahedi, and S. Chong, "Enhancing dimensional accuracy in 3D printing: a novel software algorithm for real-time quality assessment," *Int. J. Adv. Manuf. Technol.*, vol. 129, no. 7–8, pp. 3435–3446, Dec. 2023, doi: 10.1007/s00170-023-12543-2.

[5] V. A. Sears and J. M. Morris, "Establishing a Point-of-Care Virtual Planning and 3D Printing Program," *Semin. Plast. Surg.*, vol. 36, no. 03, pp. 133–148, Aug. 2022, doi: 10.1055/s-0042-1754351.

[6] B. Dorweiler, P. E. Baqué, R. Chaban, A. Ghazy, and O. Salem, "Quality Control in 3D Printing: Accuracy Analysis of 3D-Printed Models of Patient-Specific Anatomy," *Materials*, vol. 14, no. 4, p. 1021, Feb. 2021, doi: 10.3390/ma14041021.

[7] N. Sharma *et al.*, "Quantitative Assessment of Point-of-Care 3D-Printed Patient-Specific Polyetheretherketone (PEEK) Cranial Implants," *Int. J. Mol. Sci.*, vol. 22, no. 16, p. 8521, Aug. 2021, doi: 10.3390/ijms22168521.

[8] M. Odeh *et al.*, "Methods for verification of 3D printed anatomic model accuracy using cardiac models as an example," *3D Print. Med.*, vol. 5, no. 1, p. 6, Dec. 2019, doi: 10.1186/s41205-019-0043-1.

[9] L. Juergensen *et al.*, "Insights into geometric deviations of medical 3d-printing: a phantom study utilizing error propagation analysis," *3D Print. Med.*, vol. 10, no. 1, p. 38, Nov. 2024, doi: 10.1186/s41205-024-00242-x.

[10] P. Ravi, L. L. Chepelev, G. V. Stichweh, B. S. Jones, and F. J. Rybicki, "Medical 3D Printing Dimensional Accuracy for Multi-pathological Anatomical Models 3D Printed Using Material

Extrusion," *J. Digit. Imaging*, vol. 35, no. 3, pp. 613–622, June 2022, doi: 10.1007/s10278-022-00614-x.

[11] A. Fayed, "Preliminary Investigation of Dimensional Accuracy of 3D-Printed PLA—A Project-Based Learning Experience (WIP)," in *2024 ASEE Annual Conference & Exposition Proceedings*, Portland, Oregon: ASEE Conferences, June 2024, p. 47862. doi: 10.18260/1-2--47862.

[12] C. Arnold, L. Riß, J. Hey, and R. Schweyen, "Dimensional Accuracy of Different Three-Dimensional Printing Models as a Function of Varying the Printing Parameters," *Materials*, vol. 17, no. 14, p. 3616, July 2024, doi: 10.3390/ma17143616.

[13] I. A. Mohamed, M. S. El Attar, S. M. El Shabrawy, and E. Z. Alrafah, "Evaluation of dimensional accuracy, flexural strength and surface roughness of 3D-printable denture base resin modified with different concentrations of cerium oxide nanoparticles: a comparative in-vitro study," *BMC Oral Health*, vol. 25, no. 1, p. 568, Apr. 2025, doi: 10.1186/s12903-025-05840-7.

[14] S. Y. Lee *et al.*, "Accuracy and feasibility in building a personalized 3D printed femoral pseudoaneurysm model for endovascular training," *PLOS ONE*, vol. 19, no. 6, p. e0304506, June 2024, doi: 10.1371/journal.pone.0304506.

[15] K. Wendo *et al.*, "Dimensional Accuracy Assessment of Medical Anatomical Models Produced by Hospital-Based Fused Deposition Modeling 3D Printer," *J. Imaging*, vol. 11, no. 2, p. 39, Jan. 2025, doi: 10.3390/jimaging11020039.

[16] B. Msallem, N. Sharma, S. Cao, F. S. Halbeisen, H.-F. Zeilhofer, and F. M. Thieringer, "Evaluation of the Dimensional Accuracy of 3D-Printed Anatomical Mandibular Models Using FFF, SLA, SLS, MJ, and BJ Printing Technology," *J. Clin. Med.*, vol. 9, no. 3, p. 817, Mar. 2020, doi: 10.3390/jcm9030817.

[17] I. Gendviliene *et al.*, "Assessment of the morphology and dimensional accuracy of 3D printed PLA and PLA/HAp scaffolds," *J. Mech. Behav. Biomed. Mater.*, vol. 104, p. 103616, Apr. 2020, doi: 10.1016/j.jmbbm.2020.103616.

[18] C. Lebowitz *et al.*, "The Accuracy of 3D Printed Carpal Bones Generated from Cadaveric Specimens," *Arch. Bone Jt. Surg.*, no. Online First, Nov. 2020, doi: 10.22038/abjs.2020.50236.2495.

[19] C.-P. Hsu *et al.*, "Geometric accuracy of an acrylonitrile butadiene styrene canine tibia model fabricated using fused deposition modelling and the effects of hydrogen peroxide gas plasma sterilisation," *BMC Vet. Res.*, vol. 16, no. 1, p. 478, Dec. 2020, doi: 10.1186/s12917-020-02691-y.

[20] T. Tóth *et al.*, "Accuracy Verification of an Anatomical Model Manufactured Using Low-Cost Additive Production," *Appl. Sci.*, vol. 11, no. 2, p. 594, Jan. 2021, doi: 10.3390/app11020594.

[21] M. Kaschwich *et al.*, "Accuracy evaluation of patient-specific 3D-printed aortic anatomy," *Ann. Anat. - Anat. Anz.*, vol. 234, p. 151629, Mar. 2021, doi: 10.1016/j.aanat.2020.151629.

[22] "Dual Source CT." Accessed: Dec. 04, 2025. [Online]. Available: https://www.siemens-healthineers.com/it/computed-tomography/technologies-and-innovations/dual-source-ct

[23] "CT single source." Accessed: Dec. 08, 2025. [Online]. Available: https://www.siemens-healthineers.com/it/computed-tomography/single-source-ct

[24] J. H. Dirckx, "Dorland's Illustrated medical dictionary," *JAMA*, vol. 273, no. 10, pp. 821–822, 1995.

[25] T. Kimpe and T. Tuytschaever, "Increasing the Number of Gray Shades in Medical Display Systems—How Much is Enough?," *J. Digit. Imaging*, vol. 20, no. 4, pp. 422–432, Dec. 2007, doi: 10.1007/s10278-006-1052-3.

[26] J. Gille, L. Arend, and J. O. Larimer, "Display characterization by eye: contrast ratio and discrimination throughout the grayscale," in *Human Vision and Electronic Imaging IX*, B. E. Rogowitz and T. N. Pappas, Eds., SPIE, 2004, pp. 218–233. doi: 10.1117/12.532521.

[27] M. Kykta, "Gamma, Brightness, and Luminance Considerations for HD Displays," *Inf. Disp.*, vol. 25, no. 7, pp. 20–25, July 2009, doi: 10.1002/j.2637-496X.2009.tb00117.x.

[28] S. Bender, K. Lederle, C. Weiß, S. O. Schoenberg, and G. Weisser, "8-bit or 11-bit monochrome displays—which image is preferred by the radiologist?," *Eur. Radiol.*, vol. 21, no. 5, pp. 1088–1096, May 2011, doi: 10.1007/s00330-010-2014-1.

[29] R. Carter, "Gray-scale perceptions calculated: optimum display background luminance," *Appl. Opt.*, vol. 36, no. 8, pp. 1705–1717, 1997.

[30] "ZEISS METROTOM 1500: One CT. Many Applications." Accessed: Mar. 30, 2025. [Online]. Available: https://www.zeiss.com/metrology/en/systems/x-ray/3d-x-ray/metrotom-1500.html

[31] V. N. Parthasarathy, C. M. Graichen, and A. F. Hathaway, "A comparison of tetrahedron quality measures," *Finite Elem. Anal. Des.*, vol. 15, no. 3, pp. 255–261, Jan. 1994, doi: 10.1016/0168-874X(94)90033-7.

[32] International Organization for Standardization, *Uncertainty of measurement-Part 3: Guide to the expression of uncertainty in measurement (GUM: 1995)*. ISO, 2008.

Chapter 5

Mechanical Assessment

5.1 Role of Mechanical Assessment in the PoC workflow

Mechanical assessment represents a critical component of the *Inspection* step within point-of-care (PoC) additive manufacturing (AM) workflows, complementing dimensional verification by addressing the functional behavior of printed anatomical models and devices. While dimensional assessment ensures that printed anatomical models replicate the intended geometry, mechanical assessment evaluates whether the material response remains consistent with the functional requirements of the clinical application (Figure 5.1). As outlined in the workflow presented in Chapter 2, each phase, from image acquisition to printing process, can introduce deviations that affect not only geometric accuracy but also the material response of the final printed object, particularly in soft or elastomeric materials whose behavior is strongly influenced by printing parameters and post-processing conditions [1].

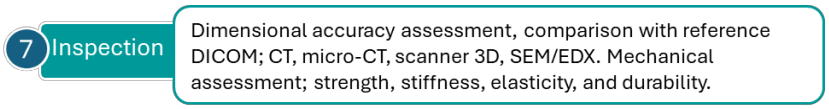

Figure 5.1. Step 7 of the PoC 3D-printing workflow: inspection. This phase integrates the mechanical assessment, through quantitative evaluation of strength, stiffness, elasticity and durability, with the dimensional assessment of the 3D printed model. Together, these operations provide measurable indicators of the functional suitability of the final model to clinical application.

Reproducing only the external shape is not enough [2]: the success of 3D printed soft models strongly depends on the mechanical performance of the printed materials, which must closely replicate the behaviour of biological tissues under different types of loading. Parameters such as tensile strength, elasticity, and elongation at break are crucial to ensure that the printed models respond realistically to manipulation, cutting, or suturing during medical procedures [3]. This requires a detailed mechanical characterization of the material, under different loading conditions, to understand how it behaves during manipulation, deformation or prolonged use [4], [5].

Despite its centrality, mechanical testing in PoC 3D printing remains considerably fragmented. The literature reports heterogeneous approaches in specimen preparation and testing configurations reflecting the lack of standardized procedures specifically tailored to photopolymers and other emerging materials manufactured by AM in clinical context [6], [7].

Existing standards for elastomers can be partially applied, but they are often not adequate, especially when considering the effects of sample geometry which properties measured using standard dog-bone specimens may not reflect those exhibited by anatomical geometries, as well as when considering print orientation and post-processing conditions [8]. Furthermore mechanical properties should be measured with methods that are feasible in a hospital setting, as well as with criteria for accuracy and acceptance that do not vary between different sites and printing technologies [9].

Within this context, the mechanical characterization performed in PoC is often limited to descriptive comparisons, and many PoC facilities rely on qualitative evaluations such as manual palpation or subjective clinician assessments of stiffness. Overall, mechanical evaluation contributes to establishing a structured quality control framework for PoC 3D printing, supporting traceability, repeatability and safety. Together with dimensional assessment, it forms the core of the "inspection" phase of the workflow, enabling hospitals to transition from experience-based validation to a measurement-based approach.

For these reasons, this doctoral work places particular attention on the mechanical assessment of anatomical models produced using PoC with a focus on soft materials and geometries that deviate even from standardized samples. By quantifying the mechanical response through tensile, dynamic and viscoelastic characterization and also by comparing the printed materials to biological references this work contributes to the development of reproducible, measurement-based quality control procedures suitable for clinical environments.

The following Subchapter 5.2 introduces the mechanical assessment methods most frequently employed in biomedical 3D printing, outlining the approaches reported in the literature and providing the conceptual basis for the experimental investigations developed in this thesis.

5.2 Mechanical Assessment Methods Form Literature

Mechanical assessment in PoC 3D printing encompasses a broad range of test setups designed to evaluate the functional behavior of 3D printed parts under different conditions. The selection of appropriate test methods is influenced by the intended clinical application, the type of material used and the geometry of the printed component. Studies employ a broad range of test configurations, specimen geometries and performance metrics, often reflecting local practices rather than shared methodological principles. Depending on the application (e.g., surgical simulation, implantable guides or external orthoses), tests typically involve tensile, compressive, three point bending, creep or fatigue loading tests under laboratory conditions. A synthesis of the main mechanical test configurations, instruments, and where is it available, a quantitative acceptance thresholds reported in recent biomedical 3D printing studies are provided in Table 5.1.

Górski et al. compared polylactic acid (PLA) and thermoplastic elastomer (TPE) prosthetic sockets fabricated by FDM using compressive tests, showing that no socket failed or deformed below the set threshold of 1000 N of maximal compressive force, representing a static compression using an item of ~100 kg mass. Authors underline the absence of available standards for conducting such tests on 3D-printed sockets so they used as a partial reference the ISO 10328 standard [10]. Since most of the tested sockets reached values well above 3500 N, the authors highlight that geometry could be topologically optimized for less volume and weight and better comfort of the patient through setting material and the infill levels [11].

Lukaszewski et al. evaluated a polyethylene terephthalate glycol (PET-G) wrist-hand orthosis printed by FDM by a three-point bending test with Sunpoc WDW-5D-HS testing machine, varying the geometry of the sample and printing parameters. Break loads exceeding 900 N were reported, but no acceptance criterion is indicated [12]. Subsequent investigations focused on establishing quantitative and acceptance limits for printed medical parts. Ling et al. characterized a digital light processing (DLP) printed model resin by carrying out a three-point bending test, tensile test, indentation tests and the impact strength test. The aim of the study was to evaluate the mechanical properties of a novel 3D-printing model resin and compare it to eight commercially available model resins. They do not explicitly state an acceptance criterion or threshold for each estimated mechanical quantity [13].

Majdak et al. tested FDM-printed orthotic fragments under compression, obtained fracture loads between 681 and 914 N, depending on the height of the test samples and infill density. They used 300 N as the minimum threshold, which, according to reports, corresponds to a value

established in agreement with an orthopedic expert [14]. During the same period, Henriques et al. studied soft SLA-printed polymers used in vascular phantoms, measuring, by performing a static and dynamic tensile test, the elastic moduli. They declared the mechanical properties of the materials studied are consistence with those reported in the literature without specifying an acceptance value [15]. Complementary findings were reported by Jiménez et al., who assessed tracheal models printed in polycaprolactone (PCL), polydioxanone (PDO) and PLA using FDM technology. Three point bending test and radial test found variation in Young's modulus depending on material type, emphasizing that printer parameters should be specifically optimized for each of the materials to ensure proper interlayer adhesion, dimensional accuracy, and structural quality of the complex geometries [16].

Table 5.1. Summary of direct linear metrology approaches reported in recent PoC studies.

Study and year	Measurement Instrument	Nominal Resolution	QC Acceptance Threshold	Ref.
Górski et al., 2021	Compressive tests	Sunpoc WDW-5D-HS	1 kN before failure	[11]
Lukaszewski et al., 2023	Three-point bending test	Sunpoc WDW-5D-HS	-	[12]
Ling et al., 2024	Three-point bending test; tensile tests; indentation tests; impact strength test;	Shimadzu AGS-X; Impressor GYZJ-935; Pendulum Impact Tester Model IT504	-	[13]
Majdak et al., 2024	Loading capacity test	Tensolab 3000 Strength Tester	300 N as minimum threshold	[14]
Henriques et al., 2025	Static and dynamic tensile tests; hardness test	Instron 6800 - 68TM5; ViaIndustrial X.F. Type A durometer	-	[15]
Jiménez et al., 2025	Three-point bending test; Radial tests	Zwick Roell universal testing machine with radial module	-	[16]
Kulker et al., 2025	Tensile tests	Zwick Roell universal testing machine	-	[17]

Overall, the body of literature highlights a fragmented landscape of methods, instrumentation and reporting conventions. In many cases, mechanical testing is carried out primarily as a means

of material characterization, aimed at describing the behavior of printed polymers under specific loading conditions, rather than identifying quantitative thresholds that define acceptable mechanical fidelity. As a result, the obtained values rarely indicate in a quantitative way whether a printed model adequately reproduces the behavior of real tissues or meets predefined functional requirements. This lack of convergence stresses the need for structured and universally recognized QC protocol in hospital manufacturing environments.

5.3 Proposed Mechanical Assessment

The mechanical assessment developed in this doctoral work was designed to propose a repeatable framework for evaluating the behavior of soft 3D-printed materials and models intended for PoC applications. This framework integrates two complementary experimental activities that reflect the dual needs of PoC environments: on the one hand, the evaluation of anatomically realistic models that must reproduce the mechanical response of pediatric airway tissues during clinical training or procedural simulation; on the other, the quantitative characterization of the mechanical properties of rubber-like photopolymers commonly used biomedical applications, indagating on the influence of the printing parameters.

The first part of the assessment concerns models printed in Flexible 80A Resin using stereolithography (SLA). This material was selected to reproduce the mechanical response of pediatric airway structures, and the evaluation was conducted on three geometries: anatomically tracheal segments derived from CT data, simplified cylindrical specimens replicating average tracheal dimensions, and ISO-standard tensile specimens. This combined approach allows the mechanical behaviour of the material to be examined under conditions that replicate those adopted in tests on real tracheal tissues, while also ensuring controlled laboratory settings. Through quasi-static tensile tests, dynamic mechanical analysis and creep testing, it was possible to quantify the elastic modulus, viscoelastic response and time-dependent deformation of the resin, providing insights into how the material behaves during simulated airway procedures.

The second part of the assessment focuses on dog-bone specimens printed with PolyJet technology in Agilus30™, a soft photopolymer widely adopted for flexible anatomical models. Standardized tensile tests were performed to analyze the influence of build orientation on mechanical response and to provide an initial verification of the consistency and suitability of this material under controlled loading. This approach enables the identification of anisotropy effects

and supports the definition of reproducible methods for material characterization within PoC workflows.

By integrating the SLA- and PolyJet-based investigations, the mechanical assessment proposed in this work defines a coherent inspection step that can be incorporated into PoC quality control workflows. The methodology provides: (i) quantification of the elastic and tensile behavior of soft photopolymers, (ii) characterization of viscoelastic and time-dependent responses under conditions representative of clinical use, and (iii) traceable mechanical indicators supported by a structured uncertainty evaluation. In addition, a specific objective of this work is to propose a method for estimating the mechanical parameters of rubber-like materials suitable for PoC environments and implementable without the need for advanced computational resources. The indicators obtained through this framework can be compared with published mechanical properties of biological soft tissues or with predefined functional requirements specific to the clinical setting. Ultimately, the purpose of this work is not only to characterize the mechanical response of 3D-printed materials but also to contribute to the identification of preliminary acceptance thresholds that may serve as indicators of whether a printed model demonstrates sufficient mechanical fidelity for its intended application.

5.3.1 Mechanical Assessment of SLA Printed Specimens

The first phase of the proposed mechanical assessment focuses on stereolithography (SLA). All mechanical tests on SLA printed components were carried out on the specimens introduced in Subchapter 3.3.3 and Subchapter 3.3.4, using the geometries described there: anatomical trachea models, simplified cylindrical sections and ISO 527-1A tensile specimens. These geometries were tested to quantify the elastic, viscoelastic and time-dependent response of Flexible 80A Resin. Mechanical tests were performed on six specimens for each configuration, with the aim of evaluating the mechanical response of the 3D-printed material under loading conditions. Mechanical tests were performed on six specimens for each configuration, which represents the minimum sample size recommended by standards for polymer tensile testing (e.g., ISO 527-1A requires at least five specimens). Furthermore, this choice ensures statistical robustness while maintaining experimental feasibility according to principles of error analysis [18], [19]. The experimental campaign comprised three distinct protocols: quasi-static tensile testing, dynamic frequency sweep tests and long-duration creep tests.

Quasi-static tensile tests were performed on all specimen geometries, including the ISO 527-1A samples, to determine their elastic properties. On the other hand, dynamic and creep tests were

conducted on the anatomical and cylindrical specimens only. This choice was motivated by two main considerations: (a) these geometries more closely replicate the actual conditions and mechanical constraints expected in clinical applications, and (b) their robust structure offers greater stability during long-duration testing, reducing the risk of misalignment or failure under constant load. The aim was to investigate how the airway model would respond to oscillatory and long-term loading conditions, replicating the types of mechanical stresses that may occur during simulated surgical procedures or extended handling.

The following subchapters describe in detail the mechanical testing setup, the procedures adopted, and the processing of the acquired data. Subchapter 5.3.1.1 introduces the characteristics of the testing machine and outlines the experimental configurations used for static, dynamic and creep loading conditions. Subchapter 5.3.1.2 presents the methods employed for mechanical characterization, including the estimation of Young's modulus, the computation of storage and loss moduli, and the analysis of time-dependent behavior. Subchapter 5.3.1.3 details the measurement uncertainty analysis associated with the tests, reporting the contributions arising from specimen geometry, displacement and strain measurement, load and stress evaluation, and the propagation of uncertainty in the mechanical parameters derived from static, dynamic and creep tests.

5.3.1.1 Testing Machine

Mechanical characterization was carried out using the ElectroForce TA3300 load frame, a Dynamic Mechanical Analysis (DMA) system. According to the manufacturer's specifications, the instrument can perform tests over a frequency range from 0.00001 Hz to 100 Hz, with a frequency accuracy of ± 0.1% of the operating value. This capability enables the execution of static, quasi-static and dynamic tensile tests, as well as creep analysis, within a single experimental platform. The testing machine is equipped with a 3 kN ± 1% load cell and a temperature-controlled chamber. The chamber was monitored via a type K thermocouple, with a measurement uncertainty of ± 0.5 °C. The main technical specifications of the ElectroForce TA3300 system and its instrumentation are summarized in Table 5.2.

Tests were performed at a controlled temperature of 23.0 ± 0.5 °C, replicating the ambient conditions typically found in clinical settings, especially during surgical simulation and preoperative training scenarios. Due to the non-standard geometries of the anatomical and cylindrical specimens, clamps were used to gently secure them to the machine handles. Particular care was

taken during assembly to avoid excessive force or damage to the specimens. The initial gauge length (i.e., the distance between the handles in the unformed state) was 75.0 ± 0.5 mm and no pre-tension was applied before testing. For the ISO 527-1A specimens, initial conditions and testing procedures were set according to the standard, in particular, the clamping length was set 115.0 ± 0.5 mm. No pre-conditioning was required. In particular, the choice of no pre-tension is consistent with the reference standards ISO 527 (tensile tests on plastics), ISO 37 (tensile tests on elastomers), and ISO 899-1 (creep tests on plastics), none of which prescribe the use of a mandatory pre-load. For consistency, all static, dynamic, and creep tests in this study were therefore performed without applying any initial load, starting from the specimen's undeformed state.

Once the initial length was set, the displacement between the grips was monitored by a High-Aspect-ratio Dielectric Sensor (HADS) installed directly on the machine with a measurement uncertainty of ± 0.025 mm. All specimens were positioned in the testing machine in vertical orientation, with their longitudinal axis aligned with the direction of applied tensile load. Figure 5.2 shows the clamping arrangement for the three geometries.

Table 5.2. Main technical specifications of the ElectroForce TA3300 testing system.

Parameter	Value
Load frame model	ElectroForce TA3300
Load cell capacity	3 kN ± 1%
Frequency range	0.00001-100 Hz ± 0.1%
Thermocouple uncertainty	± 0.5 °C
Displacement resolution	± 0.025 mm

(a) (b) (c)

Figure 5.2. Test setup for the three specimen geometries: (a) anatomical, (b) cylindrical, and (c) ISO 527-1A specimens in the ElectroForce TA3300 testing machine.

5.3.1.1.1 Static Test

Static tensile tests were performed to evaluate the elastic and deformation behavior of the materials under low-rate loading conditions. A maximum elongation of 12 mm was applied to each specimen, in accordance with the stroke limitations of the testing machine. This elongation corresponds to a strain of less than 20% of each initial specimen length, ensuring consistency with values reported in the literature for similar applications and avoiding failure of the specimens during testing [20]. In particular, to a strain of approximately 16% for both the anatomical and cylindrical specimens, and approximately 10% for the standard one. The latter have a lower percentage elongation due to the higher initial length of the test sample. The elongation was applied at a constant rate of 0.16 mm/s.

Force and displacement data were continuously recorded during each test, showed in Figure 5.3, allowing the derivation of stress-strain curves for all specimen types. From the average stress–strain response, the elastic modulus was estimated.

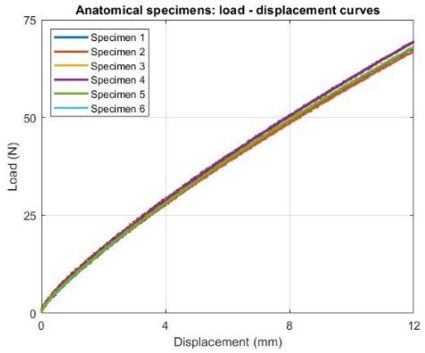

(a)

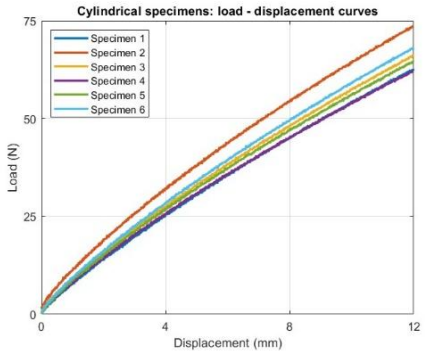

(b)

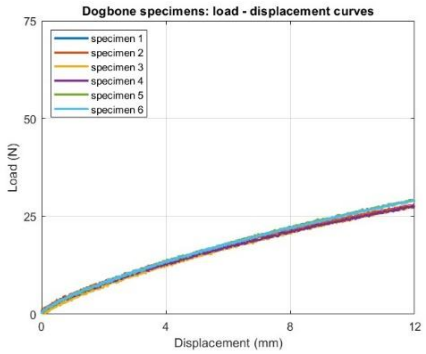

(c)

Figure 5.3. Raw load–displacement data from quasi-static tensile tests for the six specimens of each geometry: (a) anatomical, (b) cylindrical, and (c) ISO 527-1A dog-bone shape.

5.3.1.1.2 Dynamic Test

Dynamic mechanical testing was carried out on anatomical-shaped and cylindrical specimens to evaluate their viscoelastic behavior over a range of excitation frequencies. The test was configured as a sinusoidal tension–compression sweep around a defined mean strain level. The nominal test parameters were set as follows:

- mean strain level: 2 mm;
- dynamic amplitude: ± 1 mm;
- frequency range: from 1 Hz to 36 Hz, in increments of 5 Hz.

This frequency sweep allowed the evaluation of the storage modulus (E'), loss modulus (E''), and loss factor (tan δ), which are the indicators of the material energy dissipation capacity and stiffness variation with frequency. The frequency sweep aimed to characterize the viscoelastic response of the printed material rather than replicate physiological tracheal loading. In line with ISO 6721-4, which recommends testing polymers in the range 0.01–100 Hz, the selected frequency window of 1–36 Hz ensures a representative evaluation of frequency-dependent behavior. The upper limit was set below 40 Hz, as suggested by the instrument manufacturer, to avoid potential resonance effects related to the relatively large moving masses of the testing system when operated with the temperature-controlled chamber.

The raw data acquired during these tests are reported in Figure 5.4, Figure 5.5 and Figure 5.6, from which average values and their dispersions were subsequently computed. These viscoelastic

parameters are particularly relevant for applications such as surgical simulation, where tissues may experience repetitive or oscillatory forces during clinical procedures.

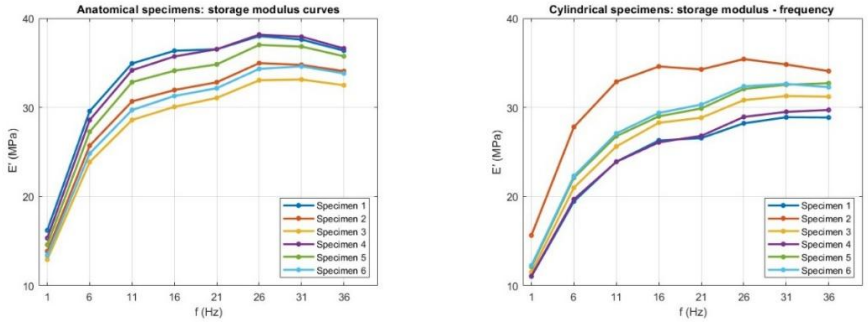

(a) (b)

Figure 5.4. Raw storage modulus (E') data as a function of frequency for (a) anatomical and (b) cylindrical specimens.

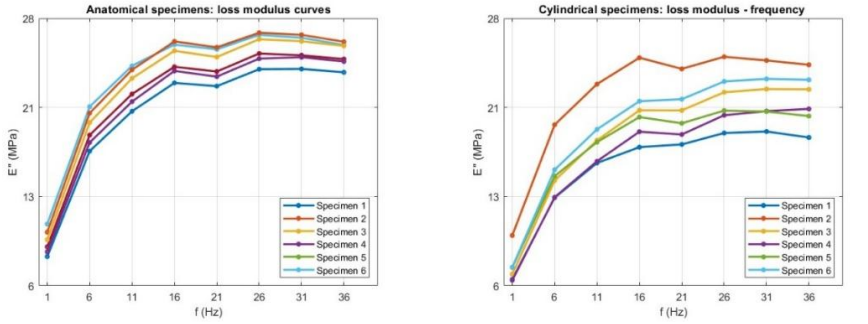

(a) (b)

Figure 5.5. Raw loss modulus (E'') data as a function of frequency for (a) anatomical and (b) cylindrical specimens.

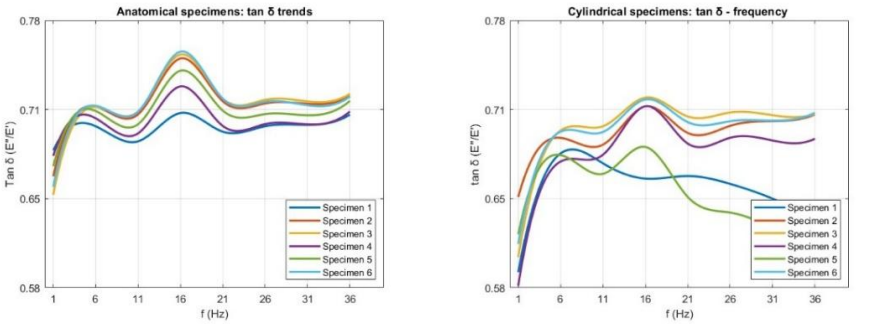

(a) (b)

Figure 5.6. Raw loss factor (tan δ) data as a function of frequency for (a) anatomical and (b) cylindrical specimens.

5.3.1.1.3 Creep Test

Creep tests were carried out to evaluate the time-dependent viscoelastic behavior of the material under sustained mechanical loading, simulating conditions such as prolonged tissue manipulation or extended handling during surgical training.

To enable a direct comparison of the viscoelastic behavior of the real trachea, the tests were performed under replicated loading conditions [21]. Consequently, a constant tensile load of 10 N ± 1% was applied and maintained via the closed-loop control of the testing machine for both anatomical and cylindrical specimens.

The experimental protocol consisted of two sequential stages, designed to capture both the immediate and the long-term components of the creep response. The first stage was a short-term, high-frequency acquisition performed immediately after load application, with the objective of resolving the instantaneous elastic deformation. Test parameters for this step were: scan time of 1 s and 1200 points acquired per scan (sampling frequency of 1200 Hz). This high temporal resolution ensured that the rapid strain change upon loading could be captured safely. The data acquired for this first stage are reported in Figure 5.7.

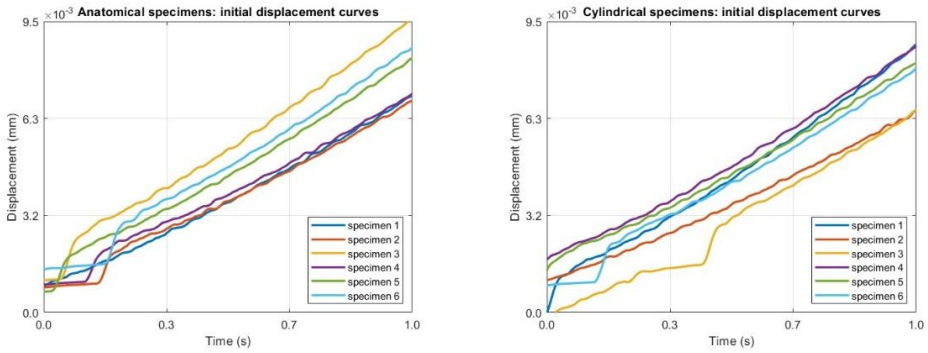

(a) (b)

Figure 5.7. Raw displacement–time data under a constant tensile load of 10 N from Step 1 (high-frequency acquisition at 1200 Hz for 1 s) for (a) anatomical specimens and (b) for cylindrical specimens.

The second stage involved a long-duration creep test. Test parameters for this step were: 2400 seconds (40 minutes), and displacement data were recorded at regular intervals of 100 seconds (sampling frequency of 0.01 Hz). The data acquired for this first stage are reported in Figure 5.8. Since the duration of the test is 40 minutes, the experiment falls within the primary creep, with decreasing strain rate, and secondary creep regime, where the strain rate becomes nearly constant. No tertiary creep stage was observed, as the specimens did not reach failure under the applied load.

The combination of high-resolution initial data and long-term creep tests will provide a comprehensive experimental basis for describing the viscoelastic response of the tested specimens.

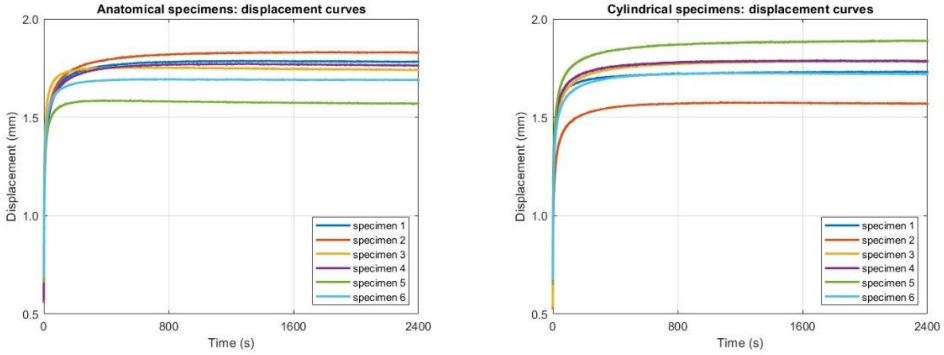

(a) (b)

Figure 5.8. Raw displacement–time data from Step 2 (long-duration acquisition at 0.01 Hz over 2400 s) for (a) anatomical specimens and (b) for cylindrical specimens.

5.3.1.2 Mechanical Characterization

This section presents the mechanical properties derived from the experimental data collected during the mechanical testing campaign. These properties describe the elastic, viscoelastic, and time-dependent behavior of the tested material under different loading conditions. Specifically, the estimation of the Young's modulus, which quantifies the initial elastic response of the material under quasi-static loading, the evaluation of storage and loss moduli, extracted from dynamic tests and used to characterize the frequency-dependent viscoelastic behavior and the primary and secondary creep behavior, based on long-duration constant-load tests, providing insights into the material performance under prolonged mechanical stress.

5.3.1.2.1 Young's Modulus

Stress-strain curves were obtained from the data recorded during quasi-static tensile tests using the WinTest® proprietary software of the testing machine. Post-processing was conducted in MATLAB to analyze and quantify the material's elastic response. To estimate the Young's modulus, an average stress-strain curve was computed from the six individual curves by interpolating stress values at equal strain intervals. The variability among samples was quantified by computing the standard deviation (SD) of stress at each strain level, allowing assessment of the test repeatability. A weighted linear regression approach [18] was employed to approximate the average curve with a series of linear segments. The weighting was based on the measured SD of stress for each sample, ensuring that data with lower uncertainty contributed more significantly to

the fit. From this piecewise linear approximation, the Young's modulus was estimated as the slope of each segment. Specifically, a polynomial function of degree *m* was first fitted to the average curve to identify *n* optimal intervals, each corresponding to a distinct segment. From each segment, the elastic modulus value E_i (i = 1, …, n) was extracted as a function of the corresponding strain range.

5.3.1.2.2 Storage Modulus, Loss Modulus and Loss Factor

For anatomical and cylindrical specimen type, dynamic mechanical data were acquired from six individual tests using the WinTest® proprietary software. During each test, the system imposed the sinusoidal displacement profile as indicated in Subchapter 5.3.1.1.2. and, based on the input geometrical parameters of the specimens, directly computed the storage modulus (E') and loss modulus (E''). The loss factor (tan δ) was obtained as the ratio E''/E'.

The raw values of E', E'', and tan δ from the six repetitions for each specimen type were then processed in MATLAB. For each frequency, an average value was estimated for each viscoelastic parameter by aligning the data sets to equal frequency values, while the variability between samples was quantified using standard deviation, providing an estimate of the dispersion of the results.

5.3.1.2.3 Creep Analysis

To characterize the material viscoelastic behavior, the creep test data were analyzed in two distinct stages, corresponding to the experimental protocol outlined in Subchapter 5.3.1.1.3. For each specimen type, the analysis was performed on a mean creep curve and its associated dispersion, which were calculated from the six experimental curves obtained for that specific geometry.

The instantaneous elastic strain, which represents the material response at the precise moment of load application, was determined from the high-frequency acquisition data (Stage 1). This value was calculated as the intercept of the creep curve and is a key parameter for the subsequent modeling. It corresponds to the initial elastic element of a Burgers model, composed of a spring and dashpot in parallel with a second spring and dashpot in series, but this was only used to determine the initial strain response [22].

For the long-term creep behavior (Stage 2), a Generalized Maxwell model was adopted to fit the time-dependent strain data. This model was chosen for its ability to accurately describe both the transient (primary creep) and steady-state (secondary creep) phases observed during the 40-minute test duration. The model is composed of a purely elastic spring (E_0) in parallel with a

number of Maxwell elements. Each Maxwell element consists of a spring (E_i) and a dashpot (η_i) in series [23].

The total creep strain ε(t), starting from the instantaneous deformation, is described as follows:

$$(\boldsymbol{t}) = \boldsymbol{\varepsilon_0} + \sum_{\boldsymbol{i=1}}^{\boldsymbol{n}} \frac{\boldsymbol{\sigma_0}}{\boldsymbol{E_i}} \left(\mathbf{1} - \boldsymbol{e}^{-\frac{\boldsymbol{t}}{\boldsymbol{\tau_i}}}\right) \quad (3)$$

where:

- $\boldsymbol{\varepsilon_0} = \frac{\boldsymbol{\sigma_0}}{\boldsymbol{E_0}}$ is the instantaneous elastic strain determined from the initial loading phase;
- $\boldsymbol{\sigma_0}$ is the constant applied stress;
- $\boldsymbol{\tau_i} = \frac{\boldsymbol{\eta_i}}{\boldsymbol{E_i}}$ represents the relaxation time for the i^{th} Maxwell element, which governs the rate of creep.

The experimental data from Stage 2 were fitted to this equation to determine the viscoelastic parameters (E_i and τ_i) that best describe the material time-dependent response. This dual-stage approach ensured that both instantaneous and long-term behaviors were captured and modeled. The methodology for obtaining the viscoelastic parameters of elastomers thorough the Burgers model and generalized Maxwell model is detailed in [24].

The fitting procedure was performed using a non-linear regression algorithm within dedicated data analysis software, with the goal of minimizing the difference between the model curve and the experimental data points. The goodness of fit was evaluated using standard statistical metrics. The coefficient of determination R^2 was used to quantify the correlation between the model and the experimental data. Additionally, the Root Mean Square Error (RMSE) was calculated to measure the average magnitude of the difference between the predicted and observed values.

5.3.1.3 Measurement Uncertainty Analysis

In this section, the measurement uncertainties associated with the experimental results are described. The analysis follows the principles of the uncertainty propagation law, taking into account the main sources of errors. For each investigated mechanical property, the combined uncertainty was obtained by considering: (a) the repeatability of the tests; (b) the instrumental and dimensional uncertainties associated with the measurement system and (c) the influence of data processing methods, such as curve fitting or derived quantities.

5.3.1.3.1 Specimen Geometry

The uncertainty associated with specimen geometry was estimated based on the dimensional accuracy of the 3D printer (± 0.025 mm), which was taken as the standard uncertainty for each linear dimension. For quantities derived from multiple measured dimensions (e.g., cross-sectional area), the uncertainties were propagated according to the uncertainty propagation law.

5.3.1.3.2 Displacement and Strain

Uncertainty about displacement measurements was determined from two contributions: (a) the resolution displacement of the testing machine transducer, as reported in the calibration certificate (0.025 mm), and (b) the variability in the displacement data recorded during repeated tests.

Strain uncertainty was obtained by propagating the displacement uncertainty together with the uncertainty in the initial gauge length of the specimen, estimated according to the protocol described in Subchapter 5.3.1.1.

5.3.1.3.3 Load and Stress

Uncertainty in the applied load was estimated from two sources: (a) the calibration certificate of the testing machine's load cell, with has a nominal capacity of 3 kN and an accuracy of ± 1% of the indicated value and (b) the variability in the load data recorded during repeated tests. The uncertainty in stress was then obtained by propagating the load uncertainty together with the uncertainty in the specimen's cross-sectional area, as described in Subchapter 5.3.1.3.1.

5.3.1.3.4 Young's Modulus

The measurement uncertainty of Young's modulus was estimated by applying the uncertainty propagation law, considering: (a) the repeatability of the tests, which influences the estimated slope of the stress–strain curve as determined through weighted linear regression, and (b) the uncertainties in stress and strain, derived according to Subchapter 5.3.1.3.2 and Subchapter 5.3.1.3.3, respectively, in line with the definition of the elastic modulus as the ratio between these two quantities.

5.3.1.3.5 Storage Modulus, Loss Modulus and Loss Factor

Given that E', E" and tan δ are directly computed by the testing system from the measured force, displacement and specimen dimensions under sinusoidal loading, the associated uncertainties for E' and E" were quantified from the dispersion of results across the six specimens for each geometry.

For the loss factor (tan δ), a derived quantity defined as the ratio E''/E', the combined standard uncertainty was obtained by propagating the uncertainties of E' and E" in accordance with the uncertainty propagation law and by adding the contribution from the dispersion observed in the repeated tests.

5.3.1.3.6 Creep Test

The first sources of uncertainty considered were those associated with the recorded displacement and the constant stress applied, estimated as described in Subchapter 5.3.1.3.2 and Subchapter 5.3.1.3.3. To estimate the uncertainty associated with material constants, except for that associated with the instantaneous elastic modulus (E_0), which was estimated as described in Subchapter 5.3.1.3.4, a Monte Carlo simulation with 10^5 iterations was carried out, which is particularly suitable for propagating uncertainties in non-linear regression models [25], [26]. Starting from the uncertainties expressed as standard deviations for the quantities described above (strain and applied stress), the Monte Carlo simulation was carried out as follows: at each iteration, a new, simulated set of strain data was generated by adding random noise to the average experimental strain curve. This noise was drawn from a normal distribution with a mean of zero and a SD equal to estimated uncertainty in terms of standard deviation associated with strain. Additionally, for the most complete analysis, a simulated value of the applied stress was also generated from a normal distribution defined by its mean and its SD. Each simulated dataset was then fitted to the generalized Maxwell model, yielding a new set of parameters. The final uncertainty for each parameter was then determined as the standard deviation of the 10^5 parameter values obtained from the simulation.

5.3.2 Mechanical Assessment of PolyJet Printed Specimens

The second phase of the proposed mechanical assessment focuses on PolyJet technology, which represents a more recent printing for soft anatomical models compared to stereolithography. Mechanical tests on PolyJet-printed components were conducted on the standardized dog-bone specimens introduced in Subchapter 3.3.4, fabricated in Agilus30™. These preliminary tests were specifically designed to evaluate the tensile behavior of a rubber-like material under controlled conditions and to investigate the influence of build orientation, which is known to affect the mechanical response of 3D printed models.

The aim of this activity was to propose a reproducible baseline for mechanical characterization of PolyJet materials by testing standard geometries before extending the QC approach to anatomical models produced with the same technology. The same guiding principles adopted for the SLA investigation were used here: repeatability of measurements, applicability of the method within PoC workflows and extraction of mechanical parameters through procedures that do not require complex computational tools.

In this context, tensile tests were selected as the most suitable and controlled method for a first characterization of Agilus30™, enabling the estimation of Young's modulus, tensile performance and potential anisotropy associated with different printing orientations, as well as allowing comparison with the manufacturer's material specifications to investigate the effect of the printing process. Tests were therefore performed on eight specimens for each printing configuration, following the same rationale adopted for SLA specimens, with the aim of assessing the mechanical response of the 3D printed material under uniaxial tension in this preliminary phase, prior to extending the QC framework to anatomically complex geometries also for PolyJet printing.

The following subchapters describe in detail the mechanical testing setup, the procedures used for static tensile loading and the data-processing methods applied to derive mechanical indicators. Subchapter 5.3.2.1 introduces the characteristics of the testing machine and the configuration adopted for the PolyJet specimens. Subchapter 5.3.2.2 presents the mechanical characterization approach, including the estimation of Young's modulus through a piecewise fitting strategy and the determination of ultimate tensile properties. Subchapter 5.3.2.3 details the uncertainty analysis performed for these tests, explaining how measurement contributions were propagated to obtain a single, comprehensive uncertainty associated with the estimation of Young's modulus.

5.3.2.1 Testing Machine

A tensile test was conducted using the Shimadzu Autograph AGS-X testing machine, equipped with a 5 kN load cell. Figure 5.9 shows an example of a specimen placed in the clamps at the start of the test and after the break at the end of the test. The main characteristics of the machine, as provided in the manufacturer's technical datasheet, are summarized in Table 5.3 [27]. Tests were performed under controlled laboratory conditions, with a temperature of 20 ± 2°C and a relative humidity of 55 ± 5 %.

Table 5.3. Main characteristics of the testing machine

Model	**Load Cell**	**Position Resolution**	**Testing speed precision**
Shimadzu AGS-X	5 kN ± 1%	0.01 mm	± 0.1 %

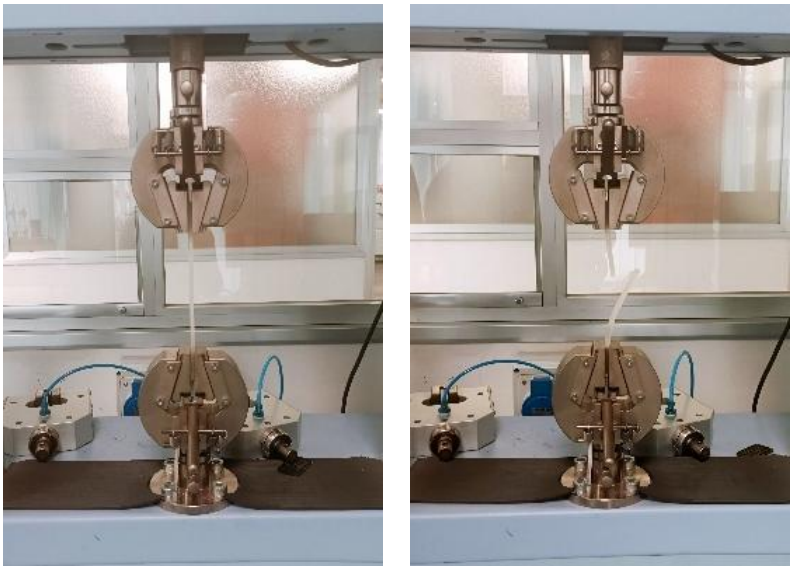

(a) (b)

Figure 5.9. Example of a specimen positioned in the testing machine Shimadzu Autograph AGS-X (a) at the start of the test and (b) after the break at the end of the test.

5.3.2.1.1 Static Test

The tensile test was carried out at a constant strain rate of 50 mm/min and the initial clamps distance was set at 115 mm. The specimens were tested in two separate sequences: first, those printed in the vertical orientation, followed by those printed in the horizontal orientation. During

the test, stress-strain curves were recorded to analyze the mechanical response of the specimens. Figure 5.10 presents the stress-strain curves obtained for the eight horizontally (Figure 5.10a) and eight vertically oriented specimens (Figure 5.10b). The horizontally oriented specimens show a regular trend and achieve elongation at break (ε_r) between 125% and 145%. In contrast, the stress values recorded for the vertically oriented specimens show slight instabilities, which could be attributed to the potential failure of the bond strength between the layers positioned orthogonally to the applied load. Due to this aspect, vertically oriented specimens have a lower ε_r. In particular, the maximum elongation values recorded are between 80% and 110%.

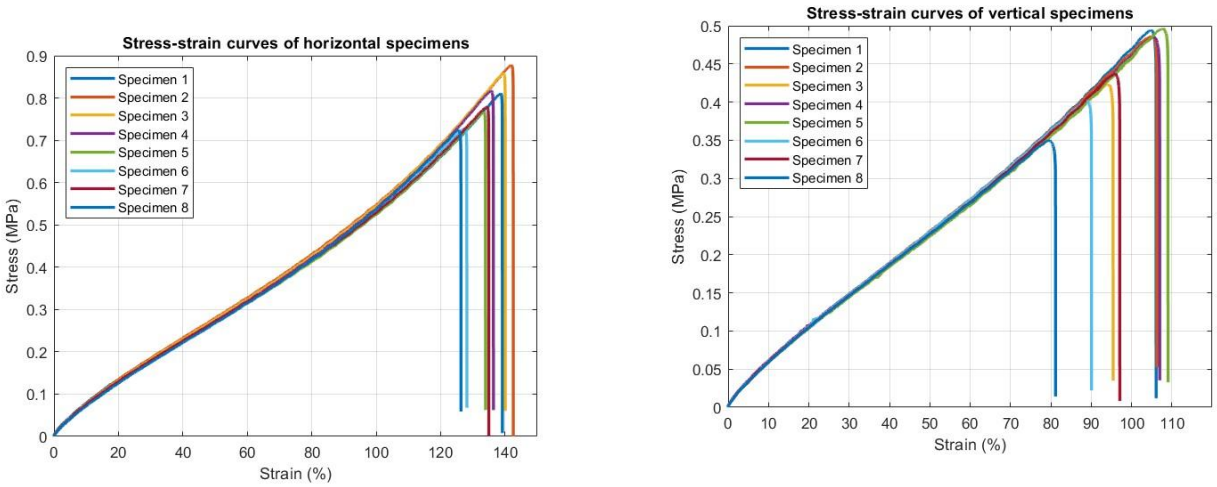

(a) (b)

Figure 5.10. Stress-strain curves obtained for (a) the eight horizontally and (b) eight vertically oriented specimens.

5.3.2.2 Mechanical Characterization

Mechanical characterization was based on the analysis of engineering stress-strain curves obtained from the static tensile tests. The same data-processing strategy adopted for the SLA specimens was applied here, ensuring a repeatable and technology-independent procedure. This includes the extraction of mechanical indicators through an analysis framework, allowing the method to be reproducible and applicable to different 3D-printing technologies.

5.3.2.2.1 Young's Modulus

Based on the data recorded during the tests, stress-strain curves up to break were obtained for both series of specimens: the eight specimens printed with a vertical orientation and the eight specimens printed with a horizontal orientation. The analysis was carried out up to the ultimate

load values recorded during the tests. For each class of specimen, with the same recorded strain values, those corresponding to the strain of the first recorded failure were taken as reference values for the ultimate tensile strength (UTS).

In line with the procedure adopted for SLA specimens, the estimation of the Young's modulus for the two specimen classes taking into account the repeatability of the test, an average curve was assessed by considering the eight individual stress-strain curves at the same strain values. The dispersion of stress values was quantified as standard deviation.

A weighted linear regression [18], taking into account the dispersion of the stress values given by recording for each sample, was used to approximate the trend of the mean curve with linear segments. From these linear trends, Young's modulus was estimated as the slope of the respective linear segments, considering its uncertainty. Specifically, based on the m-degree polynomial that best fits the stress-strain curve for each class, n linear segments were identified. From these segments, n values of the elastic modulus (E_i with $i = 1, \ldots, n$) were obtained in relation to the percentage strain level.

5.3.2.3 Measurement Uncertainty Analysis

The uncertainty analysis for the PolyJet tensile tests followed the same principles described for the SLA specimens in Subchapter 5.3.1.3. Uncertainty contributions arising from specimen geometry, load measurement, displacement and strain estimation were first evaluated individually using the same procedures outlined previously. These contributions were then propagated to estimate the uncertainty of the Young's modulus.

5.3.2.3.1 Young's Modulus

The measurement uncertainty of Young's modulus was estimated using the uncertainty propagation law, considering both the contribution due to repeatability, which affects the estimated slope, and the relative uncertainty of the measured quantities. From the expression of the linear elastic modulus, given by the ratio of stress to strain, this latter uncertainty contribution was estimated as follows:

$$\left(\frac{\sigma_E}{E}\right)^2 = \left(\frac{\sigma_L}{L}\right)^2 + \left(\frac{\sigma_d}{D}\right)^2 + \left(\frac{\sigma_l}{l}\right)^2 + \left(\frac{\sigma_w}{w}\right)^2 + \left(\frac{\sigma_t}{t}\right)^2 \quad (4)$$

The following sources of uncertainty (σ) were considered: the specimen dimensions (l = length, w = width and t = thickness), based on the accuracy on size of the 3D printer (± 0.2 mm); the load (L) and displacement (D) uncertainties, as specified by the test machine manufacturer in Table 5.3.

References

[1] A. Diniţă, A. Neacşa, A. I. Portoacă, M. Tănase, C. N. Ilinca, and I. N. Ramadan, "Additive Manufacturing Post-Processing Treatments, a Review with Emphasis on Mechanical Characteristics," *Materials*, vol. 16, no. 13, p. 4610, June 2023, doi: 10.3390/ma16134610.

[2] L. Jaksa *et al.*, "3D-Printed multi-material liver model with simultaneous mechanical and radiological tissue-mimicking features for improved realism," *Int. J. Bioprinting*, vol. 9, no. 4, p. 721, doi: https://doi.org/10.18063/ijb.721.

[3] E. O. Bachtiar *et al.*, "3D printing and characterization of a soft and biostable elastomer with high flexibility and strength for biomedical applications," *J. Mech. Behav. Biomed. Mater.*, vol. 104, p. 103649, Apr. 2020, doi: 10.1016/j.jmbbm.2020.103649.

[4] M. Cecchitelli *et al.*, "Mechanical Properties of Soft Materials in 3D Printing: A Preliminary Quality Assessment," in *2025 IEEE International Workshop on Metrology for Industry 4.0 & IoT (MetroInd4.0 & IoT)*, Castelldefels, Barcelona: IEEE, pp. 106–110.

[5] M. Wikło, B. H. Byczuk, and K. Skrzek, "Mechanical Characterization of FDM 3D-Printed Components Using Advanced Measurement and Modeling Techniques," *Materials*, vol. 18, no. 5, p. 1086, Feb. 2025, doi: 10.3390/ma18051086.

[6] H. Sadaghian, B. Dadmand, M. Pourbaba, S. Jabbari, and J. H. Yeon, "The Effect of Size on the Mechanical Properties of 3D-Printed Polymers," *Sustainability*, vol. 16, no. 1, p. 356, Dec. 2023, doi: 10.3390/su16010356.

[7] A. Rodríguez-Panes, J. Claver, and A. M. Camacho, "The Influence of Manufacturing Parameters on the Mechanical Behaviour of PLA and ABS Pieces Manufactured by FDM: A Comparative Analysis," *Materials*, vol. 11, no. 8, p. 1333, Aug. 2018, doi: 10.3390/ma11081333.

[8] C. Phillips, M. Kortschot, and F. Azhari, "Towards standardizing the preparation of test specimens made with material extrusion: Review of current techniques for tensile testing," *Addit. Manuf.*, vol. 58, p. 103050, Oct. 2022, doi: 10.1016/j.addma.2022.103050.

[9] S. Leng *et al.*, "Anatomic modeling using 3D printing: quality assurance and optimization," *3D Print. Med.*, vol. 3, no. 1, p. 6, Mar. 2017, doi: 10.1186/s41205-017-0014-3.

[10] *Prosthetics—Structural Testing of Lower-Limb Prostheses—Requirements and Test Methods*, ISO 10328:2016, June 2016.

[11] F. Górski, R. Wichniarek, W. Kuczko, and M. Żukowska, "Study on Properties of Automatically Designed 3D-Printed Customized Prosthetic Sockets," *Materials*, vol. 14, no. 18, p. 5240, Sept. 2021, doi: 10.3390/ma14185240.

[12] K. Łukaszewski, R. Raj, and A. Karwasz, "Mechanical Evaluation of PET-G 3D-Printed Wrist-Hand Orthosis: An Integrated Experimental and Numerical Approach," *Materials*, vol. 16, no. 18, p. 6132, Sept. 2023, doi: 10.3390/ma16186132.

[13] L. Ling, T. Lai, and R. Malyala, "Mechanical Properties and Degree of Conversion of a Novel 3D-Printing Model Resin," *Polymers*, vol. 16, no. 24, p. 3562, Dec. 2024, doi: 10.3390/polym16243562.

[14] M. Majdak, S. Bogović, M. Somogyi Škoc, and I. Rezić Meštrović, "Assessment of the Mechanical Properties and Fragment Characteristics of a 3D-Printed Forearm Orthosis," *Polymers*, vol. 16, no. 23, p. 3349, Nov. 2024, doi: 10.3390/polym16233349.

[15] J. F. Henriques, L. Gonçalves, A. M. Amaro, and A. P. Piedade, "3D printed polymers that mimic the mechanical properties of atherosclerotic blood vessels for training models: the advantageous degradation induced by UV radiation and hydrolysis," *3D Print. Med.*, vol. 11, no. 1, p. 34, July 2025, doi: 10.1186/s41205-025-00288-5.

[16] A. Pérez Jiménez, C. Sánchez González, S. Pérez Teresí, N. Landa, C. Díaz Jiménez, and M. Malvé, "Influence of Material Selection on the Mechanical Properties of 3D-Printed Tracheal Stents for Surgical Applications," *Polymers*, vol. 17, no. 16, p. 2223, Aug. 2025, doi: 10.3390/polym17162223.

[17] D. Kulker *et al.*, "Physico-mechanical characterization of 3D-printed PLGA for patient-specific resorbable implants in craniofacial surgery," *Sci. Rep.*, vol. 15, no. 1, p. 22225, July 2025, doi: 10.1038/s41598-025-07617-y.

[18] J. R. Taylor, "Error analysis," *Univ Sci. Books Sausalito Calif.*, vol. 20, 1997.

[19] W. C. Navidi, *Statistics for engineers and scientists*. McGraw-Hill Education, 2019.

[20] F. Safshekan, M. Tafazzoli-Shadpour, M. Abdouss, M. B. Shadmehr, and F. Ghorbani, "Investigation of the mechanical properties of the human tracheal cartilage," *Tanaffos*, vol. 16, no. 2, p. 107, 2017.

[21] M. Eskandari, A. L. Arvayo, and M. E. Levenston, "Mechanical properties of the airway tree: heterogeneous and anisotropic pseudoelastic and viscoelastic tissue responses," *J. Appl. Physiol.*, vol. 125, no. 3, pp. 878–888, Sept. 2018, doi: 10.1152/japplphysiol.00090.2018.

[22] M. P. Bonkile, A. Awasthi, C. Lakshmi, V. Mukundan, and V. S. Aswin, "A systematic literature review of Burgers' equation with recent advances," *Pramana*, vol. 90, no. 6, p. 69, June 2018, doi: 10.1007/s12043-018-1559-4.

[23] P. Chen, "CREEP RESPONSE OF A GENERALIZED MAXWELL MODEL".

[24] W. N. Findley, J. S. Lai, and K. Onaran, Eds., *Creep and relaxation of nonlinear viscoelastic materials: with an introduction to linear viscoelasticity*. in Dover books on engineering. New York: Dover, 2010.

[25] International Organization for Standardization, *Uncertainty of measurement-Part 3: Guide to the expression of uncertainty in measurement (GUM: 1995)*. ISO, 2008.

[26] "Evaluation of measurement data — Supplement 1 to the 'Guide to the expression of uncertainty in measurement' — Propagation of distributions using a Monte Carlo method." Accessed: Feb. 25, 2025. [Online]. Available: https://www.bipm.org/doi/10.59161/JCGM101-2008

[27] "AGS-X Universal Testing Machine | Affordable Material Testing." Accessed: Apr. 09, 2025. [Online]. Available: https://shimadzu-testing.com/en/products/universal-testing-machines/ags-x/

Chapter 6

Results and Discussion

6.1 Overview of Experimental Results

This chapter presents the results obtained by applying the dimensional and mechanical assessment methods introduced in Chapter 4 and Chapter 5 to the anatomical models and test specimens produced within the experimental workflow described in Chapter 3. The purpose of this chapter is to provide a structured and coherent presentation of the outcomes, enabling a comparative interpretation of the different case studies within a unified quality control (QC) perspective.

The aim is to quantify the geometric accuracy, printing repeatability, and mechanical behavior of SLA and PolyJet printed parts in order to evaluate the reliability of the proposed PoC 3D printing workflow. The reported results are grouped according to the type of assessment performed and the anatomical or test geometry considered.

Dimensional results refer to anatomical bone models, for which image-based assessment techniques were applied. In particular, two-dimensional slice-based measurements of cranial models and three-dimensional volumetric evaluations of clavicle models are presented, highlighting repeatability, measurement uncertainty and process-induced variability. On this basis, the results are further used to identify preliminary quantitative acceptance thresholds that may support quality evaluation of the printed models within a PoC workflow.

Mechanical results are focused on soft materials and specimens specifically designed for mechanical characterization. These include standardized and anatomically derived specimens produced by stereolithography and PolyJet technologies. The outcomes of static, dynamic and creep tests are reported in terms of elastic and viscoelastic properties, together with the associated measurement uncertainty, and are quantitatively compared with reference values reported for real biological tissues in order to assess the suitability of the printed materials for clinical simulation and training applications.

Overall, this chapter provides an integrated view of the experimental evidence generated in this doctoral work, showing how the results obtained, together with their associated uncertainty estimates, support the applicability and suitability of the proposed dimensional and mechanical

assessment methods for point-of-care 3D printing QC workflows. In addition, the analysis allows the identification of preliminary acceptance thresholds that may be used to evaluate the suitability of the printed models for clinical use, in line with the objectives pursued throughout this doctoral study.

6.2 Two-Dimensional Assessment Results

This subchapter presents the results obtained from the application of the proposed dimensional assessment methodology to anatomical 3D printing bone models. The analysis focuses on cranial models manufactured using Fused Deposition Modeling (FDM) and evaluated through image-based measurement techniques applied to Computed Tomography (CT) data.

The two-dimensional assessment is aimed at quantifying geometric accuracy and printing repeatability, as well as the variability introduced by the image-based measurement procedure, including slice selection and segmentation effects. Particular attention is paid to the estimation of measurement uncertainty and to the interpretation of the observed variability in relation to both process and method uncertainty contributions.

The reported results provide a quantitative basis for discussing the reliability and limitations of slice-based dimensional measurements when applied to anatomically complex geometries. On this basis, the outcomes are subsequently used to derive preliminary considerations regarding dimensional acceptance at the two-dimensional level, within the context of PoC 3D printing workflows.

6.2.1 Cranial Models

This subchapter reports the dimensional assessment results obtained for the cranial case study, following the workflow described in 4.3.1. Two-Dimensional Assessment of Cranial Model. The objective is to quantify the dimensional congruence between a reference cranial model (Skull0) and its printed replicas by means of CT-based image analysis.

As detailed in 4.3.1.1 CT Slice-Based Linear Measurements, the assessment is performed on the CT slice corresponding to the maximum outer diameter of each cranial model, automatically identified from the segmented mask. The comparison is based on four quantitative parameters: section area A, maximum longitudinal diameter D_{max}, and two local thicknesses S_1 and S_2 measured at the extremities of D_{max}.

The reported results are structured according to the anatomical plane adopted for the evaluation, consistently with 4.3.1.2 Transverse Plane Dimensional Assessment and 4.3.1.3 Coronal Plane Dimensional Assessment. Measurement uncertainty considerations and their interpretation in relation to the observed variability are discussed in line 4.3.1.4 Image Analysis, Thresholding and Uncertainty Contributions.

6.2.1.1 Transverse Plane Results

Quantitative results for the reference model (Skull0) and its replicas (Rep1 to Rep8) in the transverse plane are summarized in following tables. Table 6.1 shows the dimensional results for each skull at the slice with the maximum longitudinal diameter. Conversely, Table 6.2 presents the results of comparing each skull with Skull0 in terms of percentage discrepancy ($\Delta_{i,0}$). This value represents the relative differences between the *i*-th skull and Skull0, where i = 1, 2, …, 8. The results are expressed as mean ± standard deviation (SD).

Table 6.1. Dimensional measurements on the model mask in the transverse plane (mean ± SD).

3D printed model	A (mm^2)	D_{max} (mm)	S_1 (mm)	S_2 (mm)
Skull0	2054 ± 12	101.1 ± 0.2	4.1 ± 0.2	3.9 ± 0.2
Rep1	2192 ± 30	101.4 ± 0.2	4.0 ± 0.3	4.4 ± 0.3
Rep2	1900 ± 13	101.0 ± 0.2	4.2 ± 0.2	4.5 ± 0.2
Rep3	2206 ± 9	101.2 ± 0.3	4.3 ± 0.2	4.6 ± 0.2
Rep4	2089 ± 30	101.0 ± 0.2	4.4 ± 0.3	4.0 ± 0.3
Rep5	2111 ± 7	99.7 ± 0.3	4.5 ± 0.2	3.9 ± 0.2
Rep6	1876 ± 4	101.0 ± 0.4	4.1 ± 0.2	4.5 ± 0.2
Rep7	1971 ± 12	101.6 ± 0.2	4.2 ± 0.2	4.0 ± 0.2
Rep8	2176 ± 70	101.6 ± 0.2	3.9 ± 0.4	4.2 ± 0.2

Table 6.2. Differences of dimensional measurements between model masks (mean ± SD).

3D printed model	A (%)	D_{max} (%)	S_1 (%)	S_2 (%)
$\Delta_{1,0}$	3.63 ± 0.06	0.32 ± 0.01	6.7 ± 1.8	3.0 ± 0.9
$\Delta_{2,0}$	7.51 ± 0.07	0.05 ± 0.01	10.6 ± 1.9	9.0 ± 1.6
$\Delta_{3,0}$	7.37 ± 0.05	0.22 ± 0.01	11.5 ± 2.7	11.4 ± 2.3
$\Delta_{4,0}$	1.68 ± 0.03	0.13 ± 0.01	3.5 ± 1.1	14 ± 4
$\Delta_{5,0}$	2.75 ± 0.02	1.38 ± 0.01	6.2 ± 1.4	17 ± 3
$\Delta_{6,0}$	8.67 ± 0.05	0.26 ± 0.01	8.9 ± 2.2	6.5 ± 1.5
$\Delta_{7,0}$	4.07 ± 0.03	0.56 ± 0.01	2.2 ± 0.4	9.1 ± 2.3
$\Delta_{8,0}$	5.93 ± 0.19	0.56 ± 0.01	3.3 ± 1.3	0.3 ± 0.1

A general observation from the dimensional measurements, excluding area values, revealed that pixel resolution is the primary source of uncertainty. In fact, the standard deviation associated with the image analysis procedure is usually significantly lower (about an order of magnitude) than that attributed to pixel size, except for some specific cases discussed below. In particular, for D_{max} of Rep6 and S_1 for Rep8 the contributions of pixel resolution and image analysis uncertainty appear comparable.

While considering additional error sources, the variation in average parameter values seems to be justified by the variability inherent in the printing process and the limitations of the whole technological process, starting from the slicing phase of the 3D digital model. Indeed, the percentage error between the reference model and its replicas increases as the level of detail in the object intensifies. The maximum discrepancy observed in the macroscopic parameter (D_{max}) is approximately 1%, while an error exceeding 15% is obtained for the two thicknesses.

In addition, the variability found in S_1 and S_2 thicknesses is consistent with the uncertainty arising from the printing process. The printer nozzle has a diameter of 0.4 mm, and depending on the number of layers deposited, there is a variability multiple of 0.4 mm in the mean thickness value. The Δ values, expressed as the percentage difference between the thickness compared, indicate the extent to which the printer deposited more or fewer layers in the section under consideration. This is reflected in the percentage error between the thickness of the reference model and its replicas (Table 6.2): the relative uncertainty associated with the discrepancies is about one percentage point.

Despite the attempt to quantify errors due to model placement within the CT, the spread of results in terms of both mean value and standard deviation obtained for the areas suggests that the section with the maximum longitudinal diameter may differ between Skull0 and its replicas. Area measurements diverge in the slice range in which the anatomical geometry of the orbits and sinuses varies, leading to variability in the cross-sectional area value. However, the maximum diameter and thicknesses remain consistent. This is likely due to the repeatability of skull positioning during CT data acquisition. In regions where skull morphology varies rapidly across adjacent slices, small shifts in the identified maximum-diameter slice can lead to significant changes in the measured area, even when the corresponding diameter remains nearly constant.

For these reasons, a complementary analysis in the coronal plane was carried out, together with repeated positioning of the reference model during CT acquisition, in order to further investigate the influence of specimen alignment and slice identification on the observed variability and to distinguish positioning-related effects from process- and measurement-induced contributions.

6.2.1.2 Coronal Plane Results

The coronal plane analysis was introduced to further investigate the sources of dimensional variability observed in the transverse plane results, with particular attention to the effects of specimen positioning and slice identification during CT acquisition.

Quantitative results obtained in the coronal plane for the reference cranial model (Skull0) and its replicas (Rep1 to Rep8) are summarized in Table 6.3, where the dimensional parameters A, D_{max}, S_1 and S_2 are reported as mean ± standard deviation (SD). The corresponding dimensional discrepancies with respect to the reference model, expressed as percentage differences $\Delta_{i,0}$, are reported in Table 6.4.

Table 6.3. Dimensional measurements on the model mask in the coronal plane (mean ± SD).

3D printed model	A (mm^2)	D_{max} (mm)	S_1 (mm)	S_2 (mm)
Skull0	1252 ± 2	100.7 ± 0.3	3.1 ± 0.2	3.1 ± 0.4
Rep1	1558 ± 6	101.2 ± 0.3	3.8 ± 0.2	4.3 ± 0.3
Rep2	1456 ± 6	101.3 ± 0.5	4.4 ± 0.2	4.0 ± 0.4
Rep3	1543 ± 4	101.5 ± 0.3	4.1 ± 0.2	4.4 ± 0.2
Rep4	1442 ± 4	101.0 ± 0.4	4.1 ± 0.2	3.8 ± 0.4
Rep5	1433 ± 2	99.8 ± 0.7	4.8 ± 0.2	3.8 ± 0.2
Rep6	1461 ± 13	101.2 ± 0.5	4.3 ± 0.3	3.9 ± 0.3
Rep7	1577 ± 7	101.5 ± 0.4	4.4 ± 0.2	4.0 ± 0.2
Rep8	1457 ± 9	101.5 ± 0.5	3.8 ± 0.2	3.8 ± 0.3

Table 6.4. Differences of dimensional measurements between model masks in the coronal plane (mean ± SD).

3D printed model	A (%)	D_{max} (%)	S_1 (%)	S_2 (%)
$\Delta_{1,0}$	24.5 ± 0.1	0.532 ± 0.002	22 ± 4	41 ± 14
$\Delta_{2,0}$	16.3 ± 0.1	0.678 ± 0.004	44 ± 9	35 ± 13
$\Delta_{3,0}$	23.2 ± 0.1	0.799 ± 0.003	33 ± 6	46 ± 9
$\Delta_{4,0}$	15.2 ± 0.1	0.435 ± 0.002	33 ± 6	26 ± 9
$\Delta_{5,0}$	14.5 ± 0.1	0.967 ± 0.009	56 ± 10	24 ± 4
$\Delta_{6,0}$	16.7 ± 0.2	0.592 ± 0.004	41 ± 12	30 ± 8
$\Delta_{7,0}$	26.0 ± 0.2	0.795 ± 0.004	45 ± 8	32 ± 7
$\Delta_{8,0}$	16.4 ± 0.1	0.809 ± 0.005	22 ± 4	26 ± 7

Similarly to what observed in the transverse plane assessment, the analysis of uncertainty contributions shows that pixel resolution and method related uncertainty are generally comparable for macroscopic parameters, while pixel resolution represents the dominant contribution for detailed measurements. In particular, thickness measurements S_1 and S_2 are mainly affected by pixel resolution uncertainty, whereas method uncertainty contributions become more relevant for global parameters such as section area A and maximum longitudinal diameter D_{max}. This behaviour is consistent with the trends already highlighted in the transverse plane results.

As a first observation, the mean values of the dimensional parameters measured on the reference model (Table 6.3) tend to be systematically lower than those obtained for its replicas. This discrepancy is also reflected in the percentage differences (Table 6.4), where area discrepancies reach values up to approximately 26%, and differences exceeding 50% are observed for local thickness measurements. In contrast, the mean values measured across the replicas are generally compatible with each other.

This behavior may be partially attributed to the finer layer thickness used for printing the reference model compared to the replicas. However, it should be noted that the entire workflow, starting from the segmentation of the original CT images and including the generation of eight independent STL files, was repeated for the replicas. As a result, the higher mean values observed for the replicas can reasonably be attributed to the cumulative propagation of variability associated with both the printing process and the image segmentation procedure.

With respect to the influence of printing orientation, it should be noted that CT acquisitions were performed perpendicular to the printing direction. Specifically, skull models were printed along the transverse plane, while CT scans were acquired along the coronal plane. Under these conditions, the variability observed in thickness measurements cannot be directly attributed to layer stacking effects. In particular, the minimum discrepancies of approximately 22% observed for thicknesses in Table 6.4 are more plausibly related to local anatomical geometry rather than to variability in the number of layers deposited during printing.

A specific consideration concerns the results obtained for the maximum longitudinal diameter D_{max}. The values for the eight replicas are highly consistent (Table 6.3), with corresponding percentage differences remaining below 1% (Table 6.4). This confirms the behavior already observed in the transverse plane assessment and indicates that D_{max} represents a particularly robust dimensional descriptor for the cranial case study. The limited variability of this parameter suggests that the longitudinal diameter remains relatively constant across a wide portion of the parietal region of the skull. This observation further implies that the slice corresponding to the maximum longitudinal diameter may not be unique, even for the same skull model. To investigate this aspect, additional measurements were carried out by repeating the manual positioning of the reference model (Pos1 to Pos6) within the CT gantry six times. The resulting dimensional measurements are reported in Table 6.5, expressed as mean ± SD for the same set of parameters.

Table 6.5. Dimensional measurements (mean ± SD) by repeating the positioning of the reference skull model.

3D printed model	A (mm^2)	D_{max} (mm)	S_1 (mm)	S_2 (mm)
Pos1	1252 ± 2	100.7 ± 0.3	3.1 ± 0.2	3.1 ± 0.4
Pos2	1199 ± 15	100.7 ± 0.5	3.5 ± 0.4	3.2 ± 0.4
Pos3	1172 ± 5	101.2 ± 0.2	3.4 ± 0.2	2.9 ± 0.2
Pos4	1176 ± 2	100.7 ± 0.5	3.6 ± 0.2	3.1 ± 0.2
Pos5	1270 ± 2	100.9 ± 0.2	3.4 ± 0.2	3.4 ± 0.2
Pos6	1176 ± 10	100.9 ± 0.4	3.2 ± 0.2	2.7 ± 0.2

The positioning analysis shows that repeated placement of the same specimen primarily affects section area measurements. A noticeable dispersion in area values is observed across repeated acquisitions, despite the absence of any manufacturing-related variability. This confirms that area

measurements are particularly sensitive to slice identification in anatomical regions where skull geometry varies rapidly across adjacent slices, such as the orbital and paranasal sinus regions.
In contrast, the maximum longitudinal diameter D_{max} remains highly stable under repeated positioning conditions, with standard deviations comparable to those observed in the transverse-plane analysis of the printed replicas. This result indicates that D_{max} is weakly affected by specimen alignment and slice misidentification. Local thickness measurements S_1 and S_2 show intermediate behaviour: while some dispersion is observed, the magnitude of variability remains significantly lower than that measured between the reference model and its replicas. This confirms that the thickness variability observed in the transverse plane results cannot be attributed solely to positioning effects but rather reflects the combined influence of printing process limitations and measurement resolution.

From a metrological perspective, these findings are consistent with the uncertainty analysis discussed in Subchapter 4.3.1.4. Pixel resolution represents the dominant source of uncertainty for fine measurements, whereas method uncertainty contributions, such as slice selection and thresholding for automatic segmentation, play a more relevant role for area parameters. The coronal plane assessment therefore provides experimental evidence that positioning related effects contribute to the dimensional discrepancies observed in the transverse plane results.

6.2.2 Implications for 2D Acceptance Thresholds

The dimensional results obtained for cranial models provide useful indications for the identification of preliminary acceptance criteria within a PoC QC framework, while simultaneously highlighting the limitations of a two-dimensional, slice-based assessment.

Among the investigated parameters, the maximum longitudinal diameter consistently exhibits the lowest variability across replicas, with percentage differences remaining below approximately 1% and limited sensitivity to slice identification and specimen positioning. This indicates that a percentage deviation of this order of magnitude may be considered as a reference for preliminary dimensional acceptance in PoC contexts.
The results indicate that the observed variability cannot be attributed solely to manufacturing inaccuracies but arises from the cumulative effect of the entire digital workflow, including imaging, segmentation and measurement. Consequently, defining a single acceptance threshold applicable to all dimensional descriptors and anatomical regions is not feasible within the scope of the present case study: section area and local thickness measurements show significantly higher variability. The

strong dependence of these parameters on local geometry limits their suitability for defining strict acceptance thresholds.

These findings highlight the need to complement two-dimensional assessments with three-dimensional volumetric analyses capable of capturing global geometric deviations in a more comprehensive manner. This consideration directly motivates the extension of the dimensional investigation to volumetric assessment techniques and to additional anatomical models, as discussed in the following subchapter dedicated to the clavicle case study.

6.3 Three-Dimensional Assessment Results

This subchapter presents the results of the three-dimensional dimensional assessment carried out on anatomical bone models, with the objective of extending the investigation beyond slice-based measurements and addressing the limitations identified in the two-dimensional analysis.

The three-dimensional assessment focuses on clavicle models produced by FDM and evaluated through CT-based volumetric measurement techniques. In contrast to the cranial case study, the clavicle geometry allows the use of global volumetric descriptors, enabling a more direct interpretation of geometric variability and printing repeatability at the object level.

In addition, this subchapter includes a direct comparison between volumetric measurements obtained from a diagnostic CT system and those derived from an industrial metrological CT system. This comparison is intended to investigate the suitability of imaging tools commonly available in hospital environments for quality control purposes, and to assess whether diagnostic CT can provide sufficiently reliable information for three-dimensional quality evaluation in PoC workflows.

The reported results are discussed in terms of repeatability, measurement uncertainty and process-induced variability, and provide the basis for the definition of preliminary three-dimensional acceptance considerations, which are addressed in the conclusion of this subchapter.

6.3.1 Clavicle Models

This subchapter reports the three-dimensional dimensional assessment results obtained for the clavicle case study, following the workflow described in 4.3.2 Three-Dimensional Assessment of Clavicle Model. The objective is to quantify the geometric consistency and volumetric repeatability of FDM printed clavicle models by means of CT-based volumetric analysis.

As detailed in 4.3.2.1 Volumetric Assessment Techniques: Diagnostic CT and 4.3.2.2 Volumetric Assessment Techniques: Industrial CT, the assessment is based on the reconstruction of three-dimensional volumetric data derived from CT data and on the subsequent estimation of the total model volume. Unlike the cranial case study, where the analysis relied on slice-based linear descriptors, the clavicle assessment adopts global volumetric parameters in order to capture overall geometric deviations at the object level.

The comparison is performed across multiple printed replicas of the same digital model, allowing the investigation of printing repeatability under controlled manufacturing conditions. In addition, volumetric measurements obtained from a diagnostic CT system and from an industrial metrological CT system are analyzed in parallel, enabling a direct comparison between different CT-based measurement approaches.

The reported results are structured according to the imaging technique adopted for the volumetric evaluation, consistently with the methodological framework introduced in 4.3.2 Three-Dimensional Assessment of Clavicle Model. Measurement uncertainty contributions and their interpretation in relation to process-induced variability are discussed in line with the uncertainty considerations presented for the three-dimensional assessment, providing a quantitative basis for the definition of preliminary acceptance considerations based on volumetric descriptors.

6.3.1.1 Volumetric Assessment Results

Six clavicle replicas were produced by FDM using a single G-code file, in order to minimize variability related to slicing, support generation and print orientation. This approach allowed the investigation to focus on variability introduced by the printing process itself rather than by operator-dependent digital preparation steps.

Volumetric measurements were carried out using two CT-based imaging techniques: a diagnostic CT system (CT-D), representative of equipment commonly available at the point of care, and an industrial CT system (CT-I), designed for high-precision metrological applications. The two methods were applied independently to all replicas, and the corresponding volumetric results are reported in Table 6.6, expressed as mean ± standard deviation (SD).

Table 6.6. Volume outcomes (mean ± SD) and maximum percentage discrepancy of the 3D printed clavicle replicas for Diagnostic CT scan (CT-D) and Industrial CT scan (CT-I)

Imagine Technique	Volume (cm^3)						Maximum Discrepancy (%)	Combined Volume (cm^3)
	Rep1	Rep2	Rep3	Rep4	Rep5	Rep6		
CT-D	15.0 ± 0.7	15.1 ± 0.7	14.9 ± 0.7	14.9 ± 0.7	14.8 ± 0.7	14.9 ± 0.7	1.8	14.9 ± 0.7
CT-I	14.88 ± 0.09	14.78 ± 0.09	14.86 ± 0.09	14.91 ± 0.09	14.84 ± 0.09	14.85 ± 0.09	0.8	14.8 ± 0.1

For the diagnostic CT measurements, the overall uncertainty in volume estimation is governed by a comparable contribution of pixel resolution, slice thickness and image processing uncertainty. In contrast, the industrial CT measurements exhibit significantly lower dispersion, with uncertainties reduced by approximately one order of magnitude. This difference reflects the higher spatial resolution and metrological stability of the CT-I system.

Despite the difference in absolute uncertainty levels, both CT-based methods provide consistent volume estimates across the six replicas. The maximum volumetric discrepancy observed among the replicas remains below 2% for both techniques, indicating a high degree of repeatability of the printing process under intensive and rapid manufacturing conditions.

6.3.1.2 Comparison between Diagnostic CT and Industrial CT

A direct comparison between CT-D and CT-I measurements was performed by assuming the industrial CT results as the reference for volumetric accuracy. The comparison shows a mean absolute percentage error (MAPE) of approximately 0.65% between the two techniques, with combined average volumes differing by less than 0.1 cm^3.

These results demonstrate that, while CT-D measurements are characterized by higher uncertainty, they remain compatible with CT-I outcomes in terms of mean volumetric values. This finding is particularly relevant for PoC applications, where access to industrial CT systems is limited and diagnostic CT represents the most practical imaging option for QC purposes.

The analysis further highlights that repeatability-related uncertainty can be clearly distinguished in the CT-I measurements, whereas it is masked by the higher overall uncertainty of the CT-D measurements. Nevertheless, the agreement between the two methods supports the use of

diagnostic CT as a feasible tool for volumetric quality assessment in clinical environments, provided that its limitations are properly accounted for.

6.3.2 Implications for 3D Acceptance Threshold

The volumetric results obtained for the clavicle replicas provide a complementary perspective to the cranial model analysis and allow the identification of indicative acceptance ranges based on three-dimensional descriptors.

The maximum volumetric discrepancy observed among the replicas does not exceed 2%, even under printing conditions representative of intensive PoC use. This finding suggests that volumetric deviations exceeding this value may indicate anomalies in the printing process, such as printer miscalibration, material inconsistencies or environmental effects, and may therefore require further inspection or corrective actions.

Unlike local thickness or area measurements in the cranial case study, volumetric assessment integrates deviations over the entire geometry, reducing sensitivity to local anatomical complexity and slice selection effects. As a result, volumetric descriptors appear more suitable for defining preliminary acceptance criteria when global geometric fidelity is of interest.

Overall, the clavicle case study demonstrates that three-dimensional volumetric assessment can effectively complement two-dimensional analyses, providing a more robust basis for quality control in PoC 3D printing workflows.

6.3 Mechanical Assessment Results

This subchapter presents the results obtained from the mechanical assessment campaigns carried out on soft 3D printed specimens, following the methodologies described in Chapter 5. Beyond material characterization, the objective of the mechanical investigation is to propose testing methods applicable to PoC environments and to explore their potential use as verification procedures for the mechanical suitability of soft 3D printed anatomical models. The results are therefore interpreted not only in terms of elastic and viscoelastic behavior but also with respect to their relevance for defining preliminary acceptance thresholds tailored to different clinical simulation and training applications.

The mechanical results are organized by experimental campaign. First, stereolithography (SLA) printed specimens are analyzed as the main case study, providing a comprehensive characterization under static, dynamic and creep loading and supporting the development of a repeatable mechanical verification approach. PolyJet specimens are then introduced as a complementary and preliminary investigation, aimed at examining aspects not addressed in the SLA campaign, particularly the effect of build orientation, and at exploring the mechanical response of a recently adopted AM technology. These initial findings are intended to inform future studies on anatomically complex and multi-material printed models, where PolyJet systems are increasingly employed.

6.3.1 Mechanical Assessment of SLA Printed Specimens Results

This subchapter reports the mechanical assessment results obtained for SLA printed specimens, following the experimental workflow described in 5.3.1 Mechanical Assessment of SLA Printed Specimens. The objective is to evaluate the mechanical response of soft SLA printed materials through a verification approach, considering both standardized and anatomically derived specimen geometries.

As detailed in 5.3.1.1 Testing Machine, mechanical tests were conducted under controlled laboratory conditions and included static tensile tests, dynamic mechanical analysis and creep tests. The assessment focuses on the estimation of elastic and viscoelastic properties and on the evaluation of the repeatability of the proposed testing procedures when applied to geometries relevant for PoC applications.

The reported results are organized according to the type of mechanical test performed, consistently with 5.3.1.1.1 Static Test, 5.3.1.1.2 Dynamic Test and 5.3.1.1.3 Creep Test. Measurement uncertainty and repeatability aspects are interpreted in line with the uncertainty analysis presented in 5.3.1.3 Measurement Uncertainty Analysis in order to support a metrologically discussion of mechanical suitability and preliminary acceptance considerations for soft anatomical models.

6.3.1.1 Static Tensile Test Results

Static tensile test results were obtained for SLA printed specimens following the procedures described in 5.3.1.1.1 Static Test. Tests were performed on standardized dog-bone specimens, cylindrical specimens and anatomically derived trachea-shaped specimens, with the aim of evaluating the elastic response of the material and the influence of specimen geometry on the estimated mechanical properties.

From the load-displacement data recorded during the static tensile tests (Figure 5.3), stress–strain curves were obtained for all six specimens of each geometry (Figure 6.1).

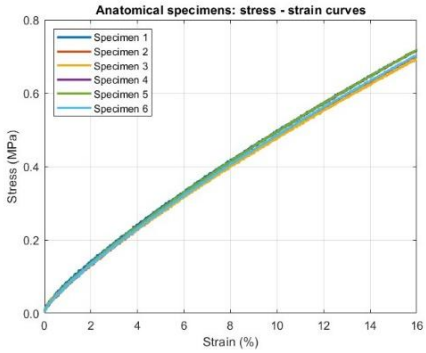

(a)

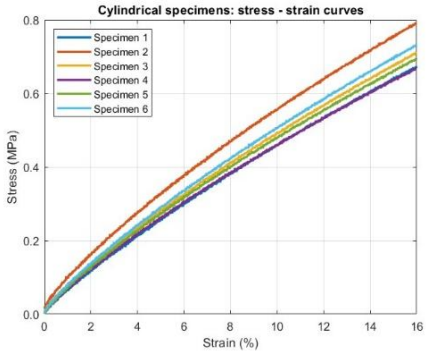

(b)

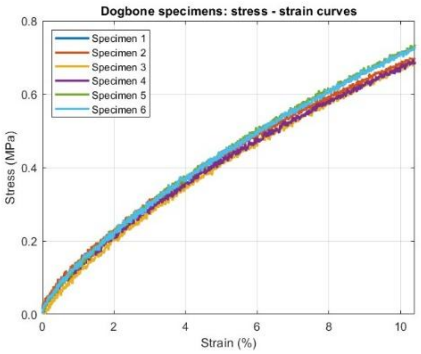

(c)

Figure 6.1. Stress-strain curves obtained from static tensile tests for the six specimens of each geometry: (a) anatomical; (b) cylindrical and (c) ISO 527-1A dog-bone shape.

To determine the Young's modulus, an average stress-strain curve was calculated for each geometry and approximated using a piecewise weighted linear regression. Starting from the third-degree polynomial that best fit the average stress-strain curve for each specimen type, three linear segments were identified. For the anatomical and cylindrical specimens, these corresponded to up to 2% strain, up to 10% and up to the maximum strain reached (16%). For the dog-bone specimens, the intervals were instead defined as up to 2%, up to 6% and up to the maximum strain reached (10.4%), due to their shorter deformation range compared to the other geometries (Figure 6.2). All linear segments exhibited a high correlation coefficient (r = 0.99), confirming the robustness of the fitting method.

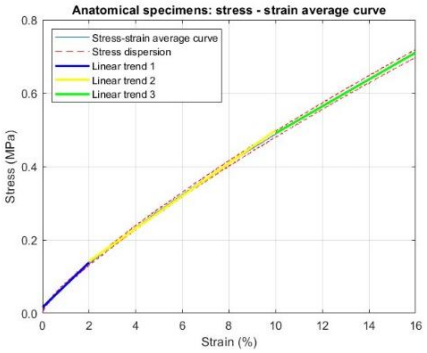

(a)

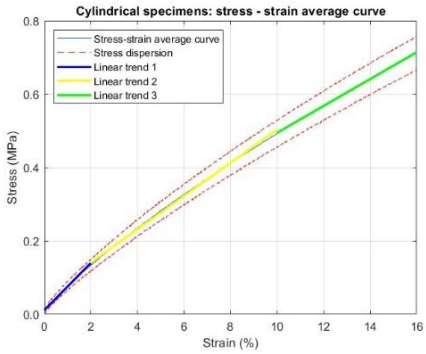

(b)

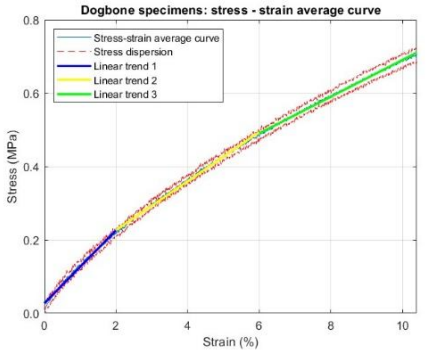

(c)

Figure 6.2. Average stress–strain curves with corresponding stress dispersion (dashed red lines) and piecewise weighted linear regressions used for Young's modulus estimation for specimen geometry: (a) anatomical; (b) cylindrical and (c) ISO 527-1A dog-bone shape.

The resulting values of stress and Young's modulus, reported as mean ± SD, are summarized in Table 6.7.

Table 6.7. Stress and Young's modulus values, expressed as mean ± standard deviation (SD), obtained for the three specimen geometries over specific strain intervals from static tensile tests.

Specimens	Strain	Stress (MPa)	E (MPa)
Anatomical	2%	0.134 ± 0.015	6.13 ± 0.25
	10%	0.487 ± 0.017	4.46 ± 0.10
	16%	0.707± 0.018	3.69 ± 0.08
Cylindrical	2%	0.13 ± 0.03	6.2 ± 0.3
	10%	0.47 ± 0.04	4.35 ± 0.12
	16%	0.68 ± 0.05	3.53 ± 0.13
Dog-bone	2%	0.215 ± 0.011	9.9 ± 0.4
	6%	0.482 ± 0.018	6.7 ± 0.20
	10.4 %	0.707 ± 0.025	5.0 ± 0.15

A progressive reduction in modulus with increasing strain was observed for all geometries, consistent with the non-linear elastic behavior typical of elastomeric materials. Among the tested geometries, dog-bone specimens showed the highest initial modulus (9.9 ± 0.4 MPa at 2% strain), while anatomical and cylindrical specimens displayed very similar values (6.13 ± 0.25 MPa and 6.2 ± 0.3 MPa at 2% strain, respectively). This increased stiffness appears to be due to their standardized length, shorter effective deformation range and compact rectangular cross-section, which differs from the hollow cylindrical cross-section of other geometries. Considering the average elastic modulus values, the mean absolute percentage error (MAPE) between the dog-bone and anatomical specimens, taking the latter as the reference, is 51.3%.

The comparison between the anatomical and cylindrical specimens shows that, for the same strain intervals, the elastic modulus values are very similar. The differences observed, 0.07 MPa at 2% strain, 0.11 MPa at 10%, and 0.16 MPa at 16%, are all smaller than or comparable to their measurement uncertainty, indicating that, under the present testing conditions, specimen geometry has only a marginal influence on the elastic response. This indicates that the observed stiffness is primarily governed by the intrinsic material properties rather than by geometric effects. These conclusions are further supported by a one-way ANOVA test. For anatomical versus cylindrical specimens, at all strain intervals, results $p \geq 0.05$, indicating no statistically significant effect of geometry. Because the dog-bone geometry was characterized over a more limited strain range, the ANOVA comparison including dog-bone specimens could be conducted only for the first interval

common to all three specimen types: in this case, results $p << 0.01$ demonstrating a statistically significant geometric effect.

When compared with the manufacturer datasheet values for Flexible 80A Resin (Table 6.8), the experimental stress values are substantially lower. This difference can be reasonably attributed to a combination of factors, including the specific geometry of the test samples, which differs from the standard sample geometry used in manufacturer testing, as well as the printing process parameters (orientation, print settings, post-processing), which can significantly affect the final mechanical properties of 3D printed parts.

Table 6.8. Mechanical properties of the material as reported in the datasheet (ASTM D 412-06).

Material	**Flexible 80A Resin**
Ultimate tensile strength	8.9 MPa
Stress at strain 50 %	3.1 MPa
Stress at strain 100 %	6.3 MPa

To provide a more relevant comparison, elastic modulus values for human tracheal tissue reported in the scientific literature were considered. Specifically, three studies performing experimental measurements on real tracheal tissues were analyzed, reporting mean Young's modulus values of 6.5 MPa [1], 4.4 MPa [2] and 3.3 MPa [3] (Table 6.9). As a first step, a global average Young's modulus was derived from the three linear segments of the anatomical shape specimens (Table 6.7) and then compared with the mean values found in the literature. The mechanical accuracy of the printed model was then quantified using the Mean Absolute Percentage Error (MAPE), which resulted in a value of 2%, indicating a good match between the mechanical response of the printed material and that of the reference biological tissue.

Table 6.9. Mean values of elastic moduli of real tracheas in the scientific literature

Authors	**Mean Young Modulus**
J. K. Rains, et al. [1]	6.5 MPa
R. K. Lambert, et al. [2]	4.4 MPa
O. Trabelsi, et al. [3]	3.3 MPa

Despite these geometry-dependent differences, the dispersion of Young's modulus values within each specimen group remains limited. The standard deviations are comparable across geometries and are consistent with the measurement uncertainty estimated in Subchapter 5.3.1.3. This indicates that the static tensile test protocol provides reproducible results when applied to both standardized and anatomical specimens.

Overall, the comparison between standardized and anatomical geometries highlights an important aspect for point-of-care quality control. While dog-bone specimens are suitable for material-level characterization, they tend to overestimate stiffness with respect to anatomically relevant geometries. Conversely, trachea-shaped specimens provide a mechanical response that more closely reflects the deformation conditions encountered in clinical simulation models. These findings support the inclusion of geometry-specific tensile testing when the objective is to verify the mechanical suitability of soft 3D printed anatomical models rather than to characterize the bulk material alone.

6.3.1.2 Dynamic Test Results

Dynamic Mechanical Analysis (DMA) results are presented following the procedures described in Section 5.3.1.1.2 Dynamic Test. The tests were conducted on cylindrical and anatomically derived trachea-shaped specimens in order to characterize the viscoelastic behavior of the SLA printed material under oscillatory loading conditions representative of clinical simulation and training scenarios.

6.3.1.2.1 Storage Modulus

The average trends of the storage modulus (E') for both anatomical and cylindrical specimens are shown in Figure 6.3.

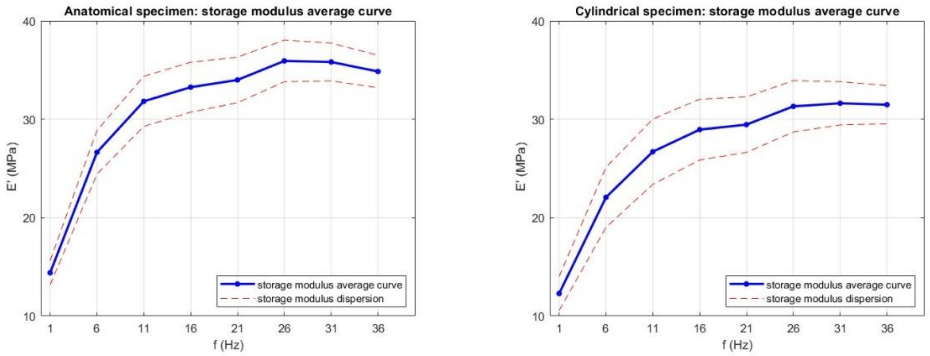

(a) (b)

Figure 6.3. Average storage modulus (E') as a function of frequency for (a) anatomical specimens and (b) cylindrical specimens. Data are presented as mean values with error bars representing the standard deviation across six replicates for each geometry.

The anatomical samples show an initial E' of 14.4 ± 1.2 MPa at 1 Hz, which increases to 33.3 ± 2.5 MPa at 16 Hz and then plateaus. Similarly, the cylindrical samples increase from 12.3 ± 1.7 MPa to 29 ± 3 MPa over the same frequency range. For both specimens, the storage modulus increased sharply from 1 Hz to approximately 16 Hz, indicating a pronounced stiffening of the material with frequency**,** after which the values plateaued or slightly decreased. This trend reflects the reduced time available for molecular rearrangements at higher loading rates, resulting in a more elastic-like response. Above 16 Hz, E' values plateaued, suggesting that the material had reached a stiffness regime that no longer varied with frequency. Anatomical specimens consistently exhibited higher E' values across the tested frequency range, reaching 35.9 ± 2.1 MPa at the maximum, compared to 31.6 ± 2.2 MPa for cylindrical specimens. The storage modulus exhibited a clear dependence on specimen geometry, with anatomical specimens consistently showing higher E' values across the entire frequency range compared to cylindrical specimens. This difference can be attributed to several factors. Firstly, the more complex geometry of the anatomical specimens likely enhances structural stiffness by distributing the applied load over regions with varying cross-sectional areas, resulting in a higher apparent elastic response. Secondly, the printing layer arrangement in the anatomical geometry may have promoted more favorable load-bearing paths, reducing the influence of local defects and improving elastic energy storage under dynamic loading. Since the storage modulus quantifies the material's capacity to store elastic energy during each cycle of deformation, the higher values observed for anatomical specimens point to an overall stiffer structural response, despite being made from the same material. In contrast, the cylindrical specimens, with their uniform cross-section, are more likely to develop a homogeneous stress field,

resulting in a lower apparent stiffness under dynamic loading. The dispersion in E' values was moderate, with greater variability in cylindrical specimens. This may be linked to their uniform geometry being more sensitive to slight misalignments or micro-slippage at the grips, which can disproportionately affect the measured stiffness. In contrast, the complex anatomy of the trachea specimens may provide additional geometric constraints that stabilize the load distribution during testing, thereby reducing variability. The effect of geometry is further supported by a one-way ANOVA test on the storage modulus E' at each frequency, with results shown in Figure 6.4; p-values were ≤ 0.03 at all frequencies, confirming that specimen geometry has a statistically significant influence.

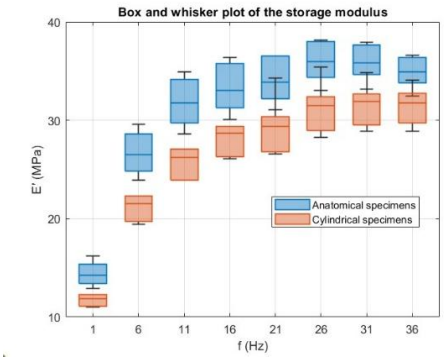

Figure 6.4. Box and whisker plots of the storage modulus E' (MPa) as a function of frequency f (Hz) for anatomical (blue) and cylindrical (orange) specimens. A one-way ANOVA test carried out at each frequency shows a significant effect of specimen geometry on E' ($p \leq 0.03$ at all frequencies), confirming the geometric influence on the specimen's response.

6.3.1.2.2 Loss Modulus

The corresponding trends for the loss modulus (E") are presented in Figure 6.5. The loss modulus exhibited a frequency-dependent trend closely mirroring that of the storage modulus. For both geometries, E" increased markedly between 1 Hz and approximately 16 Hz, indicating a rise in the material energy dissipation capability with increasing loading frequency. For anatomical specimens, E" rose from 9.6 ± 1.1 MPa at 1 Hz to 24.6 ± 1.4 MPa at 16 Hz, while cylindrical specimens increased from 7.5 ± 1.4 MPa to 20.4 ± 2.5 MPa over the same range. This initial growth reflects the reduced time for molecular rearrangements at higher excitation rates, which increases internal friction and, consequently, the viscous component of the viscoelastic response.

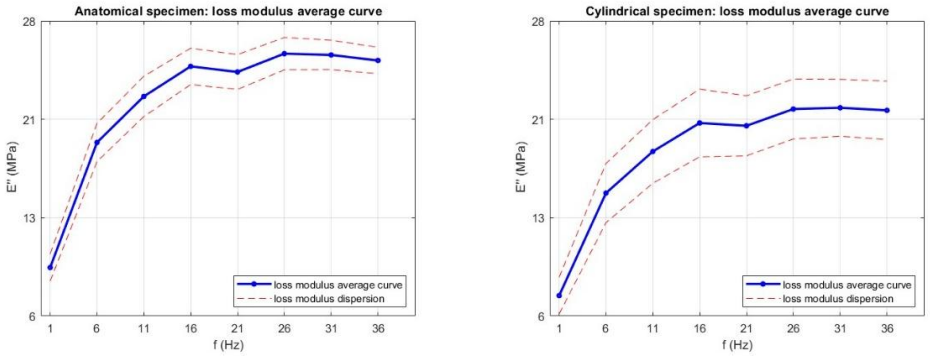

(a) (b)

Figure 6.5. Average loss modulus (E") as a function of frequency for (a) anatomical specimens and (b) cylindrical specimens. Data are presented as mean values with error bars representing the standard deviation across six replicates for each geometry.

Beyond 16 Hz, the loss modulus values approached a plateau, consistent with the behavior of many elastomeric materials, where further increases in frequency produce minimal changes in viscous damping. The slightly higher loss modulus observed for the anatomical geometry suggests a greater capacity for energy dissipation, likely due to the complex cross-sectional variation, which may promote localized strain concentrations and enhance internal friction during oscillatory loading.

As with the storage modulus, geometry had a clear influence on the loss modulus across the entire frequency range. The slightly higher E'' values observed for the anatomical samples suggest a greater capacity for energy dissipation, probably associated with their complex geometry and the resulting potential for non-uniform stress distribution during oscillatory loading. In contrast, cylindrical samples tended to show greater dispersion in E''. This can be explained, once again, by their uniform cross-section, which offers fewer geometric constraints. Consequently, small differences in effective diameter and small surface defects due to the printing process or post-processing can have a proportionally greater effect on the viscous response, amplifying the variability of the loss modulus values. This behavior mirrors the dispersion trends observed for E', indicating that geometric simplification can amplify sensitivity to small manufacturing and alignment variations during dynamic testing. Consistently, a one-way ANOVA test was performed on the loss modulus E'' at each frequency, with results shown in Figure 6.6, yielding p-values $\leq$ 0.01 across all frequencies, confirming that geometry has a statistically significant effect on the viscous response.

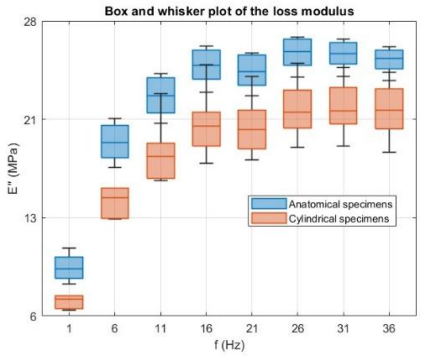

Figure 6.6. Box and whisker plots of the loss modulus E″ (MPa) as a function of frequency for anatomical (blue) and cylindrical (orange) specimens. A one-way ANOVA performed at each frequency shows a significant effect of specimen geometry ($p \leq 0.01$ at all frequencies), confirming that geometry influences the viscous response.

6.3.1.2.3 Loss Factor

The loss factor (tan δ) results are shown in Figure 6.7. For both specimen types, tan δ increased to a well-defined peak at approximately 16 Hz, followed by a gradual decrease or plateau at higher frequencies. Anatomical specimens reached a maximum of 0.74 ± 0.07, while cylindrical specimens peaked at 0.71 ± 0.11 before leveling off above 21 Hz. A peak in tan δ indicates the frequency range at which the material maximizes energy dissipation relative to energy storage. From a mechanical standpoint, this corresponds to a condition where internal molecular motions and microstructural rearrangements are optimally synchronized with the loading cycle, allowing viscous mechanisms to dominate over elastic ones at room temperature. Beyond this range, the reduced time available for molecular movement leads to a more elastic-like response and lower tan δ values. As observed for E' and E", specimen geometry influenced the magnitude and stability of tan δ across the frequency range, with anatomical specimens showing slightly higher average values. The greater data dispersion found in cylindrical specimens for E' and E" was also reflected in their tan δ values.

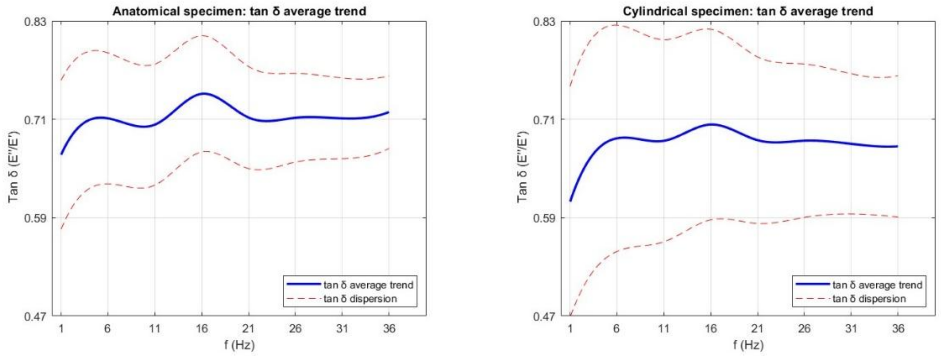

(a) (b)

Figure 6.7. Average loss factor (tan δ) as a function of frequency for (a) anatomical specimens and (b) cylindrical specimens. Data are presented as mean values with error bars representing the standard deviation across six replicates for each geometry.

The tables below summarize the viscoelastic parameters obtained for the anatomical specimens (Table 6.10) and cylindrical specimens (Table 6.11), expressed as the mean value and standard deviation.

Table 6.10. Summary of viscoelastic parameters for the anatomical specimens, expressed as mean ± standard deviation (SD).

Anatomical specimens			
Frequency (Hz)	**E' (MPa)**	**E" (MPa)**	**tan δ**
1	14.4 ± 1.2	9.6 ± 1.1	0.67 ± 0.09
6	26.6 ± 2.2	18.9 ± 1.4	0.71 ± 0.08
11	31.8 ± 2.5	22.4 ± 1.5	0.70 ± 0.07
16	33.3 ± 2.5	24.6 ± 1.4	0.74 ± 0.07
21	33.9 ± 2.3	24.2 ± 1.3	0.71 ± 0.06
26	35.9 ± 2.1	25.6 ± 1.2	0.71 ± 0.05
31	35.8 ± 1.9	25.5 ± 1.1	0.71 ± 0.05
36	34.9 ± 1.6	25.1 ± 0.9	0.72 ± 0.04

Table 6.11. Summary of viscoelastic parameters for the cylindrical specimens, expressed as mean ± standard deviation (SD).

Cylindrical specimens			
Frequency (Hz)	**E' (MPa)**	**E" (MPa)**	**tan δ**
1	12.3 ± 1.7	7.5 ± 1.4	0.61 ± 0.14
6	22 ± 3	15.2 ± 2.2	0.69 ± 0.14
11	27 ± 3	18.3 ± 2.4	0.68 ± 0.12
16	29 ± 3	20.4 ± 2.5	0.71 ± 0.11
21	30 ± 3	20.2 ± 2.2	0.68 ± 0.10
26	31 ± 3	21.4 ± 2.2	0.68 ± 0.09
31	31.6 ± 2.2	21.5 ± 2.1	0.68 ± 0.08
36	31.5 ± 1.9	21.3 ± 2.2	0.67 ± 0.09

This behavior aligns with the typical viscoelastic response of elastomeric materials, where stiffness increases with excitation frequency due to reduced time for molecular rearrangements [4], [5]. A similar trend has been reported for real human airways in [6], where the storage modulus likewise increased with frequency, reflecting the intrinsic time-dependent response of airway tissue under oscillatory loading.

The agreement in the frequency-dependent trends between printed specimens and biological airway tissue further supports the relevance of the proposed dynamic mechanical assessment for evaluating the suitability of soft 3D printed models in clinical simulation and training applications. Moreover, these results provide a consistent basis for the subsequent analysis of time-dependent behavior under constant loading conditions, addressed through creep testing and viscoelastic modelling in the following section.

6.3.1.3 Creep Test

The experimental data of creep response was fitted to a two-element generalized Maxwell model to characterize the material viscoelastic behavior. This configuration was not assumed as a priori, but determined from the shape of the experimental curves, where two distinct relaxation processes, one fast and one slow, were evident. The fit curves obtained from the interpolation of experimental data for both are shown in Figure 6.8. The fit quality was high for both geometries, with R^2 values of 0.99 for anatomical specimens and 0.98 for cylindrical specimens, and RMSE values in the order

of 10^{-4}, confirming that the model robustly reproduces the experimental slip curves. In addition, this modeling strategy is commonly used in biomechanical studies to describe the time-dependent mechanical behavior of soft biological tissues [7].

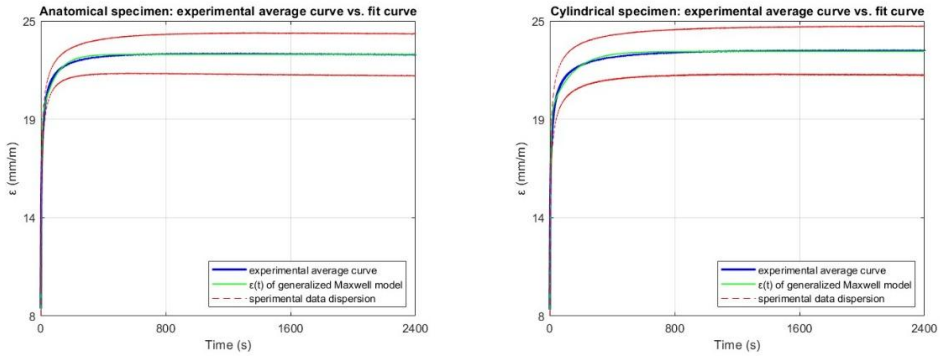

(a) (b)

Figure 6.8. Experimental average strain-time curve (blue), fit obtained from the two-element Generalized Maxwell model (green), and experimental data dispersion (red dashed lines), for (a) anatomical and (b) cylindrical specimens.

From data processing, therefore, following the methodology described in 5.3.1.2.3 Creep Analysis, the mathematical model that best represents the experimental trend of the data is:

$$\varepsilon(t) = A_0 + A_1(1 - e^{-B_1 t}) + A_2(1 - e^{-B_2 t}) \quad (5)$$

where the fitted coefficients (A_0, A_1, A_2, B_1 and B_2) obtained from non-linear regression are reported in Table 6.12. Using the relationships in 5.3.1.2.3 Creep Analysis, these coefficients were converted into the characteristic viscoelastic parameters (E_0, E_1, E_2, τ_1, τ_2, η_1, η_2) listed in Table 6.13. This parameter conversion allows the creep response to be interpreted in terms of physically meaningful elastic moduli, relaxation times and viscosities, facilitating direct comparison between specimen geometries and with reference biological tissues.

Table 6.12. Coefficients obtained from the non-linear regression of the experimental creep data using the two-element Generalized Maxwell model, along with the coefficient of determination R^2 and Root Mean Square Error (RMSE). Values are expressed as mean ± standard deviation (SD).

Specimens	A_0	A_1	A_2	B_1	B_2	R^2	RMSE
Anatomical	8.42	10.62 ± 0.08	4.02 ± 0.08	240 ± 8	122.8 ± 0.3	0.99	$8.4 \cdot 10^{-5}$
Cylindrical	8.37	11.22 ± 0.09	3.6 ± 0.9	204 ± 9	7.5 ± 0.3	0.98	$1.2 \cdot 10^{-4}$

Table 6.13. Viscoelastic parameters of the two-element Generalized Maxwell model for anatomical and cylindrical specimens, calculated from the regression coefficients in Table 6.12. Values are expressed as mean ± standard deviation (SD).

Specimens	E_0 (MPa)	E_1 (MPa)	E_2 (MPa)	τ_1 (s)	τ_2 (s)	η_1 (MPa·s)	η_2 (MPa·s)
Anatomical	9.9 ± 0.3	7.8 ± 1.7	21 ± 4	4.16 ± 0.14	81.5 ± 2.2	33 ± 7	$(17 \pm 4) \cdot 10^2$
Cylindrical	9.9 ± 0.3	7.4 ± 1.6	22.8 ± 1.6	4.91 ±0.20	134 ± 5	36 ± 8	$(30.6 \pm 2.4) \cdot 10^2$

The instantaneous modulus (E_0) was the same for both specimen types (9.9 MPa), indicating comparable initial elastic stiffness under sudden loading. Differences emerged in the Maxwell branch parameters. This suggests that anatomical specimens may dissipate a slightly larger portion of the applied strain through the faster relaxation process (τ_1 = 4.16 s anatomical, 4.91 s cylindrical), whereas cylindrical specimens exhibit a slower long-term relaxation (τ_2 = 134 s compared to 82 s for anatomical specimens). The viscosity values reflect these differences, with cylindrical specimens showing a notably higher ($\eta_2 = 30.6 \cdot 10^2$ MPa·s compared to $17 \cdot 10^2$ MPa·s), consistent with their longer secondary relaxation time. This behavior can be attributed to geometric effects: the uniform cross-section of the cylindrical samples may promote a more homogeneous stress distribution, leading to slower redistribution of internal stresses during the steady-state phase, while the complex geometry of the anatomical specimens facilitates faster local relaxation mechanisms. Overall, the creep analysis confirms that geometry plays a measurable role not only in the instantaneous elastic response but also in the balance between fast and slow relaxation processes. In general, the trends observed are consistent with those reported for elastomers of similar hardness, in which the relative contributions of rapid and slow relaxation processes, as well as the stability of elastic parameters beyond a deformation threshold, have been consistently documented [8]. When compared with published data on human trachea mechanical behavior [9], a similar relationship between short-

and long-term relaxation times is found, with τ_2 consistently about one order of magnitude greater than τ_1. This suggests that the material used in this study suitably reproduces the characteristic time-dependent viscoelastic response of the human trachea, strengthening the relevance of the proposed mechanical assessment framework for clinical simulation and training applications.

6.3.2 Mechanical Assessment of PolyJet Printed Specimens Results

This subchapter reports the mechanical assessment results obtained for PolyJet printed specimens, following the experimental workflow described in Section 5.3.2 Mechanical Assessment of PolyJet Printed Specimens. The objective of this case study is to provide a preliminary mechanical verification of soft materials produced by PolyJet technology, with particular attention to aspects not addressed in the SLA investigation, namely the influence of printing orientation on the mechanical response. To this end, static tensile tests were performed on ISO 527-1A dog-bone specimens printed in two different build orientations, horizontal and vertical, in order to evaluate the mechanical behaviour of a rubber-like photopolymer (Agilus30™).

As detailed in 5.3.2.1 Testing Machine and 5.3.2.1.1 Static Test, mechanical characterization was carried out through uniaxial tensile tests performed under controlled laboratory conditions. In contrast to the SLA case study, the PolyJet assessment is intentionally limited to static testing with the aim of focusing on process-induced variability rather than on a full viscoelastic characterization.

The reported results are organized according to the applied loading conditions and build orientations, consistently with 5.3.2.2 Mechanical Characterization and 5.3.2.2.1 Young's Modulus. Measurement uncertainty is addressed in accordance with the methodology described in 5.3.2.3 Measurement Uncertainty Analysis, and the results are therefore reported together with their associated uncertainty, in line with the approach adopted throughout this doctoral work. Although preliminary, these results contribute to the mechanical assessment framework extended to PolyJet and multi-material printed anatomical models in PoC environments.

6.3.2.1 Static Tensile Test Results

Stress-strain curves were obtained for eight specimens printed in each orientation. As illustrated in Figure 5.10, individual experimental curves were used to derive the corresponding average stress-strain curves and dispersion bands, which form the basis for the quantitative results. Figure 6.9 presents the graphs obtained from the stress-strain curves of the samples, interrupted at the failure point of the first specimen. Specifically, the figure displays the average curve (continuous blue line)

and the dispersion of the stress values (dashed red line), which represent the repeatability for both the horizontally (Figure 6.9a) and vertically (Figure 6.9b) oriented specimens. Young's modulus was estimated by applying the weighted linear regression approach described in 5.3.2.2.1 Young's Modulus, based on the subdivision of the average stress–strain curves into linear segments corresponding to different strain intervals. The average curve obtained for the horizontally oriented specimens can be approximated by a third-degree polynomial. Therefore, it was segmented into three parts: the first segment up to 30% strain, the second up to 80% strain, and the final segment up to break. All linear segments exhibit a correlation coefficient $r = 0.99$. In contrast, the average curve of the vertical specimens can be approximated to a second-degree polynomial, so it was divided into two linear segments, the first up to 20% strain and the second up to failure. Again, both linear segments have a correlation coefficient $r = 0.99$. The dispersion bands associated with the average curves indicate good repeatability within each printing orientation.

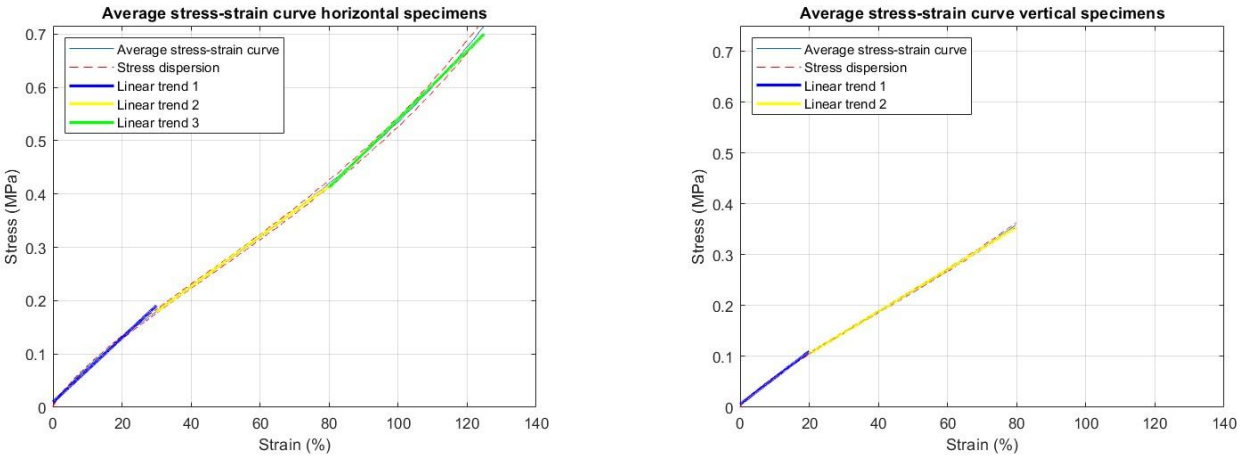

(a) (b)

Figure 6.9. Stress-strain curves of the tested samples, interrupted at the failure point of the first specimen. The graphs show the average curve (continuous blue line) and the stress dispersion (dashed red line), illustrating the repeatability of the results for (a) horizontally and (b) vertically oriented specimens.

Vertically printed specimens consistently support approximately half of the ultimate load achieved by horizontally printed ones, indicating a significantly reduced load-bearing capacity when the applied tensile load is oriented orthogonally to the layer stacking direction. Moreover, when analyzing the graph at the same applied load, and therefore at the same stress level, the vertically oriented specimens exhibit greater deformation. From these initial results, it appears that the vertically oriented specimens bear a lower load and break earlier than the others.

Measurement uncertainty was treated consistently with the methodology described in 5.3.2.3 Measurement Uncertainty Analysis. Accordingly, the dispersion of stress values and the uncertainty associated with Young's modulus estimation were derived by combining repeatability contributions and instrument-related uncertainties, ensuring coherence with the verification-oriented approach adopted throughout this doctoral work.

6.3.2.2 Effect of Printing Orientation on Mechanical Response

The comparison between horizontally and vertically printed PolyJet specimens provides clear quantitative evidence of process-induced mechanical anisotropy. The observed differences in tensile strength, elongation at break and elastic modulus cannot be attributed to material formulation, printing mode or layer thickness, which were kept constant across all specimens, but are directly related to the orientation of the deposited layers with respect to the applied load.

The main representative results of material behaviour obtained for vertical and horizontal printing are summarized in Table 6.14, expressed as mean ± standard deviation (SD).

Table 6.14. Results of material behavior expressed as mean ± standard deviation (SD). Percentage differences (Δ%) for the vertical specimens with respect to the horizontal ones, taken as reference, are also reported.

	UTS (MPa)	**ε_r (%)**	**E_1 (MPa)**	**E_2 (MPa)**	**E_3 (MPa)**	**UTS (MPa)**
Vertical specimens	0.36 ± 0.01	80 ± 1	0.52 ± 0.02	0.42 ± 0.01	-	0.36 ± 0.01
Horizontal specimens	0.72 ± 0.02	125 ± 1	0.60 ± 0.02	0.47 ± 0.01	0.64 ± 0.02	0.72 ± 0.02
Δ% (%)	50	36	13.3	10.6	-	50

The percentage differences ($\Delta_{\%}$) obtained for the vertically oriented specimen, taking the horizontal prints as the reference, are also shown. It is worth noting that vertical specimens have an ultimate tensile strength of 50% of the horizontal ones and can be stretched 36% less before breaking. Consequently, the modulus of elasticity in the first two linear trends and the overall average modulus of elasticity are at least 10% lower. This means that the vertically printed samples are more compliant and less resistant to deformation compared to those printed horizontally. Such behavior is consistent with expectations, as the tensile test applies the load along the direction in which, for

vertically printed samples, the interlayer cohesion is weaker, making the material overall more fragile in that orientation.

Comparing the results with the mechanical properties declared by the material manufacturer, shown in Table 6.15, the measured tensile strength values are an order of magnitude lower, and the maximum elongation achieved is approximately half of the declared value.

Table 6.15. Material Datasheet

Material	3D Printing Parameters	Mechanical Properties
Agilus30™ Translucent	High Mix mode Layer Thickness: 0.037 mm Accuracy on size: ± 0.2 mm	Tensile strength: 2.4 - 3.1 MPa Elongation at break: 220 – 270 %

This discrepancy could be attributed to both the specimen geometry, which was produced according to different standards, and to the specific manufacturing technology used. According to ASTM D-412, "specimens must be injection-molded or cut from a flat sheet"; as the material supplier did not provide any further details, it cannot be assumed that the specimens were produced using 3D printing technology. Therefore, it is even more scientifically relevant to investigate the mechanical performance of the material once it has been processed by 3D printing.

Considering the vertical printing orientation, the ultimate tensile strength is at least 85% lower than the value declared by the manufacturer. These findings are significant and should be carefully considered, especially in the biomedical field, where anatomical geometries are complex, and applied stresses may be neither uniformly distributed nor equidirectional. Depending on the direction of the applied load relative to the printing orientation, the material may behave differently than expected.

From a QC perspective, these findings underline that printing orientation represents a critical factor in the mechanical verification of printed components. Even within a preliminary assessment framework, neglecting orientation-induced anisotropy may lead to an overestimation of mechanical performance and to inappropriate material or process choices.

6.3.3 Implications for Mechanical Acceptance Considerations

The mechanical results obtained for both SLA and PolyJet printed specimens provide relevant indications for discussing preliminary acceptance considerations within a PoC QC framework, while highlighting the need for a verification and specific application interpretation of mechanical performance.

For SLA printed specimens, the combined outcomes of static, dynamic and creep tests demonstrate that the proposed mechanical assessment methodology offers good robustness. The estimated measurement uncertainty, evaluated for the proposed methods, is comparable to the uncertainty levels reported in the literature for the mechanical characteristics of materials. This consistency supports the validity of the proposed testing approach for mechanical assessment.

A key outcome of the SLA mechanical investigation is the quantitative comparison between the elastic response of anatomically derived trachea-shaped specimens and reference values reported for real human tracheal tissue. In particular, the Mean Absolute Percentage Error (MAPE) obtained from static tensile tests resulted in a value of approximately 2%, indicating a close agreement between the mechanical response of the printed models and that of the corresponding biological tissue. While this value does not represent a universal acceptance threshold, it provides a quantitative indication of mechanical compatibility for clinical simulation and training applications.

Importantly, this order of magnitude is consistent with the deviations identified in the dimensional assessment. As discussed in Subchapter 6.2.2 for two-dimensional measurements and in Subchapter 6.3.2 for volumetric assessment of clavicle models, discrepancies on the order of a 2% emerged as a recurring reference across different measurement domains. Although derived from different physical quantities, this convergence suggests that relative deviations of similar magnitude may represent a coherent and practical reference for first-level quality evaluation within PoC workflows, when interpreted with measurement uncertainty.

The results further confirm that specimen geometry plays a significant role in the measured mechanical response. For SLA specimens, standardized dog-bone geometries consistently exhibit higher apparent stiffness compared to cylindrical and anatomically derived specimens, indicating that material-level characterization alone may not be sufficient to evaluate the mechanical suitability of anatomical models. Conversely, tests performed on anatomically relevant geometries provide mechanical responses that more closely reflect the deformation conditions encountered during

clinical use, supporting the inclusion of geometry-specific testing in mechanical verification procedures.

The PolyJet case study complements these findings by highlighting the influence of process-related factors, particularly printing orientation, on mechanical behavior. Static tensile tests reveal evident orientation-dependent anisotropy, with vertically printed specimens exhibiting reduced tensile strength, elongation at break and elastic modulus compared to horizontally printed ones. These results demonstrate that, in addition to geometry, manufacturing parameters inherent to the printing technology can significantly affect mechanical performance and must therefore be explicitly considered in mechanical verification activities.

Overall, the findings suggest that preliminary mechanical acceptance considerations for soft 3D printed anatomical models should be defined in relation to the intended clinical use, the characteristic deformation modes and the relevant loading time scales. Within this context, the need arises to define specific acceptance criteria, expressed in terms of relative percentage deviations, for the mechanical properties involved. The recurrence of relative deviations on the order of a few percent across both dimensional and mechanical assessments further reinforces the coherence and applicability of the proposed quality control framework for point-of-care 3D printing.

References

[1] J. K. Rains, J. L. Bert, C. R. Roberts, and P. D. Pare, "Mechanical properties of human tracheal cartilage," *J. Appl. Physiol.*, vol. 72, no. 1, pp. 219–225, Jan. 1992, doi: 10.1152/jappl.1992.72.1.219.

[2] R. K. Lambert, E. M. Baile, R. Moreno, J. Bert, and P. D. Pare, "A method for estimating the Young's modulus of complete tracheal cartilage rings," *J. Appl. Physiol.*, vol. 70, no. 3, pp. 1152–1159, Mar. 1991, doi: 10.1152/jappl.1991.70.3.1152.

[3] O. Trabelsi, A. P. Del Palomar, J. L. López-villalobos, A. Ginel, and M. Doblaré, "Experimental characterization and constitutive modeling of the mechanical behavior of the human trachea," *Med. Eng. Phys.*, vol. 32, no. 1, pp. 76–82, Jan. 2010, doi: 10.1016/j.medengphy.2009.10.010.

[4] D. Dunson, "Characterization of Polymers using Dynamic Mechanical Analysis (DMA)," 2017.

[5] J. Cortazar-Noguerol, F. Cortés, I. Sarría, and M. J. Elejabarrieta, "Preload Influence on the Dynamic Properties of a Polyurethane Elastomeric Foam," *Polymers*, vol. 16, no. 13, p. 1844, June 2024, doi: 10.3390/polym16131844.

[6] J.-Y. Wang, P. Mesquida, P. Pallai, C. J. Corrigan, and T. H. Lee, "Dynamic Properties of Human Bronchial Airway Tissues," Nov. 23, 2011, *arXiv*: arXiv:1111.5645. doi: 10.48550/arXiv.1111.5645.

[7] X. Wang, J. A. Schoen, and M. E. Rentschler, "A quantitative comparison of soft tissue compressive viscoelastic model accuracy," *J. Mech. Behav. Biomed. Mater.*, vol. 20, pp. 126–136, Apr. 2013, doi: 10.1016/j.jmbbm.2013.01.007.

[8] P. Zielonka *et al.*, "Stress Relaxation Behaviour Modeling in Rigid Polyurethane (PU) Elastomeric Materials," *Materials*, vol. 16, no. 8, p. 3156, Apr. 2023, doi: 10.3390/ma16083156.

[9] F. Safshekan, M. Tafazzoli-Shadpour, M. Abdouss, and M. B. Shadmehr, "Viscoelastic Properties of Human Tracheal Tissues," *J. Biomech. Eng.*, vol. 139, no. 1, p. 011007, Jan. 2017, doi: 10.1115/1.4034651.

Chapter 7

Conclusions

7.1 Overview of the Conclusions

This chapter brings together the main outcomes of the doctoral research, providing an interpretation of the results presented throughout the thesis. The conclusions are intended to guide the reader through the key findings, underlining their methodological relevance, experimental robustness and implications for point-of-care (PoC) biomedical 3D printing.

The chapter synthesizes the conclusions derived from the dimensional and mechanical assessment activities, highlighting how these results contribute to the definition of a measurement-based quality control framework compatible with clinical environments. Particular attention is paid to the role of measurement uncertainty and to the interpretation of variability of the results in relation to the intended clinical use of the printed models.

Finally, the chapter outlines the overall contribution of the thesis, discusses its limitations and identifies future research directions, framing the results within the broader context of regulatory requirements and ongoing standardization efforts in biomedical additive manufacturing.

7.2 Conclusions on dimensional assessment

The investigations on dimensional assessment based on medical imaging can be effectively adopted as a quantitative quality control tool for 3D-printed anatomical models produced in point-of-care (PoC) environments. The proposed approach addressed both two-dimensional and three-dimensional evaluations, starting from clinical image data and extending to the quantitative comparison of printed replicas.

Two-dimensional CT-based analyses were performed on selected transverse and coronal slices of a reference cranial model derived from diagnostic CT imaging, as well as on eight corresponding replicas generated by re-segmenting CT scans of the reference model itself. This strategy was adopted to specifically investigate the variability introduced by the segmentation procedures to post-processing operations. The analyzed slices were identified using a rigorous and objective image-analysis method, corresponding to the slice exhibiting the maximum outer diameter for each

cranial model. On these slices, geometric parameters including section area, maximum diameter and local thicknesses were detected through pixel-based image analysis. Among the investigated parameters, the maximum longitudinal diameter showed the highest stability, with percentage differences consistently below approximately 1%. This suggests that deviations of this magnitude may be considered as a preliminary reference for dimensional acceptance when two-dimensional, slice-based are adopted in PoC environments. Conversely, section area and local thickness measurements exhibited higher variability and stronger dependence on local geometry, highlighting the intrinsic limitations of two-dimensional assessment. For this reason, three-dimensional CT-based volumetric analyses were introduced to capture global geometric deviations in a more comprehensive manner.

Accordingly, the dimensional investigation was extended to a three-dimensional volumetric assessment applied to six clavicle models, selected as a representative bone geometry to evaluate global geometric consistency. In this case study, volumetric measurements derived from CT-based reconstructions enabled the quantification of inter-model repeatability and the comparison between diagnostic CT systems commonly available in PoC settings and higher-resolution industrial CT acquisitions used as metrological references. The comparison between the two imaging modalities revealed a mean absolute percentage error of approximately 0.65% between diagnostic and industrial CT measurements, with volumetric discrepancies among replicas remaining within a few percent and typically below approximately 2%, even under intensive printing conditions. These results indicate that diagnostic CT, despite its lower spatial resolution, can provide sufficiently accurate and reliable dimensional information to be integrated into PoC quality control workflows. This aspect is particularly relevant for implantable medical devices, for which pre- and post-operative CT examinations are routinely performed in clinical practice, allowing an additional dimensional verification to be embedded into existing imaging protocols without introducing additional measurement steps.

7.3 Conclusions on mechanical assessment

The mechanical investigations confirmed that measurement-based mechanical assessment represents a necessary component of quality control frameworks for 3D-printed anatomical models produced in point-of-care (PoC) environments, particularly when soft materials and patient-specific geometries are involved. The proposed methodology combined standardized specimens and anatomically representative geometries to investigate the influence of printing technology, build orientation and specimen geometry on mechanical behavior.

Mechanical characterization was conducted through a structured set of tests, including static tensile tests, dynamic mechanical analysis and creep experiments, applied to SLA and PolyJet printed specimens. Standardized dog-bone and cylindrical geometries were used to enable material comparisons, while anatomically shaped specimens were introduced to assess mechanical behavior under deformation more representative of clinical use.

Tensile tests under uniaxial loading were used in combination with a proposed piecewise linear regression approach to estimate Young's modulus from selected linear segments of the stress-strain response. This method enabled an identification of the elastic regime and a quantitative estimation of the associated uncertainty, enabling comparisons across printing configurations, with manufacturer declared material properties, and with native biological tissue in the context of surgical simulation applications. The uncertainty obtained for the estimated Young's modulus was found to be in line with the ranges typically reported in the literature, thereby providing robustness to the proposed methodology and supporting its applicability for comparative mechanical characterization across printing configurations in PoC environments.

For SLA-printed specimens, the combined outcomes of static, dynamic and creep tests demonstrated the overall robustness of the proposed mechanical assessment approach. In particular, tests performed on anatomically derived trachea-shaped specimens showed close agreement with reference mechanical properties reported for human tracheal tissue, with a Mean Absolute Percentage Error of approximately 2% obtained from static tensile tests. While this value does not define a universal acceptance threshold, it provides a quantitative indication of mechanical compatibility for clinical simulation and training applications.

The results further highlighted the significant role of specimen geometry in the measured mechanical response. Standardized dog-bone specimens consistently exhibited higher apparent stiffness compared to cylindrical and anatomically shaped samples, indicating that material-level characterization alone may not be sufficient to evaluate the mechanical suitability of anatomical models. Conversely, geometry-specific testing provided mechanical responses more representative of clinical deformation conditions, supporting its inclusion in mechanical verification procedures.

The PolyJet case study complemented these findings by emphasizing the influence of process-related factors, particularly printing orientation, on mechanical performance. Static tensile tests revealed clear orientation-dependent anisotropy, with vertically printed specimens exhibiting reduced elastic modulus, tensile strength and elongation at break compared to horizontally printed

ones. This confirms that both geometry and manufacturing parameters inherent to the printing technology must be explicitly considered in mechanical quality control activities.

7.4 Overall and Novel Contributions of the Doctoral Thesis

This doctoral thesis provides an original contribution to biomedical additive manufacturing through the design, development and experimental validation of measurement methods and systems for the functional and performance characterization of 3D-printed biomedical models produced in PoC environments. The central novelty of the work lies in the definition of a measurement-based QC framework in which dimensional and mechanical verification activities are integrated and interpreted as complementary components, rather than independent checks, to support the evaluation of geometric fidelity, mechanical compatibility and process repeatability in clinical contexts.

A first contribution of the thesis is the critical analysis of the biomedical additive manufacturing landscape and its regulatory context, which highlighted the absence of harmonized, operational quality control protocols tailored to PoC workflows. This analysis provided the conceptual basis for the subsequent experimental activities and motivated the development of measurement-based approaches capable of ensuring reproducibility, traceability and transparency in decentralized hospital manufacturing.

In response to the dimensional assessment objective, this thesis report about the design, development and validation of imaging-based measurement methods that combine two-dimensional slice-based analyses and three-dimensional volumetric evaluations within a unified framework. Diagnostic and industrial CT data, together with image-analysis strategies, were used to quantify geometric fidelity in terms of volumes, diameters, thicknesses and cross-sectional geometry. The explicit integration of uncertainty estimation enabled a rigorous interpretation of dimensional variability and demonstrated that diagnostic CT data routinely available in hospitals can be reliably exploited for quality control purposes in PoC environments.

The mechanical assessment objective is addressed through the development and validation of a comprehensive experimental strategy that integrates standardized specimens and anatomically representative geometries, multiple testing modalities and uncertainty parameter estimation. Static tensile tests, dynamic mechanical analysis and creep experiments were combined to investigate elastic and viscoelastic behavior across different technologies and build orientations. Within this framework, a dedicated piecewise linear regression method was designed and validated for the

estimation of Young's modulus in rubber-like materials, providing a robust measurement approach for the functional characterization of soft 3D-printed biomedical systems and enabling meaningful comparisons with manufacturer-declared properties and native biological tissues.

A unifying and novel outcome of the thesis is the integrated interpretation of dimensional and mechanical results within a QC framework. Across different case studies and measurement domains, relative deviations were consistently found to be in the order of a few percent. In particular, the recurrence of deviations of approximately 2% across both dimensional and mechanical assessments emerges as a meaningful reference magnitude. While not representing a universal acceptance threshold, this value provides quantitative basis that may be extended to other dimensional and mechanical parameters, to be specifically investigated and validated according to the intended clinical application.

Overall, this doctoral research bridges metrological consistency, experimental validation and clinical constraints, delivering a measurement-based quality control framework that supports reproducible, uncertainty-aware and application-driven verification practices for PoC biomedical 3D printing. The results provide both methodological advances and practical guidance for future PoC laboratories seeking to standardize workflows and ensure the safe and reliable use of 3D-printed medical models.

7.5 Limitations and Future Research Directions

Despite the encouraging results and the internal coherence of the proposed QC framework, several limitations of the present work should be acknowledged. The experimental investigations were conducted on a limited set of materials, printing technologies and anatomical models selected to be representative of clinically relevant use cases but not exhaustive in PoC environments. In particular, AM technologies based on powder processing were not investigated, mainly due to the stringent health and safety requirements associated with their use in hospital settings, including dedicated facilities, controlled ventilation systems and environmental monitoring, although they hold promise in the field of titanium prosthetics and implants.

From a dimensional perspective, although diagnostic CT-based methods proved to be effective for QC purposes, the influence of image acquisition parameters, scanner-specific characteristics and reconstruction algorithms was not systematically explored across multiple clinical imaging systems. Further studies involving multi-center datasets would be required to assess the generalizability of

the proposed dimensional assessment methods and to refine uncertainty models under heterogeneous imaging and acquisition protocol conditions.

Regarding mechanical assessment, the experimental tests focused on static, dynamic and creep loading conditions relevant to simulation and training applications. However, other clinically relevant aspects, such as fatigue behavior, long-term aging, environmental effects and post-processing-induced property variations, were not addressed. In addition, the translation of specimen mechanical characterization to complex anatomical models remains a challenging task, particularly for highly heterogeneous or multi-material structures.

Future research should therefore aim to extend the proposed framework to a broader range of materials, including emerging multi-material and gradient structures, and to additional anatomical regions and clinical applications. Particular attention should be paid to establishing stronger correlations between simplified test specimens and the mechanical response of full anatomical models under realistic loading conditions. The systematic evaluation of sterilization processes and their impact on both dimensional accuracy and mechanical integrity also represents a critical and still underexplored research direction.

Finally, further efforts are needed to translate experimental evidence into shared verification practices and harmonized guidance for PoC 3D printing. Future developments should focus on refining acceptance criteria, strengthening uncertainty estimation and contributing with providing a database input for ongoing standardization and regulation. In this perspective, the methodologies and results presented in this thesis provide a foundation for continued research at the intersection of metrology, biomedical engineering and clinical practice.